

IMPROVING THULIUM FIBER LASER LITHOTRIpsy EFFICIENCY

by

Luke Allen Hardy

A dissertation submitted to the faculty of
The University of North Carolina at Charlotte
in partial fulfillment of the requirements
for the degree of Doctor of Philosophy in
Optical Science and Engineering

Charlotte

2018

Approved by:

Dr. Nathaniel Fried

Dr. Yasin Raja

Dr. Irina Nesmelova

Dr. Tino Hofmann

Dr. Harish Cherukuri

ABSTRACT

LUKE ALLEN HARDY. Improving Thulium Fiber Laser Lithotripsy Efficiency
(Under the direction of DR. NATHANIEL M. FRIED)

Kidney stone disease affects approximately 10% of the U.S. population. Conventional Holmium:YAG laser lithotripsy is an effective minimally invasive treatment that operates primarily on a photothermal interaction. The heat generated causes a rise in temperature in the calculi, leading to ablation. However, in this application, laser irradiation through an optical fiber occurs in a water environment, bringing about other mechanical ablation effects as well.

Heating of water filled subsurface pores, cracks, and fissures causes vaporization and generates large pressures inside the stone. Such pressures can cause fragmentation of the kidney stone, through “micro-explosions”. Uneven heating also causes thermo-elastic expansion of the kidney stone, translating to differences in pressure inside of the calculi and micro-cracks in the kidney stone which further facilitates ablation.

The conventional Ho:YAG laser is limited to operation at high pulse energies and low pulse rates (‘fragmentation’ mode), thus producing larger stone fragments, and greater retropulsion. The ‘fragmentation’ mode may increase the probability that a surgeon loses a stone fragment, requiring the patient to undergo a second surgery.

The Thulium Fiber laser (TFL) is being explored as an alternative to the Ho:YAG laser for lithotripsy, due to its ability to operate at low pulse energies and high pulse rates (‘dusting’ mode), which tend to produce smaller stone fragments, and reduced retropulsion. The TFL wavelength at 1908 nm also more closely matches a high temperature water absorption peak at 1910 nm than the Ho:YAG wavelength at 2120 nm. Additionally, the

TFL near single mode spatial beam profile enables laser energy to be coupled into smaller fibers (50 - 150- μm -core) than currently being used with Ho:YAG (\geq 200- μm -core) lithotripsy.

TFL ablation rate as a function of pulse rate was examined at pulse rates up to 500 Hz. The ablation rate scales linearly with pulse rate and can be effective at higher pulse rates (500 Hz) with the use of a stone stabilization device.

Operation times were compared between the TFL and Ho:YAG lasers, using an in vitro ureter model, with the stone allowed to move freely. Operative time and temperature data near the ablation site was tested to confirm safe operating parameters. TFL operation time was found to be shorter than for the Ho:YAG laser.

Collapse of laser induced vapor bubbles is the primary cause of stone retropulsion. The bubble dimensions are directly proportional to the amplitude of pressure waves induced in the water. Dimensions, dynamics, and pressures of the bubbles produced by the TFL (5-70 mJ, 200-1000 μs) and Ho:YAG (600 mJ, 350 μs) were examined at different laser parameters using a high speed camera and needle hydrophone. TFL bubbles were discovered to collapse multiple times along the optical axis of the fiber, while the Ho:YAG laser created a single, larger, bubble that collapsed only once. Due in part to these differing bubble dynamics, lower pressures were observed with the TFL.

Influence of water vaporization inside of the stone was examined. The study determined how dry and wet environments change the primary ablation mechanism. A scanning electron microscope was used to analyze the ablation crater, and crack formation before and after each study. This information may be used to determine the optimum laser, and environmental parameters for maximum ablation rates.

Current commercial TFL lasers typically operate at a 1940 nm wavelength, translating into an approximately 20% decrease in the low temperature water absorption coefficient, compared to the 1908 nm wavelength. Previous studies have found a difference in ablation damage due to dynamic water absorption coefficients. The study determined if the decrease in high temperature water absorption translates into a corresponding decrease in ablation rate and threshold.

The 1940 nm TFL and high pulse rate Ho:YAG was examined in this study. Recent advances in Ho:YAG technology allow both the TFL and Ho:YAG to be operated at the same laser parameters. This study compared ablation rate and debris particle size between the two lasers, using the same laser parameters.

The experiments above are designed to examine the TFL ablation mechanism and find optimum laser parameters to safely increase stone ablation rates, and ablation efficiency.

DEDICATION

This thesis is dedicated to my parents, grandparents, and family for their constant encouragement and support.

ACKNOWLEDGMENTS

I would like to thank all of my fellow former and current Biomedical Optics Laboratory members and members of other laboratories who have provided insight and assistance throughout my graduate career: Dr. Thomas Hutchens, Dr. Richard Blackmon, Dr. Christopher Wilson, William Perkins, Dr. Chun-Hung (Jack) Chang, Joshua Kennedy, David Gonzalez, and Layton Hall.

I would also like to thank Dr. Pierce Irby, from the McKay Department of Urology at Carolinas Medical Center for his clinical advice in designing the experiments.

I would also like to thank Dr. William Nau of Medtronic (Boulder, CO) for providing the needle hydrophone system used in our experiments.

I would also like to thank Dr. Gregory Altshuler, Dr. Ilya Yaroslavsky, and Igor Perchuk from IPG Medical (Marlborough, MA) for providing the 1940 nm laser and assistance with the TFL vs. high power Ho:YAG study.

I would also like to thank Kurt Shelton of Olympus (Southborough, MA) for providing the high power Holmium:YAG laser in the TFL vs. high power Ho:YAG study. I also thank Dr. Michel Daudon (Tenon Hospital, Paris, France) for providing the stone samples used in these experiments.

TABLE OF CONTENTS

LIST OF TABLES	xi
LIST OF FIGURES	xii
LIST OF ABBREVIATIONS	xix
CHAPTER 1: Introduction	1
1.1 Kidney Stone Disease	1
1.2 Laser Lithotripsy	2
1.3 Holmium:YAG Laser	8
1.4 Thulium Fiber Laser	10
1.5 Current Research	11
CHAPTER 2: Rapid Thulium Fiber Laser Lithotripsy at High Pulse Rates	14
2.1 Introduction	14
2.2 Methods	15
2.3 Results	18
2.4 Discussion	21
2.5 Conclusion	22
CHAPTER 3: Comparison of Thulium Fiber and Low Power Holmium:YAG Laser Lithotripsy in an In Vitro Ureter Model	23
3.1 Introduction	23
3.2 Methods	23
3.3 Results	27
3.4 Discussion	32
3.5 Conclusion	36
CHAPTER 4: Analysis of Thulium Fiber Laser Induced Bubble Dynamics for Ablation of Kidney Stones	37

4.1 Introduction	37
4.2 Methods	39
4.3 Results	44
4.4 Discussion	56
4.5 Conclusion	61
CHAPTER 5: Investigation of the Thulium Fiber Laser Ablation Mechanism for Real and Artificial Kidney Stones in Air and Water Mediums using Scanning Electron Microscopy	62
5.1 Introduction	62
5.2 Theory	62
5.3 Methods	64
5.4 Results	66
5.5 Discussion	81
5.6 Conclusion	85
CHAPTER 6: Comparison of 1908 and 1940 nm Wavelengths for Thulium Fiber Laser Lithotripsy	86
6.1 Introduction	86
6.2 Methods	89
6.3 Results	94
6.4 Discussion	97
6.5 Conclusion	99
CHAPTER 7: High Power Holmium:YAG vs Thulium Fiber Laser for Dusting of Calcium Oxalate Kidney Stones	100
7.1 Introduction	100
7.2 Methods	102
7.3 Results	106

7.4 Discussion	109
7.5 Conclusion	112
CHAPTER 8: Conclusion	113
REFERENCES	116
APPENDIX A: LIST OF PEER-REVIEWED PUBLICATIONS	124
APPENDIX B: LIST OF PEER-REVIEWED CONFERENCE PROCEEDINGS	126
APPENDIX C: DYNAMIC PULSING DURING THULIUM FIBER LASER FOR LITHOTRIPSY	128
APPENDIX D: FRAGMENTATION AND DUSTING OF LARGE KIDNEY STONES USING COMPACT AIR-COOLED, HIGH PEAK POWER, 1940- nm, THULIUM FIBER LASER	134

LIST OF TABLES

TABLE 2.1:	TFL stone ablation rates (mg/s) as a function of stone type and stone stabilization device.	20
TABLE 3.1:	Total laser and operating times to fragment 4-5 mm diameter calcium oxalate stones into fragments smaller than 1.5 mm, and peak saline temperatures measured during experiments.	29
TABLE 4.1:	Thulium fiber laser parameters and bubble dimensions using 105- μ m-core fiber.	45
TABLE 4.2:	Thulium fiber laser parameters and bubble dimensions using 270- μ m-core fiber.	46
TABLE 4.3:	Holmium:YAG laser parameters and bubble dimensions using 270- μ m-core fiber.	53
TABLE 5.1:	Thermal and mechanical properties of different kidney stone compositions, compiled from multiple sources.	63
TABLE 5.2:	Qualitative description of ablation effects on kidney stones and stone phantoms as a function of medium, wavelength, and stone composition.	84
TABLE 6.1:	Laser and fiber parameters used for 1908 and 1940 nm wavelength Thulium fiber lasers.	90
TABLE 7.1:	Summary of laser settings used for ‘dusting’ ablation mode in TFL and Ho:YAG laser lithotripsy experiments.	102
TABLE 7.2:	Percent (%) of stone fragments falling within each size range as a function of laser type and settings.	108
TABLE 7.3:	Total number of stone fragments collected within size range of $0.2 < x < 2$ mm as a function of laser type and setting (n = 5 sample size).	109

LIST OF FIGURES

FIGURE 1.1:	Photographs of different kidney stone compositions. Calcium oxalate based stones account for 80%, and uric acid 5-10% of all stones encountered in the clinic	2
FIGURE 1.2:	Image of ureteroscopic procedure. An optical fiber would be placed in the same working channel as the basket instrument shown.	3
FIGURE 1.3:	Absorption as a function of wavelength and kidney stone types. For near-IR wavelengths, absorption does not change significantly according to stone type.	4
FIGURE 1.4:	The TFL room temperature water absorption peak at 1940 nm shifts to about 1910 nm at higher temperatures. The major emission lines of the TFL at 1908 and 1940 nm match this shifting peak more closely than the Ho:YAG laser wavelength at 2120 nm [39][40].	11
FIGURE 2.1:	Experimental setup for TFL lithotripsy with a uric acid stone immobilized in a clamp and submerged in a saline bath.	16
FIGURE 2.2:	Experimental setup for TFL lithotripsy, showing rigid endoscope, optical fiber, and stone basket for grasping a uric acid stone immersed in a saline bath.	17
FIGURE 2.3:	TFL stone ablation rate as a function of stone type and laser pulse repetition rate.	19
FIGURE 2.4:	Representative uric acid stone (a) before and (b) after TFL lithotripsy with 35 mJ, 500 μ s, and 500 Hz. Total laser irradiation time was 24 s and total treatment time was 65 s. Initial stone size was 8 x 4 x 5 mm and initial stone mass was 135 mg.	20
FIGURE 3.1:	Human urinary stone samples with composition of 60% calcium oxalate monohydrate and 40% calcium phosphate used in all of these studies.	25

- FIGURE 3.2: (a) Experimental setup showing the ureter model, including 6-mm-inner-diameter tube, 1.5 mm mesh sieve, and micro-thermocouple. (b) Close-up view through the flexible ureteroscope of the fiber tip and stone sample during the experiment. The thermocouple was placed 3 mm from the center of the tube (along the tube wall) and 1 mm above the mesh sieve. 26
- FIGURE 3.3: Temperature vs. time plots showing worst case (highest peak temperature) for Holmium:YAG and TFL lithotripsy procedures. (a) Holmium laser, $T_p = 25.5\text{ }^\circ\text{C}$; Laser time = 288 s; Total time = 320 s; (b) TFL at 150 Hz; $T_p = 38\text{ }^\circ\text{C}$; Laser time = 154 s; Total time = 154 s; (c) TFL at 300 Hz; $T_p = 48\text{ }^\circ\text{C}$; Laser time = 43 s; Total time = 47 s; (d) TFL at 500 Hz; $T_p = 48\text{ }^\circ\text{C}$; Laser time = 22 s; Total time = 107 s. Note that the variation in temperatures measured was a function of not the only laser parameters used, but also of the variable movement of the fiber tip and stone sample with respect to the thermocouple position. 30
- FIGURE 3.4: (a) Stone fragments after TFL lithotripsy. Inset figure shows the original stone (at the same scale). (b) Video frame showing multiple large stone chips temporarily obstructing the sieve and saline irrigation flow at the time point in which the absolute peak temperature of $48\text{ }^\circ\text{C}$ was measured by the micro-thermocouple during TFL lithotripsy at 500 Hz (Figure 3.2b). 31
- FIGURE 4.1: Temporal beam profiles produced by Thulium fiber laser (TFL) and Holmium:YAG laser used in this study. (a) The TFL has a $2\text{ }\mu\text{s}$ -long spike at beginning of pulse but overall energy is more uniformly distributed across $\sim 500\text{ }\mu\text{s}$ pulse, with the exception of a $100\text{ }\mu\text{s}$ fin shape at the beginning and a $\sim 75\text{ }\mu\text{s}$ taper at the end of the pulse. (b) Holmium laser has a large portion of energy delivered at beginning of macro-pulse, then decays after $\sim 75\text{ }\mu\text{s}$. Holmium beam profile also contains multiple 1-3 μs micro-pulses in $\sim 350\text{ }\mu\text{s}$ macro pulse envelope. 39
- FIGURE 4.2: Diagram of experimental setup used with Thulium fiber laser for high speed imaging of cavitation bubbles. 41
- FIGURE 4.3: Temporal profiles of the 1940 nm laser as a function of pulse energy and time. The laser is set to a $500\text{ }\mu\text{s}$ pulse duration. Shows how the temporal profile of the laser changes depending on the pulse energy setting. 43

- FIGURE 4.4: Graph of bubble width as a function of TFL pulse energy and time during a single 500 μs pulse using 105 μm fiber. The time necessary to initiate a bubble increases as pulse energy decreases. There is also a clearly defined expansion and collapse for the first bubble due to the spike observed at the beginning of the TFL temporal beam profile shown in Figure 4.1, followed by a more chaotic process for the rest of the laser pulse. The inset image of a bubble shows how width and length of bubble dimensions were measured during data analysis. 45
- FIGURE 4.5: The laser temporal beam profile (red) from Figure 4.5A is superimposed with the bubble width (green), and needle hydrophone pressure data (blue), as a function of time. The synchronized data shows how bubble width influences the pressure transients, while confirming that multiple bubble collapses occur during a single laser pulse. Figure 4.5B shows a small pressure transient occurring during the initial 2- μs -long set of spikes in the TFL temporal beam profile. The spikes are believed to be the cause of the onset of the first bubble. Note that although it appears that the bubble is expanding before the pulse, this is an artifact from the oscilloscope sampling the pressure transient and beam profile data at a smaller temporal resolution (0.4 μs) than for the camera (9.5 μs). 47
- FIGURE 4.6: Maximum bubble size and shape as a function of both TFL pulse energy and pulse duration for 105 μm fiber. As the pulse energy increases, for a given fixed pulse duration, there is an increase in bubble dimensions. For a fixed pulse energy and increase in the pulse duration, there is a decrease observed in bubble dimensions. 48
- FIGURE 4.7: Frames taken with a high-speed camera at successive 9.5 μs intervals, showing formation of a bubble stream during a single TFL pulse delivered through a 105 μm fiber at 35 mJ and 500 μs . The sequence shows multiple bubble expansions and collapses along the bubble stream. The chaotic nature after the initial bubble is also observed in these frames. 50

- FIGURE 4.8: Laser induced vapor bubble and stone debris and as a function of fiber-to-stone working distance and time for TFL laser settings of 35 mJ pulse energy, 500 μ s pulse duration, and 105- μ m-core fiber. There is a larger amount of debris produced by a fiber in contact mode (0 mm) compared to a noncontact working distance of 1 mm away, at which laser stone ablation stallout occurs. Note that the third row of images (1 mm working distance) were acquired at a different aspect ratio (128 x 344) than the other rows of images (320 x 184). 51
- FIGURE 4.9: Maximum bubble size and shape as function of Holmium laser pulse energy for a fixed pulse duration of 350 μ s, using a 270 μ m fiber. Bubble dimensions increase as pulse energy increases, as expected. 52
- FIGURE 4.10: Ho:YAG vapor bubble frames with 9.5 μ s intervals for a 1000 mJ, 350 μ s laser pulse, showing an initial expansion to a single collapse, that rebounds at the end of the laser pulse. 54
- FIGURE 4.11: Representative Holmium:YAG vapor bubble pressure transient with pulse energy of 800 mJ, and pulse duration of 350 μ s. 55
- FIGURE 4.12: Bubble width as a function of time for different peak powers of the TFL emitting a 1940 nm wavelength. The number of bubble expansions and collapses increase as the peak power decreases. 56
- FIGURE 5.1: SEM images of different natural COM formations taken at magnifications of (A) 1,600 \times and (B) 1,100 \times . 67
- FIGURE 5.2: Ablation crater and char formed by irradiation from the 1908 nm TFL in a water environment. (A) Photograph of ablation crater with arrows designating char spot. (B) SEM image taken at 70 \times magnification. 67
- FIGURE 5.3: (A,B) SEM images taken at magnifications of 1,600 \times and 900 \times , inside the char spot of COM stones irradiated at 1908 nm in water, showing melting of calculi. (C,D) SEM images taken outside of char spot on COM stone, but inside crater, at magnifications of 1,600 \times and 650 \times , with arrows pointing to mechanically induced fracturing. 68
- FIGURE 5.4: (A) Photograph of COM stone after irradiation in air with (B) SEM counterpart in image at 27 \times magnification. (C,D) COM stone irradiated in an air environment inside the crater at magnifications of 1600 \times and 3700 \times . 69

- FIGURE 5.5: (A,B) SEM images of natural uric acid calculi taken at magnifications of 600× and 4,500×. 70
- FIGURE 5.6: (A) Photograph of ablation crater in UA stone after irradiation at 1908 nm in water; (B,C,D) SEM images taken at magnifications of 22×, 800×, and 2,500×. Mechanical damage in the form of multiple fractures in (C) and (D), is shown by arrows. 71
- FIGURE 5.7: (A) Photograph of crater in UA stone after irradiation at 1908 nm in air. (B,C) SEM images at magnifications of 1,600× and 16,000×. Direct melting of the stone surface is observed, without any mechanical damage (e.g. fractures). 72
- FIGURE 5.8: (A) Photograph of COM stone in water after irradiation at 1940 nm with high pulse energy. (B,C,D) SEM images at magnifications of 60×, 650×, and 1,1000×. (C,D) Significant fracturing due to micro-explosions, with a small amount of melting in the material is observed. 74
- FIGURE 5.9: (A) Photograph of COM stone after laser irradiation at 1940 nm in air. (B,C) SEM images of ablation crater taken at magnifications of 50× and 1500×. (C) Melted material caused by thermal build up from direct absorption of light by stone material. 74
- FIGURE 5.10: (A) Photograph of UA stone in water after irradiation at 1940 nm with high pulse energy; (B,C,D) SEM images at 19×, 600×, and 1,700× magnification. Significant mechanical fractures are present as indicated by the arrows. 75
- FIGURE 5.11: (A) Photograph of UA stone after laser irradiation at 1940 nm in an air. (B,C) SEM images at 50×, and 1,100× magnification. (C) The material inside of the crater has been melted from direct photothermal interaction with the laser light. 76
- FIGURE 5.12: SEM images of BegoStone stone phantoms at 600× and 650× magnification with (A) natural material, and after irradiation in (B) water, and (C) air environments using a 1908 nm wavelength laser. 77
- FIGURE 5.13: SEM images of BegoStone material at 650× magnification with (A) natural material, and laser irradiation at 1940 nm in (B) water, and (C) air. 78

FIGURE 5.14:	SEM image of UltraCal30 stone phantoms at 600× and 650× magnifications of (A) natural material, and laser irradiation at 1908 nm in (B) water, and (C) air.	79
FIGURE 5.15:	SEM image of UltraCal30 stone phantom at 1,100× - 1,600× magnifications of (A) natural material, and laser irradiation at 1940 nm in (B) water, and (C) air.	80
FIGURE 6.1:	Thulium fiber lasers operating at (A) 1908 nm and (B) 1940 nm.	90
FIGURE 6.2:	Temporal beam profiles of the two Thulium fiber lasers show a roughly similar shape, with each laser having an approximately 500 μs pulse length as measured from baseline to baseline.	91
FIGURE 6.3:	Representative images of uric acid stone samples used during experiments. All stones were of similar shape, size (6-9 mm diameter) and mass (~ 260 mg).	92
FIGURE 6.4:	Diagram of experimental set up used to measure stone ablation times and then calculate stone ablation rates. The optical fiber was placed in contact mode with the stone for each experiment. A water pump was used for saline irrigation. In each experiment, the total time for all stone fragments to fall through the sieve was measured.	93
FIGURE 6.5:	Ablation rates calculated from initial stone mass and total laser irradiation time for 1908 and 1940 nm TFLs (n = 10).	94
FIGURE 6.6:	Mass loss vs. radiant exposure for (A) 1908 nm and (B) 1940 nm thulium fiber lasers. Threshold values of 8 ± 7 and 5 ± 13 J/cm ² were calculated, respectively.	95
FIGURE 6.7:	Image of first bubble expansion (A) 1908 and (B) 1940 nm at ~ 120 μs into pulse duration for each laser.	96
FIGURE 6.8:	Bubble width dimensions for 1908 and 1940 nm laser wavelengths. Both bubbles produced two distinct expansions. However, the 1908 nm laser bubble did not fully collapse from first bubble, most likely due to a greater maximum length produced at end of laser pulse.	96
FIGURE 7.1:	Temporal beam profile of short pulse Ho:YAG laser setting. The pulse duration measures ~ 250 μs. The pulse shape has a sharp initial spike followed by a more uniform profile.	103

FIGURE 7.2:	TFL temporal beam profiles for long pulse laser setting (G3), showing a more uniform profile than Ho:YAG laser.	103
FIGURE 7.3:	Photograph of experimental setup (left) with a magnified image of the ablation chamber (right).	104
FIGURE 7.4:	Image of stitching microscope setup. Actuators move the sample while the CMOS camera acquires images. The images are later stitched together to analyze the fragment size.	106
FIGURE 7.5:	Ablation rate as a function of average power for TFL and Ho:YAG lasers. The P-value is labeled for each setting.	108
FIGURE 7.6:	Histograms of fragment size normalized by total number of fragments, for TFL (top row) and Ho:YAG (bottom row), with laser settings (G1, G2, G3) in columns. A greater number of large fragments (> 1.5 mm) were observed at higher pulse energies.	108

LIST OF ABBREVIATIONS

IR	Infrared
μ_a	Absorption Coefficient (cm^{-1})
δ	Penetration Depth (cm)
EM	Electro-Magnetic
τ_p	Laser Pulse Duration (μs)
σ	Speed of Sound in Tissue (mm/s)
LISL	Laser-Induced Shockwave Lithotripsy
α	Thermal diffusivity (cm^2/s)
ΔT	Change in Temperature ($^{\circ}\text{C}$)
c_p	Specific Heat Constant at Constant Pressure ($\text{J}/\text{kg}^{\circ}\text{C}$)
H_0	Radiant Exposure (J/cm^2)
z	Depth in Tissue (cm)
λ	Wavelength of Light (nm)
Ho:YAG	Holmium: Yttrium Aluminum Garnet
s	Seconds (Unit of Time)
J	Joules (Unit of Energy)
m	Meter (Unit of Distance)
Hz	Hertz (Cycles Per Second)
W	Watts (Unit of Power)
g	Gram (Unit of Mass)
m	Prefix milli- (10^{-3})
μ	Prefix micro- (10^{-6})
n	Prefix nano- (10^{-9})
k	Prefix kilo- (10^3)
M	Prefix mega- (10^6)
TFL	Thulium Fiber Laser
cm^{-1}	Inverse 10^{-2} Meters (Unit of Inverse Distance)
FL	Focal Length (mm)
Fr	French (Unit of Distance 1 mm equals 3 French)
OD	Outer-Diameter
ID	Inner-Diameter
CCD	Charge-Coupled Device
UA	Uric Acid
COM	Calcium Oxalate Monohydrate
In Vitro	Taking place outside a living organism
n	Sample Size

P	Results from t-test
T_p	Peak Temperature
Ω	Results from Arrhenius Integral (Quantifies Thermal Damage)
ζ	Frequency Factor (s^{-1})
E_a	Activation Energy (J/mol)
τ	Total Heating Time (s)
T	Temperature ($^{\circ}C$)
R	Universal Gas constant (8.32 J/K* mol)
T_{crit}	Critical Temperature ($^{\circ}C$)
CaP	Calcium Phosphate
SMA	Subminiature Assembly
S.D.	Standard Deviation
$\tau_{diffusion}$	Thermal Relaxation Time of Tissue
Bars	Unit of Pressure
SEM	Scanning Electron Microscope
HU	Hounsfield Unit (Unit Describing Radiodensity)
MAP	Magnesium Ammonium Phosphate
V	Voltage
NA	Numerical Aperture
Δt	Change in Time
min.	Minute (Unit of Time)
G1	Laser Setting 0.2 J / 50 Hz / 10 W
G2	Laser Setting 0.2 J / 80 Hz / 16 W
G3	Laser Setting 0.4 J / 80 Hz / 32 W
x	Variable for Fragment Size

CHAPTER 1: Introduction

1.1 Kidney Stone Disease

Kidney stone disease is a common and costly disorder, affecting ~10% of the U.S. population and about 50 million people worldwide [1][2]. Annual costs to the national health care system are estimated to be \$5.3 billion [3]. Each year, over 3 million patient visits to health care providers occur with over 500,000 treatments in emergency rooms for kidney stones [3]. In the U.S., almost 300,000 ureteroscopic laser lithotripsy procedures are performed annually, due to both a continuing increase in incidence of stone disease and increasing adoption of this technique [4]. Furthermore, over the last two decades, a marked increase in stone disease has been associated with changing demographics, diet, and lifestyle of our population [5]. Based on demographic and lifestyle modeling, continued and further increasing rates of stone disease are expected to occur in the coming decades [6].

Urinary stones are composed of inorganic and organic crystals combined with proteins. The cause of these formations varies significantly based on diet and genetics [7]. Calcium oxalate based stones account for 80% and uric acid 5-10% of all stones encountered in the clinic [7][8].



Figure 1.1. Photographs of different kidney stone compositions. Calcium oxalate based stones account for 80%, and uric acid 5-10% of all stones encountered in the clinic.

Urinary stones may stay in the kidney or travel down the urinary tract and become lodged in the ureter, reducing urinary flow, and causing severe discomfort and pain [9]. Smaller stones eventually pass, or are naturally flushed out of the urinary tract, however larger or oddly shaped stones may remain within the body, requiring immediate medical relief.

Treatment of kidney stones ranges from dietary approaches to percutaneous procedures [10]. Procedures such as shock-wave and laser lithotripsy have been found to be effective for small to moderate sized stones (< 15 mm). Shock wave lithotripsy is a completely non-invasive procedure that utilizes focused ultrasonic waves to fragment stones. While shock wave lithotripsy is successful, minimally invasive laser lithotripsy procedures are more effective at obliterating kidney stones with higher success rates and lower stone re-treatment rates [11][12][13][14].

1.2 Laser Lithotripsy

1.2.1 Ablation Mechanisms

Laser lithotripsy involves placing an ureteroscope, which has several ports (illumination, viewing, and working channel), through the urinary tract to the stone's

location. A low-OH, silica optical fiber is inserted through the working channel, for delivery of infrared laser radiation.

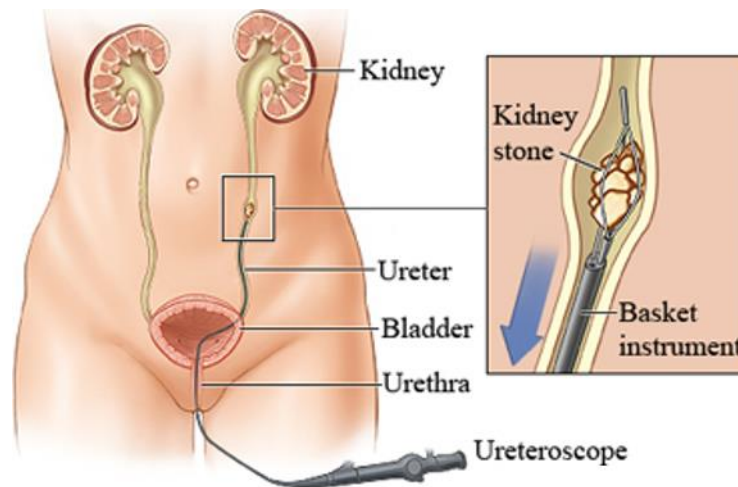


Figure 1.2. Image of an ureteroscopic procedure. An optical fiber would be placed in the same working channel as the basket instrument depicted. [healthy.kaiserpermanente.org]

The primary absorber of IR light is water. A measure of how much electromagnetic radiation a substance (water, kidney stone) can absorb is the absorption coefficient μ_a (cm^{-1}). The inverse of the absorption coefficient is called the optical penetration depth, δ (cm), and is a measure of the $1/e$ decay of the initial intensity. The absorption coefficient of water is an indicator of how well a particular wavelength will ablate kidney stones. Hard calculi directly absorb EM radiation, and the ablation rate is dependent on the stone material [15]. Figure 1.3 shows that the absorption coefficients of different dry kidney stones are similar. Previous studies have also shown that there are higher ablation rates for dry stones, stating that only direct absorption by the hard calculi is responsible for ablation [15]. This observation infers that the ablation mechanism is more complex than direct photoabsorption of hard calculi.

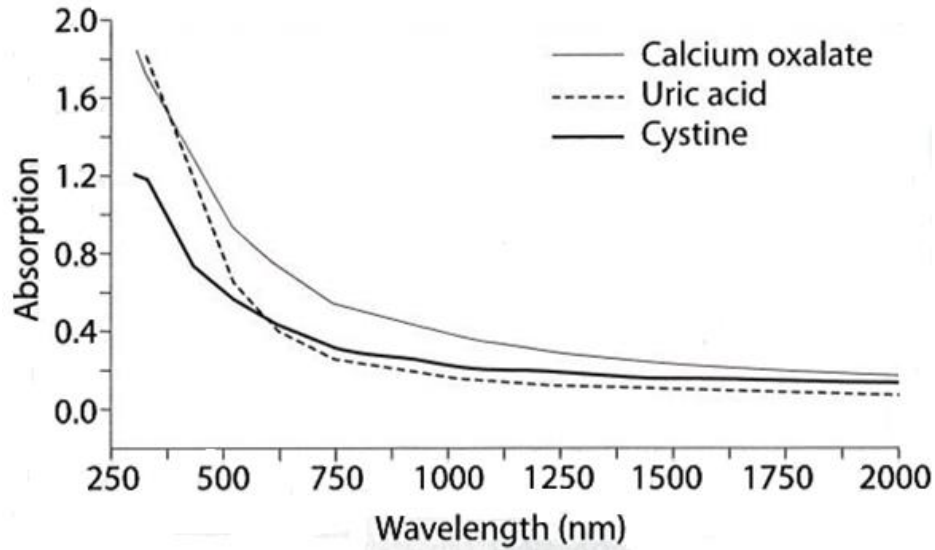


Figure 1.3. Absorption as a function of wavelength and kidney stone types. For near-IR wavelengths, absorption does not change significantly according to stone type [16].

1.2.2 Photomechanical ablation

The photomechanical ablation process occurs for lasers with short pulses ($< 1 \mu\text{s}$), and/or high irradiances ($< 10^8 \text{ W/cm}^2$). The transfer of laser energy into a mechanical shock wave that travels at the speed of sound or faster causes mechanical damage to hard calculi. Any laser pulse (τ_p) that is shorter than the time it takes for a stress wave to propagate out of the irradiation zone of the tissue, produces stresses. The accumulated stress propagates through the tissue with enough pressure to have ablative effects [17]. The criteria for a laser pulse to exhibit photomechanical effects is called “stress confinement”, shown in equation 1:

$$\text{(Equation 1.1)} \quad \tau_p < \frac{\delta}{\sigma},$$

where δ is the optical penetration depth (cm), τ_p is the laser pulse (s), and σ is the speed of sound in tissue (mm/s).

The actual mechanism of conversion from laser energy to mechanical or acoustical energy, in stress confined regions ($< 10^8 \text{ W/cm}^2$ irradiance), is a thermo-elastic response

of the tissue [17]. The pressure induced in the tissue is dependent on the localized change in temperature, which in turn is a function of the absorbed irradiance. During stress confinement conditions, the stress accumulated propagates in the form of an acoustic pressure wave, whose amplitude is dependent on the medium's absorption coefficient. The acoustic wave generates a sharp change in pressure which may induce a spherical cavitation bubble in a fluid medium the collapse of which creates another stress wave that contributes to ablation. The entire ablation process relies on thermo-elastic responses of the tissue and the water surrounding it.

Lasers with higher irradiances ($> 10^8 \text{ W/cm}^2$), under stress confinement conditions, can produce optical breakdown of the tissue [18]. A byproduct of optical break-down is plasma formation, and plasma expansion, which results in a shockwave and bubble formation whose collapse also generates a shockwave. The ablative effects are still mechanical, but the process is not thermo-elastic. The laser generates plasma that creates the mechanical energy exchange.

Short-pulsed lasers operating in the stress confined regions ablate hard tissue mechanically in a process called "laser-induced shockwave lithotripsy" (LISL). Mechanical ablation effects are generated by short pulsed (stress confined), high irradiance lasers, and utilize thermo-elastic, and intense pressure waves to mechanically fragment kidney stones.

1.2.3 Photothermal ablation

The long pulsed lasers described in this thesis do not operate in the stress confined region and therefore do not operate based on a photomechanical ablation mechanism. Direct absorption of near-IR irradiation can lead to non-radiative decay that produces heat, and

causes chemical decomposition and ablation. This photothermal ablation process occurs for lasers with longer pulse durations ($> 10^{-6}$ s), and low irradiances ($\ll 10^8$ W/cm²). The photothermal effect is caused from photoexcitation of a material that produces heat. To prevent thermal diffusion during the laser pulse throughout the tissue and undesirable collateral thermal damage, the laser pulse should be shorter than the time it takes for thermal energy to diffuse beyond the radiation site. A laser pulse duration that satisfies these conditions is called thermally confined. The quantitative criteria for thermal confinement is given by the following equation.

$$\text{(Equation 1.2)} \quad \tau_p < \frac{\delta^2}{4\alpha}$$

where α is the thermal diffusivity (cm²/s) of tissue, and δ is the optical penetration depth (cm) of the laser wavelength. When a laser pulse satisfies this thermal confinement criteria, laser ablation is localized, because the energy transfer (photons to thermal energy) occurs before the heat is able to diffuse beyond the irradiation site. During photothermal ablation in thermally confined regimes, the change in temperature in the tissue is related to the fluence absorbed by the tissue:

$$\text{(Equation 1.3)} \quad \Delta T(x, y, z) = \frac{\mu_a(\lambda)H_0(x,y)}{\rho c_p} e^{-\mu_a(\lambda)z}$$

where ΔT is change in temperature (°C), ρ is density of the material (kg/cm³), c_p is specific heat at constant pressure of the material (J/kg*°C), H_0 is radiant exposure (J/cm²), and z is the depth in the tissue (cm). The rise in temperature is responsible for chemical decomposition, melting, and ablation.

1.2.4 Laser Induced Vapor Bubbles

The kidney stone is typically immersed in a water environment during laser lithotripsy. IR radiation is highly absorbed by water. Although the procedure is primarily a photo-thermal ablation mechanism, there are also mechanical effects caused by high absorption in water [19]. Laser irradiation may cause the water inside the hard calculi to become superheated, creating high pressure in a localized region [20]. The abrupt change in pressure produces a mechanical stress wave, inside of the hard tissue, sufficient to ablate. Even if the stress wave is not sufficient to produce ablation, it does help facilitate the removal of already weakened material from the ablation site [15].

If there is water separating the near-IR radiation and the stone, the water will undergo rapid vaporization, causing the vapor pressure to increase, leading to a bubble formation. This phenomenon is often referred to as the “Moses effect”, because it separates the water and provides a path for the infrared energy to reach the target tissue (e.g. stone). The laser induced vapor bubble collapses once laser irradiation ceases. If there is a hard surface (e.g. kidney stone) in front of the vapor bubble, pressure asymmetry causes the bubble to collapse in a way that forms a counter jet near the surface [21]. This counter jet and the collapse of the bubble creates pressure waves that cause the stone to move in a direction opposite to the incoming irradiation. This phenomenon is called “retropulsion”. However, the resulting waves will not typically be strong enough to ablate mechanically [21].

The majority of laser lithotripsy procedures are conducted with a thermally confined laser (Holmium:YAG, wavelength: 2120 nm pulse duration: 250-1500 μ s, pulse energy: 200-2000 mJ). The primary mechanism that will be explored is the photothermal mechanism and its mechanical byproducts that either impede or facilitate ablation.

1.3 Holmium:YAG Laser

The solid-state, flashlamp-pumped, Holmium:YAG laser (Ho:YAG) has become the principal laser lithotripter in clinical use over the past 20 years. The laser operates at a wavelength of 2120 nm ($\mu_a=33 \text{ cm}^{-1}$) and utilizes 200-1000 μm core, low-OH, silica fibers for the procedure. Due to the flashlamp-pump configuration, the laser is pulsed, typically with settings of 0.2-2.0 J pulse energy, a 250-1500 μs pulse duration, pulse rates of 5-20 Hz, and average power of less than 20 W. There are high power versions of the Ho:YAG laser that utilize four Holmium doped rods pulsed in sequence. These lasers are able to operate at faster pulse rates up to 80 Hz, and larger average powers greater than 32 W.

Clinically, there are at least two common techniques used during laser lithotripsy, ‘fragmentation’ and ‘dusting’ ablation modes [22][23]. The ‘fragmentation’ mode is characterized by use of a high pulse energy (0.5 - 2.0 J) and low pulse rate (5 - 30 Hz). The stone is rapidly fractured into larger fragments. However, the ‘fragmentation’ operation mode also produces strong retropulsion effects. ‘Dusting’ ablation mode utilizes low pulse energy (0.2 - 0.4 J) and high pulse rate (50-80 Hz) laser settings. The ablated debris is characterized as ‘dust’ (< 0.5 mm) and can be easily passed spontaneously by the patient. The ‘dusting’ mode results in lower stone retropulsion, but the method may not be able to ablate harder stones requiring a ‘fragmentation’ mode technique or a higher pulse energy laser setting [24]. Currently, there is a clinical trend to move towards a dusting mode operation for laser lithotripsy [24][25].

The typical operating parameters of the Ho:YAG laser are made suitable for a ‘fragmentation’ mode technique. The large pulse energies generate pressures inside and outside of the stone, through the rapid evaporation of water. The large pressure inside the

stone causes fractures and “explosive” removal of stone material. The pressures generated also contribute to the stone’s retropulsion, which impedes ablation efficiency [26]. The high pulse energy, low pulse rate Ho:YAG laser operation translates into a more ‘chaotic’ ablation process. Strong stone retropulsion and ‘explosive’ stone fragmentation frequently results in the doctor chasing the stone throughout the urinary tract and can lead to a significant increase in operation time or the doctor losing small stone fragments, potentially resulting in higher stone re-treatment rates.

Thermal lensing affects limit the flash lamp pumped Ho:YAG laser to operation at pulse rates less than 30 Hz, causing the need of four laser rods in the high power Ho:YAG laser. The lower pulse rate also hinders the overall average power that can be delivered to the kidney stone, lowering ablation efficiency. The lower pulse rate of the low-power Ho:YAG also requires the laser to be operated at a higher pulse energy, requiring a larger effective volume of the gain material, which produces a multimode beam profile. The multimode beam profile in turn prohibits the use of optical fibers less than a 200 μm core diameter.

Larger core silica optical fibers affect efficiency of the procedure in several ways. First, the cross-sectional area consumes a large portion of the single ureteroscope working channel. This limits the rate of saline flow to clear the ablation site of debris, causing the doctor’s field of view to be obscured. An obscured field of view increases the probability of complications (i.e. potential perforation of the ureter wall) and an increase in operation time. Second, larger fibers decrease the effective energy density incident on the stone surface [27].

1.4 Thulium Fiber Laser

Use of fiber lasers for lithotripsy may eliminate some of these limitations. The experimental Thulium Fiber Laser (TFL) is currently being studied as a potential alternative to the Ho:YAG laser for the treatment of kidney stones [28][29][30][31][32][33]. Several recent clinical studies with the TFL have shown promise [34][35][36][37]. The TFL has several advantages over the Ho:YAG for lithotripsy.

Electronic modulation enables the TFL to be operated at pulse rates of 1-1000 Hz, 100 μ s to continuous wave (CW) pulse duration, and a pulse energy dependent on the pulse duration selected (e.g. 35 mJ for 500 μ s pulse duration). The lower pulse energies (35 mJ) and higher pulse rates (300 Hz) provide a “dusting” ablation effect, with less stone retropulsion [38]. This operation mode also allows the TFL to safely operate at higher average powers (~10 W for TFL versus 3 W for Ho:YAG). Higher average powers with reduced stone retropulsion translate into improved TFL ablation efficiency during lithotripsy.

The TFL wavelength at 1908 nm also more closely matches a high temperature water absorption peak at 1910 nm when compared to the Ho:YAG wavelength of 2120 nm [39][40][41] (Figure 1.4). Since the primary absorber in the stone is water during laser lithotripsy, the TFL’s greater high temperature water absorption coefficient (155 cm^{-1}) has been found to produce a 4x lower ablation threshold for kidney stones when compared to the Ho:YAG laser (33 cm^{-1}) [39][40][41]. A decrease in ablation threshold translates into an increase in overall ablation efficiency.

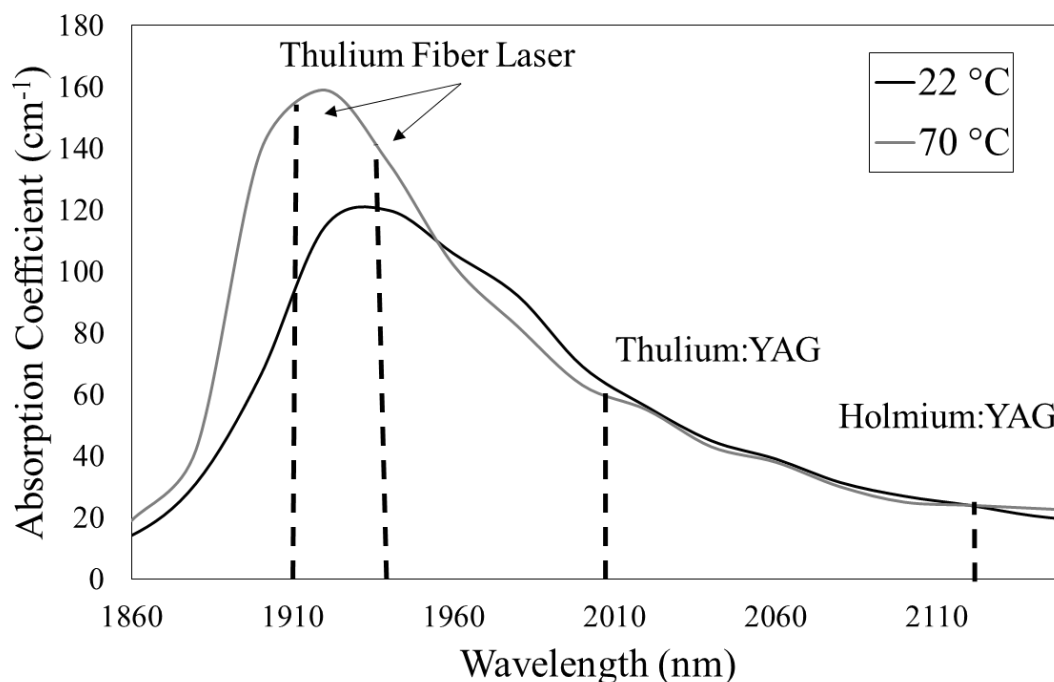


Figure 1.4. The TFL room temperature water absorption peak at 1940 nm shifts to about 1910 nm at higher temperatures. The major emission lines of the TFL at 1908 and 1940 nm match this shifting peak more closely than the Ho:YAG laser wavelength at 2120 nm [39][40].

TFL light originates in an 18 μm core fiber, producing a low number of transverse modes, and providing a uniform spatial beam profile. The uniform beam enables focusing and coupling of IR energy into smaller optical fibers (50, 100, and 150 μm cores) than used during Ho:YAG lithotripsy procedures (≥ 200 μm core) [42]. Smaller optical fibers provide several potential advantages including higher irradiance (W/cm^2) on the stone. The fiber also consumes a smaller cross-sectional area in the single working channel of the ureteroscope, translating into a faster saline flow rate during the procedure, and allows faster dissipation of heat from the irradiation zone, as well as better visibility for safety [44].

1.5 Current Research

The versatility of the TFL leads to a large parameter space to be explored to enhance ablation efficiency. The methods for obtaining an increase in ablation efficiency vary as

well. A primary concern is stone retropulsion, which can be mitigated in several ways. Use of stone stabilization devices enables the laser to be operated at high average power without stone retropulsion. However, these devices consume valuable space in the ureteroscope working channel, thus lowering saline irrigation rates and visibility, and they may not always be fully effective at stabilizing the stone [43][44]. An improved understanding of the mechanism that causes retropulsion may facilitate optimization of laser parameters to reduce retropulsion, while preserving adequate stone ablation rates. For example, it has been found empirically that longer laser pulse durations decrease stone retropulsion [26]. Understanding how the laser parameters affect vapor bubble formation may also lead to an increase in ablation efficiency.

The TFL has the ability to be electronically modulated, producing greater average powers than the Ho:YAG laser. While use of higher laser powers may increase ablation rates, it may also increase the probability of perforation of the ureter or damage to urinary tissue [45]. The optical power used to ablate stones must be adjusted such that there is a large safety margin for the patient, without compromise in ablation efficiency.

An increase in ablation efficiency translates into a decrease in operation time, surgical risk, and cost for the patient. This can be achieved by optimizing the TFL parameters, inclusion of stone stabilization devices, and a better understanding of the ablation mechanisms.

The purpose of this dissertation is to understand the TFL's ablation mechanisms and provide solutions to increase overall kidney stone ablation efficiency without sacrificing patient safety.

In chapter 2, TFL stone ablation was measured as a function of pulse rate with and without use of a stone basket. TFL ablation rates of different stone types using both a clamp, and a commonly used retropulsion stabilization device (stone basket) were compared.

In chapter 3, TFL and Ho:YAG laser were compared in an in vitro ureter model. TFL ablation rates increased sufficiently for clinical use, due to an increase in pulse rate (average power). Both operation time and laser irradiation time were recorded along with temperature safety data. Temperature data was used to determine if undesirable thermal damage to surrounding tissues (e.g. ureter wall) was a concern.

In chapter 4, TFL induced vapor bubble dynamics were studied. The expansion and collapse of the laser induced bubble is a main source of stone retropulsion. This effect causes the stone to move away from the irradiation site, leading to a surgeon to chase the stone, increasing operation time and also increasing the probability of losing a fragment inside the urinary tract. Previous studies have quantified laser induced bubble dimensions for different lasers, wavelengths, and operational settings. The TFL's wavelength of 1908 nm and low pulse energy/high pulse rate "dusting" mode laser settings (35 mJ at 300 Hz) is an unexplored regime. A wide range of laser peak power settings were explored and compared to Ho:YAG. The purpose of the study was to examine bubble dimensions and dynamics to determine the optimal TFL laser settings for both high ablation rate and low stone retropulsion.

In chapter 5, kidney constituent particle size, and morphology was examined. A connection between the stone environment and primary ablation mechanism was determined. Previous studies have found a decrease in ablation rate when comparing

ablation between air and water environments. This study used SEM images to determine primary ablation mechanism for different kidney stone compositions in an air and water environment.

In chapter 6, ablation rate as a function of wavelength was studied. Long pulse laser lithotripsy operates on a photothermal mechanism. The energy absorbed by a medium is a function of the optical absorption coefficient, μ_a (cm^{-1}). However, the optical absorption coefficient changes dynamically with pressure and temperature. Newer commercial Thulium fiber lasers operate at a 1940 nm wavelength, which differs from the 1908 nm output. This difference results in an approximate 20% decrease in the high temperature water absorption coefficient. The purpose of this study was to analyze the difference in ablation rates, and ablation threshold as a function of the two laser wavelengths.

In chapter 7, fragmentation size of stone debris was studied as a function of laser parameters between the Ho:YAG and TFL lasers. Ho:YAG typically operates in a 'fragmentation' mode with high pulse energy and low pulse rate. However, with new Ho:YAG laser advances the laser is able to operate with the same high pulse rate (50-80 Hz) low pulse energy (50-400 mJ) laser settings as the TFL. Previous studies were not able to operate both the TFL and Ho:YAG laser at the same laser parameters. The purpose of this study was to compare both TFL and Ho:YAG ablation rates at the same laser parameters, while analyzing the fragment size generated from both lasers.

CHAPTER 2: Rapid Thulium Fiber Laser Lithotripsy at High Pulse Rates

2.1 Introduction

The rate of stone destruction, or ablation rate, is a significant measure of efficiency. Ho:YAG laser energy propels stones away from the fiber tip (resulting in retropulsion) unless the stone is fixed or impacted by surrounding tissues within the ureter or kidney. Stone retropulsion is a clinically significant phenomenon, as it causes the surgeon to “chase” the stone, resulting in a decrease in ablation efficiency, increase in surgical time and possible collateral tissue trauma [26][46][47][48][49][50][51]. Most stone clearance failures can be attributed to stone fragment retropulsion [47]. Therefore, elimination of retropulsion during lithotripsy is desirable. Several endoscopic devices (balloons, stone cones, accordions, baskets, and thermosensitive polymeric gel plugs) have been used in the clinic to minimize stone retropulsion during lithotripsy [52].

Currently, the low-power Ho:YAG is limited to low pulse rates (< 30 Hz), due to the flash-lamp pump design. The only way to increase average power is by increasing the pulse energy, which leads to high retropulsion [46]. The TFL can be electronically modulated, with variable pulse rates (1-1000 Hz). The average power can be increased by increasing the pulse rate of the laser, which limits retropulsion by keeping pulse energy low. However, previous studies observed that stone phantom retropulsion was > 2 mm when operating the TFL at pulse rates greater than 150 Hz, without assistance of a stone stabilization device [38]. The purpose of this study is to use a clamp or stone basket to minimize stone retropulsion, and thus allow TFL operation at pulse rates > 150 Hz for more efficient stone ablation.

2.2 Methods

2.2.1 Thulium Fiber Laser Parameters

A 100-Watt Thulium fiber laser (TLR 100-1908, IPG Photonics, inc., Oxford, MA) (TFL) with a center wavelength of 1908 nm was used in these studies. The continuous-wave TFL was electronically modulated using a function generator (DS345, Stanford Research Systems, Sunnyvale, CA) to operate in long-pulse mode, producing 500- μ s pulses for lithotripsy studies, similar to conventional Ho:YAG laser pulse lengths of 350-700 μ s. The TFL produced a Gaussian mode spatial beam profile, originating from an 18- μ m-core thulium-doped silica fiber, with a built-in collimator providing a 5.5-mm-diameter output beam. A 25-mm-FL plano-convex calcium fluoride lens was then used to focus the collimated TFL beam down to a $1/e^2$ spot diameter of ~ 25 μ m, for coupling into a standard, low-OH, 100- μ m-core silica optical fiber (AFS105/125, Thorlabs, Newton, NJ), for use in stone ablation studies. All experiments were performed with a TFL output pulse energy of 35 mJ, pulse duration of 500 μ s, and pulse rates of 10-500 Hz.

2.2.2 Kidney Stone Samples

Human uric acid (UA) and calcium oxalate monohydrate (COM) stone samples with greater than 95% purity were obtained from several stone analysis laboratories including LabCorp (Oklahoma City, OK), Louis C. Herring & Co (Orlando, FL) and Carolinas Medical Center (Charlotte, NC). These stone samples were chosen because calcium oxalate and uric acid stones comprise $\sim 80\%$ and $\sim 10\%$, respectively, of all stone compositions encountered in the clinic [7]. Stone samples were desiccated in an oven for 30 min. and then weighed with an analytical balance (Model AB54-S, Mettler-Toledo,

Switzerland) both before and after lithotripsy experiments to determine their mass loss. All experiments were performed with the stone samples completely submerged in a saline bath.

2.2.3 Experimental Setup

Two different techniques were used for stabilizing the stone during laser lithotripsy. The first method was designed to be a simplified representation of an impacted stone, that is embedded in tissue and not free to move on its own. This technique involved mechanically clamping the stone to eliminate stone repulsion and to determine ablation rates under those specific conditions (Figure 2.1). During this procedure, the laser fiber was kept in close contact with the stone and manually scanned over the stone surface.

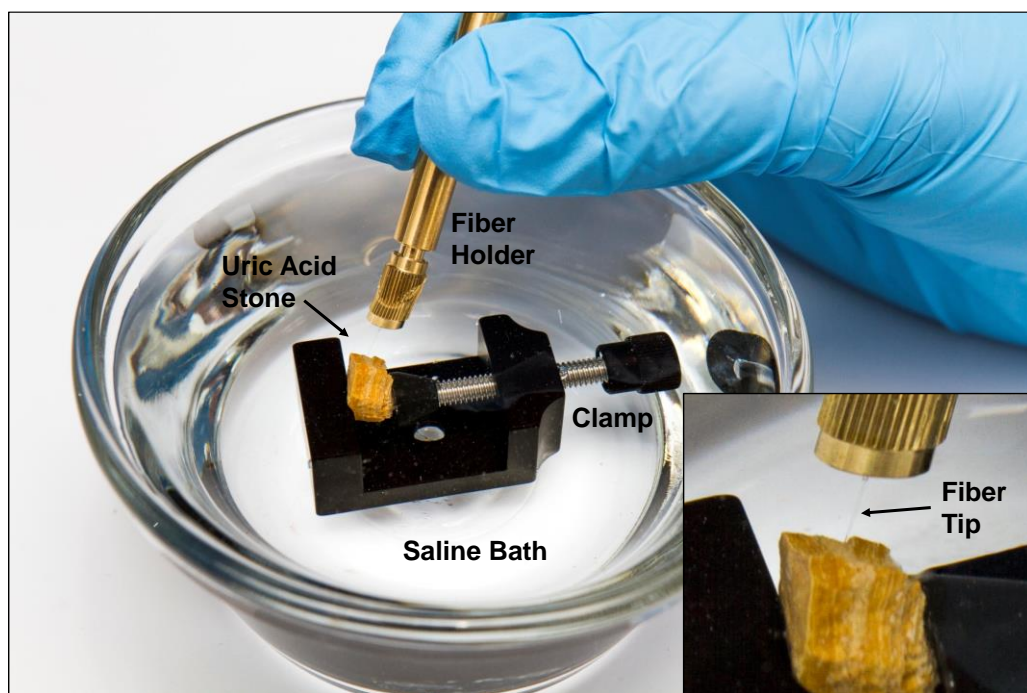


Figure 2.1. Experimental setup for TFL lithotripsy with a uric acid stone immobilized in a clamp and submerged in a saline bath.

The second method involved using a 1.9-Fr (0.6-mm-OD) stone basket (Zero Tip Nitinol Stone Retrieval basket, Boston Scientific, Natick, MA) as a standard clinical approach for stabilization of a stone that would otherwise be free to migrate in the urinary

tract. The experimental setup consisted of a rigid ureteroscope (9.5-Fr ID, Karl Storz, Germany) attached to a light source (X7000, Stryker Endoscopy, San Jose, CA), CCD camera (1188HD, Stryker), and monitor. The laser fiber and stone basket were inserted through the same ureteroscope working channel, and then placed in contact with the urinary stone sample, which was submerged in a saline bath (Figure 2.2). Illumination from the endoscope and a magnified image from the CCD camera, connected to a monitor, were used to observe the laser lithotripsy procedure. Although the fiber was constrained by the endoscope working channel, the stabilized stone was still free to rotate and translate slightly inside of the stone basket during the procedure.

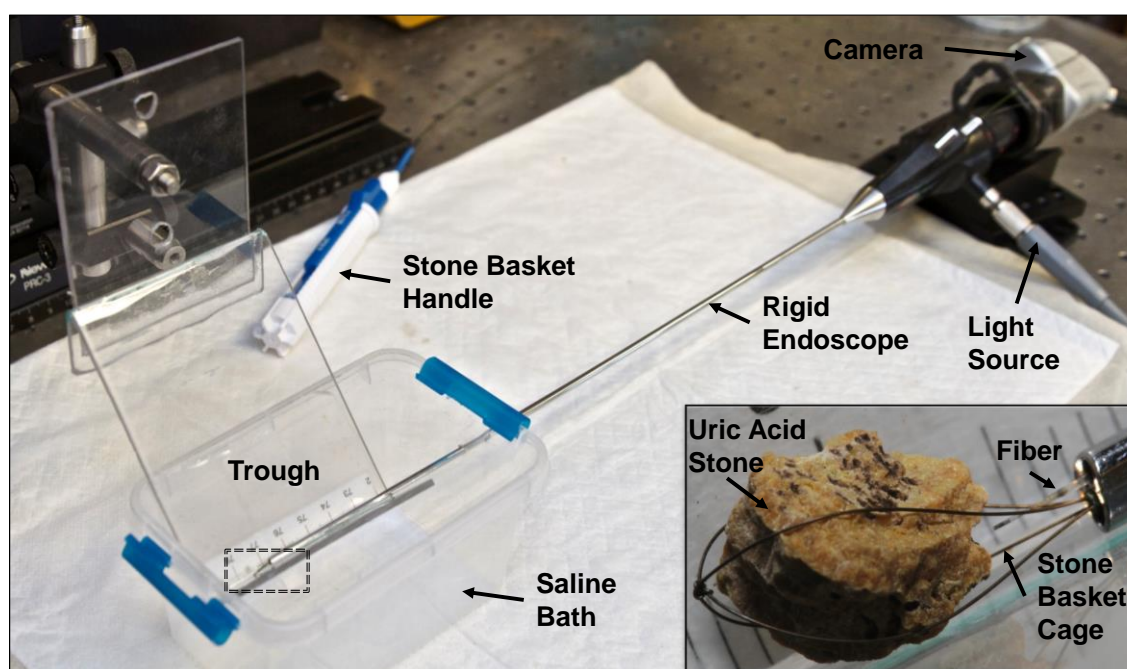


Figure 2.2. Experimental setup for TFL lithotripsy, showing rigid endoscope, optical fiber, and stone basket for grasping a uric acid stone submerged in a saline bath.

For both procedures, stone vaporization rate ($\mu\text{g/s}$) was calculated by determining net mass loss of stones as a function of laser irradiation time. The procedure was only paused momentarily under circumstances in which stone dust or bubble formation impeded the field of view. All residual stone samples > 2 mm were collected in a sieve and included in

the stone mass measurements, consistent with the clinical endpoint for successful stone fragmentation, since small stone fragments (< 2 mm) can be naturally passed through the urinary tract. A minimum of five samples were tested for each data set and the mean \pm standard deviation recorded.

2.3 Results

Figure 2.3 shows TFL stone ablation rates as a function of both stone type and laser pulse rate. The pulse energy was fixed at 35 mJ while the pulse rate ranged from 10-500 Hz, translating into average powers of 0.35-17.50 W. TFL ablation of UA stones was 2-3 times faster than COM stones, due in part to differences in stone composition. However, both stone types exhibited a strong linear relationship between TFL pulse rate and stone ablation rate. The increase in TFL pulse rate compensated in part for the low pulse energy output (35 mJ), resulting in higher stone ablation rates than observed in our previous studies [18].

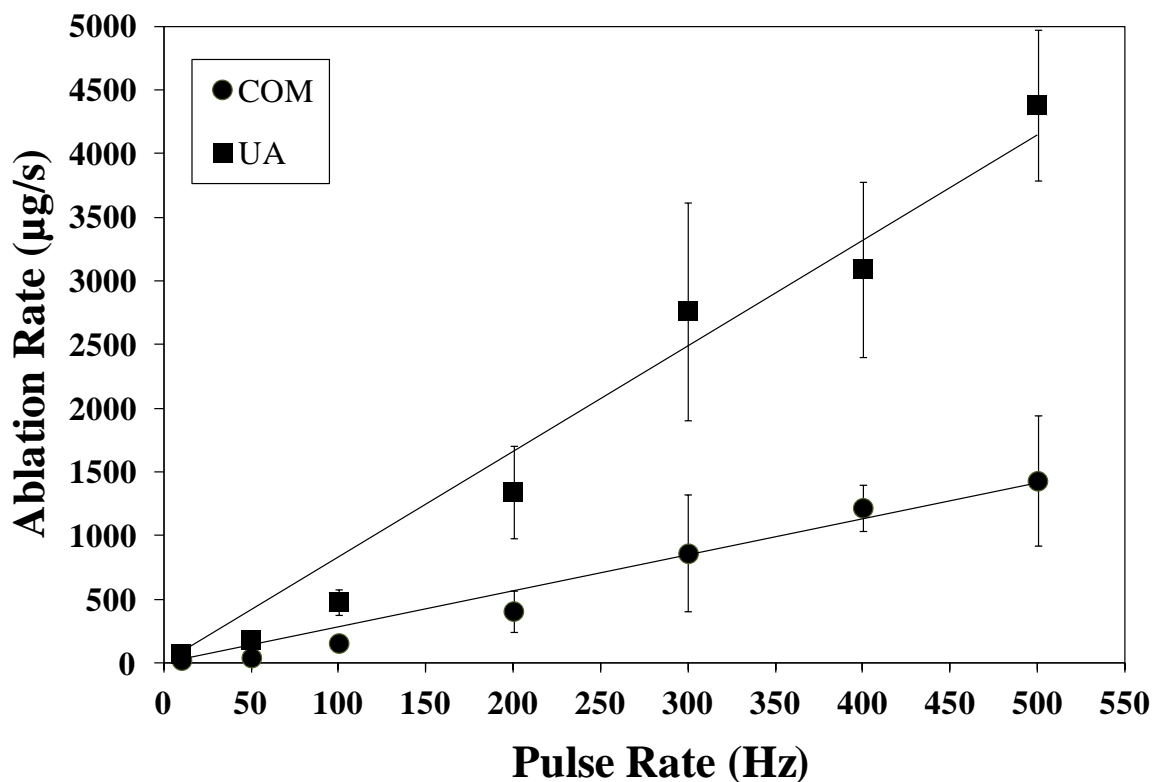


Figure 2.3. TFL stone ablation rate as a function of stone type and laser pulse repetition rate. TFL pulse energy and pulse length were fixed at 35 mJ and 500 μ s, respectively.

Table 2.1 summarizes TFL stone ablation rates (at 500 Hz) as a function of stone type and stabilization device (clamp or basket). Use of a clamp resulted in higher stone ablation efficiency due to several factors. The stone was completely stabilized, allowing the manually scanned fiber tip to remain in constant close contact with the stone surface, so that every laser pulse delivered to the stone contributed to stone ablation. Use of the stone basket resulted in lower stone ablation rates by a factor of about two due to the limited freedom of movement of the fiber tip inside the rigid endoscope, and the need to periodically reposition the fiber during the procedure, thus resulting in some laser pulses being delivered into the saline bath rather than to the stone surface. Furthermore, the stone was free to move slightly within the basket, which impacted the working distance between fiber tip and stone surface, and hence the ablation rate as well, during the procedure.

Table 2.1. TFL stone ablation rates (mg/s) as a function of stone type and stone stabilization device.

	Clamped Stone	Stone Basket
COM	1.4 ± 0.5	0.7 ± 0.2
UA	4.4 ± 0.6	1.7 ± 0.3

The large error bars for some of the data points in Figure 2.3 and Table 2.1 may be attributed to several factors, including variable stone mass density and surface texture, small variations in laser irradiation time, and human error during translation of the laser fiber across the stone surface.

Figure 2.4 shows representative photographs of a human UA stone before and after TFL lithotripsy. The initial stone dimensions and mass provided are typical of stones encountered in the clinic. Laser irradiation time and total treatment time are also given. The UA stone was broken down into fragments < 2 mm diameter in an irradiation time of only 24 s and a total treatment time of only 65 s.

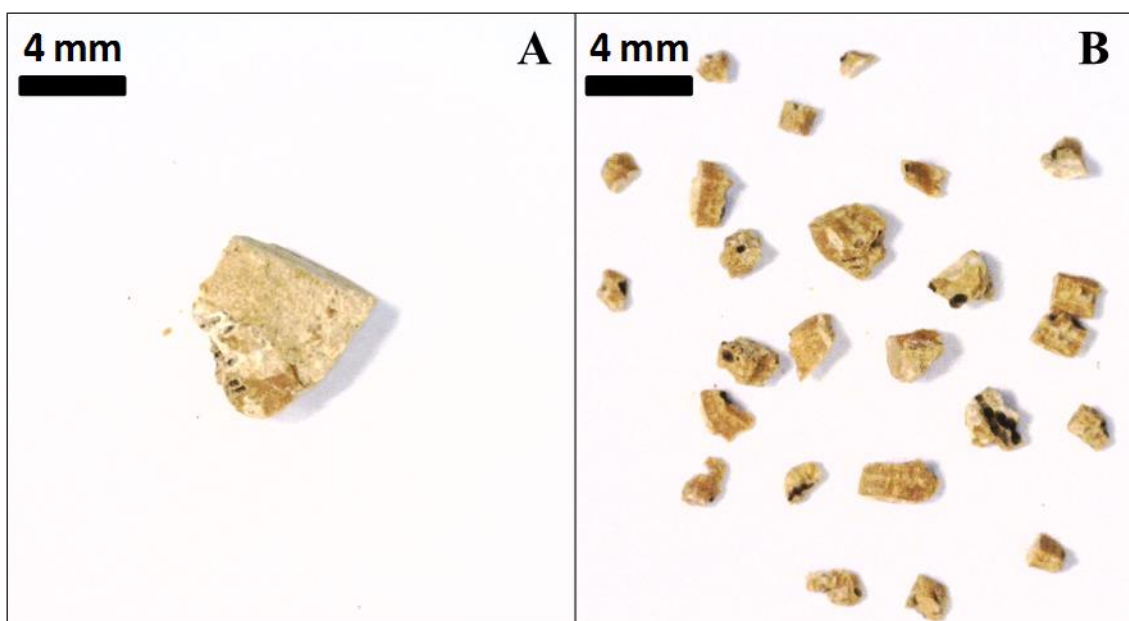


Figure 2.4. Representative uric acid stone (a) before and (b) after TFL lithotripsy with 35 mJ, 500 μ s, and 500 Hz. Total laser irradiation time was 24 s and total treatment time was 65 s. Initial stone size was 8 x 4 x 5 mm and initial stone mass was 135 mg.

2.4 Discussion

In previous reports, stone phantom retropulsion during TFL lithotripsy became significant at pulse rates greater than 150 Hz. However, limiting TFL operation to lower pulse rates unnecessarily limits stone ablation rates as well. It was also concluded, incorrectly, in previous studies that TFL operation at higher pulse rates resulted in a plateau in the clamped stone ablation rates above about 100 Hz [38]. As observed in Figure 2.3 in this study, the stone ablation rate is directly proportional to the TFL pulse rate, and ablation rate continued to increase linearly in the entire range studied, from 10-500 Hz.

This study demonstrated that the TFL can be operated at ultra-high pulse rates up to 500 Hz, when used in combination with a commercially available clinical stone basket device. The stone basket acted to stabilize the stones, minimizing retropulsion, and thus providing more efficient stone vaporization. It is estimated from these results that a typical stone size encountered in the clinic (5-8 mm diameter), could be treated in 1-2 min for UA stones and 3-5 min for COM stones, with the clinical endpoint being fragmentation into stone fragments ≤ 2 mm diameter, for subsequent natural passage through the urinary tract.

Direct comparisons between the clinical Ho:YAG laser lithotripter and the experimental TFL are difficult to perform since the two lasers have fundamentally different operation parameters. The Ho:YAG laser is typically operated at high pulse energy (0.5 - 2 J) and low pulse rates (5-20 Hz), while our electronically modulated TFL is limited to operation at low pulse energies (35 mJ) for a fixed pulse duration (500 μ s), but is capable of high pulse rates (500 Hz).

Despite these differences in laser parameters, it is still informative to provide an estimate for comparison of ablation rates between the TFL and Ho:YAG lasers under the most

similar conditions available. For example, from Table 2.1, the TFL ablation rate (at 500 Hz) for clamped COM stones measured 1.4 ± 0.5 mg/s. Previous studies reported by our laboratory also measured Ho:YAG ablation rates for clamped COM stones. In these studies, the Ho:YAG pulse rate was fixed at 10 Hz, and Ho:YAG pulse energy was gradually increased. The Ho:YAG ablation rate measured 1.0 ± 0.2 mg/s and 1.7 ± 0.5 mg/s at laser pulse energies of 700 mJ and 1000 mJ, respectively [53]. These values demonstrate that COM ablation rates for TFL and Ho:YAG lasers are comparable when the lasers are operated with their normal laser parameters and under similar conditions.

2.5 Conclusion

The experimental Thulium fiber laser was studied as an alternative laser to the standard, clinical Holmium:YAG laser for ablation of kidney stones. TFL operation at pulse rates up to 500 Hz resulted in rapid fragmentation of human uric acid and calcium oxalate monohydrate urinary stones at ablation rates that may be practical for future translation into the clinic.

CHAPTER 3: Comparison of Thulium Fiber and Low Power Holmium:YAG Laser Lithotripsy in an In Vitro Ureter Model

3.1 Introduction

In chapter 2, it was observed that TFL kidney stone ablation rates scale linearly with pulse rate, and when operated at high pulse rates up to 500 Hz, the TFL is capable of rapid stone ablation [44]. However, these studies did not take into account stone retropulsion, in a free moving environment, or active saline irrigation during the procedure, and there was also no comparison with the conventional Holmium laser, currently the gold standard laser lithotripter in the clinic. The objective of this study is therefore twofold: (a) to compare TFL and Holmium laser times and total operation times necessary to fragment similar stones in an *in vitro* ureter model, and (b) to record saline temperatures near the stone sample in order to provide feedback on safety margins for potential future clinical application.

3.2 Methods

3.2.1 Thulium Fiber Laser Parameters

A 100-Watt experimental Thulium fiber laser (TLR 110-1908, IPG Photonics, Oxford, MA) with a center wavelength of 1908 nm was used in these studies. The continuous-wave TFL was electronically modulated using a function generator (DS345, Stanford Research Systems, Sunnyvale, CA) to operate in long-pulse mode, producing 500- μ s pulses for lithotripsy studies, similar to conventional Holmium laser pulse lengths of 350-700 μ s. The TFL produced an approximately Gaussian, near single-mode beam profile, originating from an 18- μ m-core thulium-doped silica fiber, with a built-in collimator providing a 5.0-mm-diameter output beam. A 25-mm-focal-length calcium fluoride lens was used to focus

the TFL beam down to a $1/e^2$ spot diameter of $\sim 25 \mu\text{m}$, for coupling into a standard, disposable, low-hydroxyl, 100- μm -core silica optical fiber (AFS105/125, Thorlabs, Newton, NJ). All stone ablation experiments were performed with TFL output pulse energy of 35 mJ, pulse duration of 500 μs , and variable pulse rates of 150, 300, or 500 Hz.

3.2.2 Holmium:YAG Laser Parameters

A 20-Watt, clinical Holmium:YAG laser (Medilas H20, Dornier MedTech, Wessling, Germany) with a center wavelength of 2100 nm was used in these studies for direct comparison with the TFL. The Holmium laser was used with a standard 270- μm -core clinical, low-OH silica optical fiber (RFID Holmium Lightguide, Dornier MedTech). The laser was operated with standard clinical parameters, including pulse energy of 600 mJ, pulse duration of 350 μs , and pulse rate of 6 Hz. Laser pulse energy was measured using a pyroelectric detector (ED-200, Gentec, Canada) connected to an energy/power meter (EPM1000, Molectron, Portland, OR).

3.2.3 Urinary Stone Samples

All stone samples were composed of 60% calcium oxalate monohydrate and 40% calcium phosphate (Figure 3.1). These stones were chosen because calcium oxalate stones are common and comprise about 80% of all stone compositions encountered in the clinic [7][8]. All of the stone samples originated from a single patient, had consistent mass (40-100 mg) and size (4-5 mm diameter) and were available in large quantities. Stone samples were desiccated in an oven for 15 min. and then weighed with an analytical balance (Model AB54-S, Mettler-Toledo, Columbus, OH) before lithotripsy experiments to determine their initial mass. Stone samples were then placed in the ureter model, immersed in a saline bath

and experiments were conducted immediately upon rehydration. A total of 12 stone samples were used for each set of laser parameters.



Figure 3.1. Human urinary stone samples with composition of 60% calcium oxalate monohydrate and 40% calcium phosphate used in all of these studies.

3.2.4 Experimental Setup

A 6-mm-inner-diameter tube with integrated 1.5 mm mesh sieve and micro-thermocouple was used as a simple *in vitro* ureter model in these studies (Figure 3.2). Kidney stones were placed inside of the tube and rested on the sieve, with the entire ureter model submerged in a saline bath. The distal tip of a flexible digital video-ureteroscope (URF-V, Olympus, Southborough, MA) was then placed inside of the tube. The optical fiber was inserted through the 3.6 Fr (1.2 mm) single working channel of the ureteroscope and positioned in contact with the urinary stone sample, under magnification. Constant saline irrigation at room temperature (22 °C) was provided by a saline bag elevated 100 cm above the experimental setup. Saline flow rates through the ureteroscope working channel with the 100- μm -core (244- μm -OD) TFL and 270- μm -core (464- μm -OD) Holmium laser

fibers measured 22.7 ml/min and 13.5 ml/min, respectively. It should be noted that there is always continuous saline irrigation during endoscopic laser lithotripsy in the clinic, primarily to clear stone dust and maintain visibility of the stone in the surgical field during the procedure. All stone samples were free to move around inside the ureter model during the studies. An experienced, practicing urologist (Dr. Pierce Irby, McKay Department of Urology, Carolinas Medical Center, Charlotte, NC) performed all of the laser lithotripsy experiments. The stone sample was irradiated with the laser until all ablated fragments were sufficiently small (< 1.5 mm diameter) to pass through the mesh of the sieve. Total laser times and operation times were recorded for each experiment. “Laser time” was defined as the total time that the laser was on. “Operation time” was defined as the total time from laser initiation until the final stone fragments passed through the sieve, including both laser time and any additional time used to re-adjust the fiber position or clear the visual field, when the laser was momentarily not in use. Videos of each stone ablation experiment were also recorded for subsequent analysis.

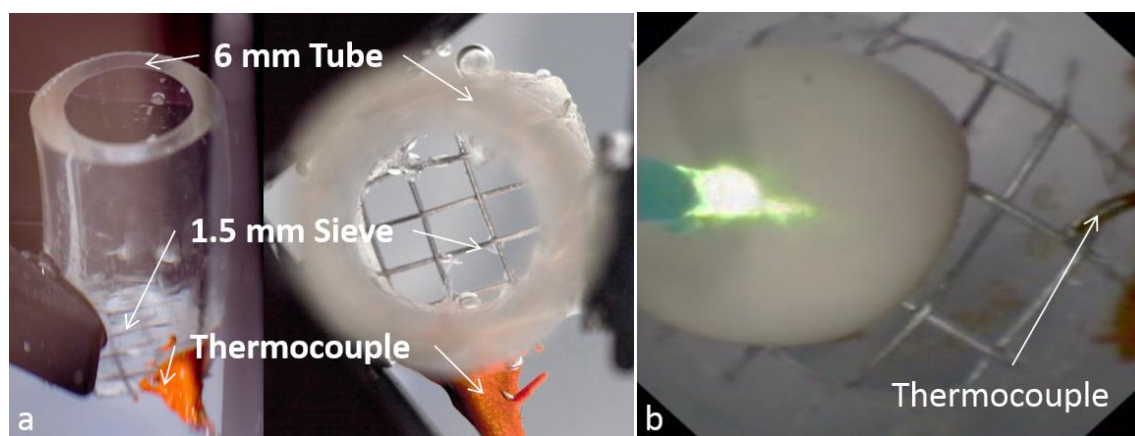


Figure 3.2 (a) Experimental setup showing the ureter model, including 6-mm-inner-diameter tube, 1.5 mm mesh sieve, and micro-thermocouple. (b) Close-up view through the flexible ureteroscope of the fiber tip and stone sample during the experiment. The thermocouple was placed 3 mm from the center of the tube (along the tube wall) and 1 mm above the mesh sieve.

3.2.5 Thermocouple Temperature Measurements

Temperature monitoring was performed during all experiments. An insulated, 125- μm -diameter, micro-thermocouple (Type T, Omega, Stamford, CT) was positioned 1 mm above the sieve mesh and 3 mm from the center of the tube (at the tube wall), to monitor and record saline temperatures in close vicinity to the stone sample during laser ablation (Figure 3.2). A digital data acquisition system (OM-USB-TC, Omega) connected to the micro-thermocouple and controlled by a laptop personal computer was used to record all temperature data. The peak temperature from each individual study ($n = 10$) of a given data set was recorded, and then the mean and standard deviation of all of these peak temperatures was calculated and provided in Table 3.1. Great care was taken to prevent direct irradiation of the thermocouple with laser energy from the fiber optic tip, so as to avoid both potential damage to the thermocouple and erroneous temperature values from direct absorption of laser energy by the thermocouple.

3.3 Results

3.3.1 Laser and Operation Times

Mean laser and operation times during Holmium:YAG and TFL lithotripsy experiments are summarized in Table 3.1. The laser was periodically turned off to allow re-positioning of the fiber and stone debris clearance for improved visibility during the procedure, which resulted in the reported differences between laser and operation times. Initial stone mass was similar for all data sets and measured 59 ± 4 mg for Holmium laser data set, and 55 ± 15 mg, 60 ± 15 mg, and 66 ± 10 mg for TFL pulse rates of 150, 300, and 500 Hz, respectively. Holmium laser times measured 167 ± 41 s. TFL times measured 111 ± 49 s, 39 ± 11 s, and 23 ± 4 s, for pulse rates of 150, 300, and 500 Hz, respectively. As TFL pulse

rate was increased from 150 to 500 Hz, laser times decreased since the laser pulses were more rapidly delivered to the stone. Operation times were also recorded. Holmium laser operation time measured 207 ± 50 s. TFL operation times measured 116 ± 54 s, 54 ± 22 s, and 60 ± 22 s for pulse rates of 150, 300, and 500 Hz.

Both stone laser times and total operation times were significantly shorter for the TFL at all pulse rates (150, 300, and 500 Hz) than for the Holmium laser ($P < 0.05$). However, there was no statistical difference between 300 and 500 Hz TFL operation times ($P = 0.37$). These overall findings were due to a number of factors, including TFL operation at higher power densities, higher pulse rates, higher average powers, and reduced stone retropulsion, as described below.

The two lasers produced two different stone motion effects. The TFL with lower pulse energy and higher pulse rate produced a vibrational effect, which led to the stone oscillating in the same relative position. The Holmium laser exhibited a retropulsion effect, causing the stone to recoil within the confines of the ureter model, and making it more difficult to ablate the stone in an efficient manner, which was reflected by longer Holmium laser and operation times provided in Table 3.1. It should be noted, however, that the presence of the sieve may have distorted to some degree the normal retropulsion movement typically encountered in the clinic.

Table 3.1. Total laser and operating times to fragment 4-5 mm diameter calcium oxalate stones into fragments smaller than 1.5 mm, and peak saline temperatures measured during experiments.

Laser	Laser Time (s)	Operation Time (s)	Peak Temperature (°C)	N
Holmium:YAG	167 ± 41	207 ± 50	24 ± 1	12
TFL				
150 Hz	111 ± 49	116 ± 54	33 ± 3	12
300 Hz	39 ± 11	54 ± 22	33 ± 7	12
500 Hz	23 ± 4	60 ± 22	39 ± 6	12

* Baseline temperature was 22 °C.

3.3.2 Saline Temperatures

Mean peak saline temperatures (defined as average of n=10 individual peak temperatures for each data set) during Holmium:YAG and TFL lithotripsy experiments were calculated to be 24 ± 1 °C for Holmium, and 33 ± 3 °C, 33 ± 7 °C, and 39 ± 6 °C for TFL at pulse rates of 150, 300, and 500 Hz, respectively (Table 3.1). Temperatures during TFL lithotripsy were significantly higher than for Holmium laser ($P < 0.05$). The results also suggest that a decrease in TFL pulse rate from 500 to 300 Hz also translated into lower average power and lower saline temperatures ($P = 0.01$), and thus provides an additional safety margin for potential future clinical studies.

Temperature history graphs showing the worst case (highest peak temperature) during Holmium and TFL lithotripsy experiments are provided in Figure 3.3. The variation in temperatures in all of the graphs is due to a number of factors, including the laser parameters, experimental setup, and surgical technique. Specifically, variable laser pulse rates were used translating into different cooling rates in between delivery of individual laser pulses. The ureteroscope was handheld and the distance between fiber optic tip and thermocouple location also varied constantly, affecting temperature readings as well.

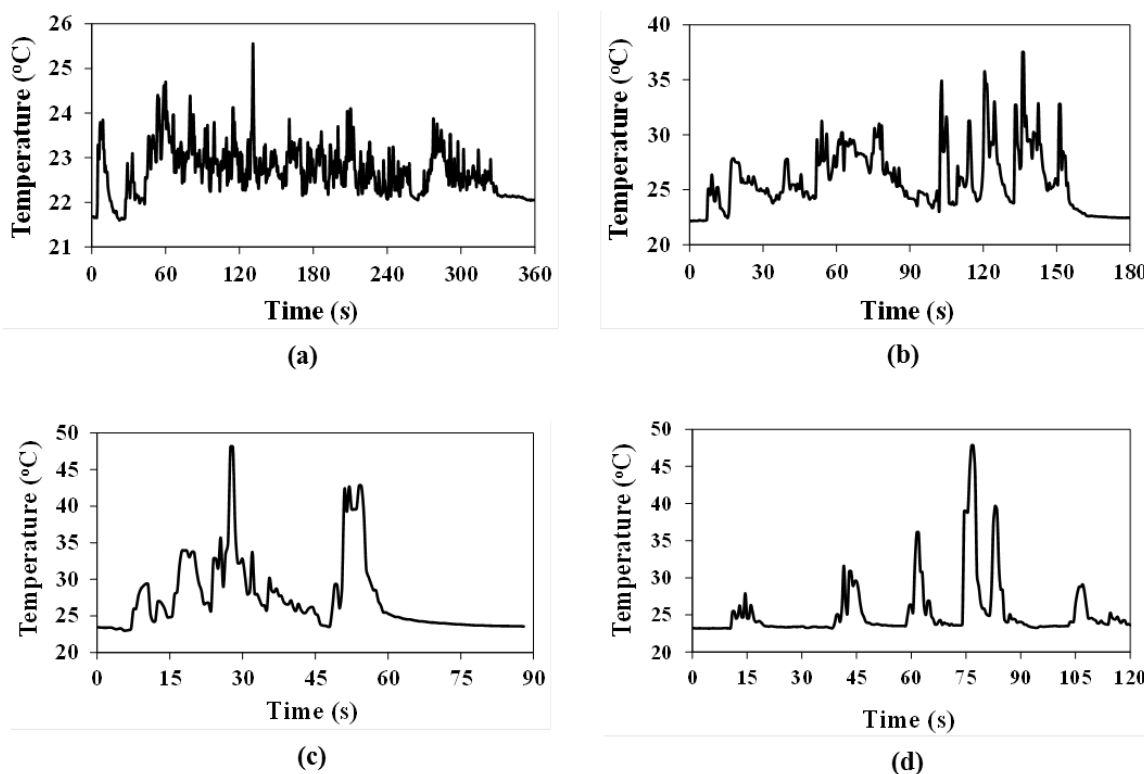


Figure 3.3 Temperature vs. time plots showing worst case (highest peak temperature) for Holmium:YAG and TFL lithotripsy procedures. (a) Holmium laser, $T_p = 25.5$ °C; Laser time = 288 s; Total time = 320 s; (b) TFL at 150 Hz; $T_p = 38$ °C; Laser time = 154 s; Total time = 154 s; (c) TFL at 300 Hz; $T_p = 48$ °C; Laser time = 43 s; Total time = 47 s; (d) TFL at 500 Hz; $T_p = 48$ °C; Laser time = 22 s; Total time = 107 s. Note that the variation in temperatures measured was a function of not only the laser parameters used, but also of the variable movement of the fiber tip and stone sample with respect to the thermocouple position.

The two laser systems produced different saline temperature profiles near the stone sample. During Holmium laser lithotripsy, a gradually increasing, but small overall elevation in the saline temperature was observed, averaging only a few degrees Celsius by the end of the procedure. The highest temperature recorded for any of the stone samples was only about 26 °C (Figure 3.3a). This minimal temperature rise may be explained by the low pulse rate (6 Hz) and low duty cycle (1:167) with sufficient time for saline cooling in between Holmium laser pulses.

On the contrary, during TFL stone ablation there was a rapid and substantial increase in saline temperature, presumably due to the higher duty cycles of 1:10, 1:5, and 1:3 for TFL pulse rates of 150, 300, 500 Hz operation, respectively, and correspondingly lower cooling

times in between laser pulses. The highest temperature measured for any stone sample was 48 °C (Figures 3.3cd). However, such temperatures were maintained for a short time, typically less than 1 s (Figure 3.3d) and less than 4 s total (Figure 3.3c). Such temperatures corresponded to the time when large stone debris or chips were obstructing the sieve, reducing irrigation rates, and temporarily resulting in a thermal buildup in the saline (Figure 3.4). As expected, mean peak saline temperatures decreased as TFL pulse rate was decreased from 500 to 300 Hz, due to lower average power and duty cycle, and longer cooling times in between laser pulses.

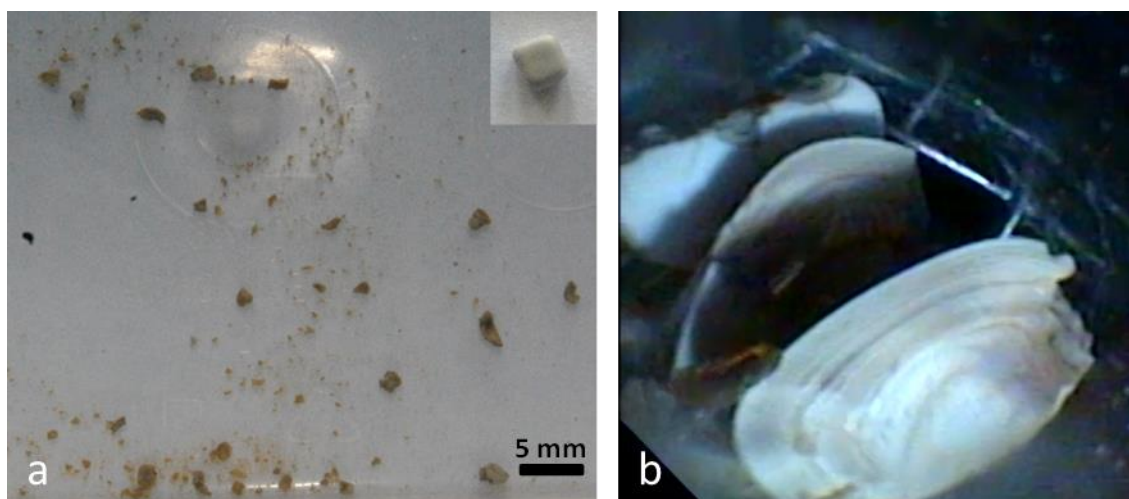


Figure 3.4 (a) Stone fragments after TFL lithotripsy. Inset figure shows the original stone (at the same scale). (b) Video frame showing multiple large stone chips temporarily obstructing the sieve and saline irrigation flow at the time point in which the absolute peak temperature of 48 °C was measured by the micro-thermocouple during TFL lithotripsy at 500 Hz (Figure 3.2b).

It is of interest that TFL operation at 300 Hz lead to a significant decrease in saline irrigation temperatures without decreasing overall operation times, in comparison with 500 Hz. It may be that although TFL operation at 500 Hz results in shorter laser irradiation times, operating time is not reduced due to both greater stone movement and the need to more frequently pause during the procedure and momentarily turn the laser off for improved fiber positioning and visibility.

It should be emphasized that the saline temperatures recorded during TFL lithotripsy may be of potential concern during a clinical procedure, because a prolonged and excessive temperature rise, although not observed here, could possibly cause undesirable collateral thermal damage to surrounding soft urinary tissues such as the ureter or kidney, if left unchecked. However, to put these specific results into proper perspective, it should be noted that even the highest temperatures reached (48 °C) only briefly (< 4 s), are safe, based on standard Arrhenius integral calculations for thermal damage to soft urological tissues using published values [54][55][56] as discussed in more detail below.

3.4 Discussion

During this study, both laser times and total operation times for stone fragmentation were significantly shorter for the experimental TFL operated at all pulse rates (150, 300, and 500 Hz) than for the conventional Holmium laser ($P < 0.05$). This result was due to a number of factors, including TFL operation at higher power density, higher pulse rates, and average powers. The observation of reduced stone retropulsion also played a role, and was due in part to use of lower TFL pulse energies and smaller optical fibers. It should be noted that diode-pumped fiber laser technology such as the TFL is ideally suited to performing laser lithotripsy where low pulse energies, high pulse rates, long pulse durations, and small optical fibers have been previously reported to be optimal for minimal stone retropulsion and more efficient stone ablation [26][38][46][47][48][49][50][51].

Other studies have recently been published exploring the influence of saline irrigation rates on ureter temperature profiles during Ho:YAG laser lithotripsy. For example, Molina et. al. reported higher ureter wall temperatures of 37 °C and 50 °C for a ureteral stone model and an open ureter model, respectively [57], than measured in our study. However, there

were several significant differences between the two studies. For example, the Holmium laser settings (1 J, 10 Hz, Average power = 10 W) in Molina's study were significantly higher than the settings in our study (0.6 J, 6 Hz, Average Power = 3.6 W), and the power density was also higher even after factoring in their larger 365 μm fiber versus our 270 μm fiber. Based on this difference alone, it is not surprising that their ureter temperatures during Holmium laser lithotripsy were higher than in our study. Our Holmium laser settings were carefully chosen only after consultation with urologists about commonly used laser lithotripsy parameters. It should also be noted that Molina, et al., used a saline pump to provide an extremely high constant saline flow rate of 8 ml/sec or 480 ml/min. This flow rate is over 20 times higher than the flow rate in our study (22.7 ml/min) in which we used normal gravitational flow alongside a 270 μm fiber through the ureteroscope working channel. Although saline pumps may provide a useful option for temporarily increasing saline irrigation rates, such an approach can also be dangerous in a clinical setting because it risks washing stone fragments back into the kidney and increases the probability of distending and rupturing the kidney. Finally, Molina, et. al. used a sheep ureter model compared with our artificial ureter model, and their ureter model was not placed in a saline bath, so peak temperatures would be expected to be higher than in our study.

Other studies using an unimpeded flow at greater average powers (20 W, 1 J/20 Hz) saw a temperature rise of 43.4 °C using a low irrigation rate (50 mL/min) [58]. Using a higher irrigation rate of 100 mL/min, minimal to no temperature rise was observed. This contradicts Molina, et. al., but there were no obstructions present in the studies to impede flow and increase temperature. The study does show the importance of saline irrigation during laser lithotripsy to limit temperature increase.

A mathematical description in the form of an Arrhenius integral, is the standard formulation for predicting laser-induced thermal damage to tissues [54]. Thermal damage, quantified by $\Omega(t)$, can be evaluated using the Arrhenius integral:

$$\text{(Equation 3.1)} \quad \Omega(t) = \zeta \int_0^{\tau} \exp\left(-\frac{E_a}{RT(t)}\right) dt,$$

where ζ (s^{-1}) is frequency factor; τ (s) is total heating time; E_a (J/mol) is activation energy; R (8.32 J/K mol) is universal gas constant; and $T(t)$ is absolute tissue temperature. Values of frequency factor (ζ) and activation energy (E_a), corresponding to amount of energy needed to start the transformation process, are derived from experimental analysis. The thermal damage parameter $\Omega(t)$ depends exponentially on temperature and linearly on heating time, and $\Omega(t) = 1$ corresponds to 63% damage to the tissue. It is also useful to define the critical temperature for damage accumulation rate as, $\Delta\Omega/\Delta t$:

$$\text{(Equation 3.2)} \quad \frac{\Delta\Omega}{\Delta t} = \zeta \exp\left(-\frac{E_a}{RT_{crit}}\right),$$

where the critical temperature (T_{crit}) is related to $\Omega(t)$, ζ (s^{-1}), and E_a . Below T_{crit} , or the thermal damage threshold temperature, damage accumulation rate is negligible. However, damage rate increases exponentially when T_{crit} is exceeded.

Unfortunately, there are currently no published Arrhenius integral parameters for ureter tissue. However, studies have been performed using other urinary tissues, such as kidney [55], and other elastic, tubular structures such as arteries [56], which may provide approximations for our case. The critical temperatures for kidney and arteries were reported to be 73.7 °C and 79.15 °C, respectively. The amount of time necessary to damage the ureter can be calculated using these critical temperatures along with their corresponding

values for the frequency factor and activation energies provided in the references [55][56], assuming that $\Omega(t) = 1$, and substituting the absolute peak temperatures observed in our TFL studies of $T = 48\text{ }^{\circ}\text{C}$. The resulting time periods at which the ureter has to be maintained at $48\text{ }^{\circ}\text{C}$, for both kidney and artery approximations, are $t = 18.5$ hours and 424 hours, respectively. Clearly, the peak temperatures achieved in our study are nowhere near thermal damage temperatures for these times scales.

It may be possible to further increase the safety margin and reduce the probability of adverse heating effects during TFL lithotripsy by implementing a combination of safeguards, including (a) higher saline irrigation rates, (b) use of chilled saline, (c) delivery of laser pulses in short bursts of only a few seconds, and/or (d) further reduction in laser pulse rates. For example, syringe pumps are used in the clinic to temporarily provide increased pulsatile saline irrigation rates [59] (e.g. 480 ml/min for Molina study) compared to normal gravitational flow of about 20 ml/min (with 270 μm fiber in working channel) from hanging a saline bag above the patient [60].

Studies observing inadvertent TFL perforation of the ureter, as well as laser-induced thermal damage to ureteroscopic devices (e.g. stone baskets and guidewires) have been conducted for TFL [45]. Incidents of ureter perforation and ureteroscope device damage from the Holmium laser have also been previously reported [61]. It was informative to study how such TFL adverse incidents compare with the Holmium laser as a standard. Several minor technical improvements to the TFL also need to be implemented prior to translation of this technology into the clinic, including integration of a visible aiming beam into the laser system for alignment purposes and reduction of back-reflected light from the optical components.

3.5 Conclusions

The Thulium fiber laser was observed to fragment kidney stones more rapidly than the Holmium laser in a comparative setting, due in part to the combination of the TFL's high pulse rate, high average power, and reduced stone retropulsion. To avoid thermal buildup, TFL lithotripsy should be performed with pulse rates below 500 Hz and/or increased saline irrigation rates. Under these conditions, TFL lithotripsy may provide an alternative to conventional Holmium:YAG laser lithotripsy.

CHAPTER 4: Analysis of Thulium Fiber Laser Induced Bubble Dynamics for Ablation of Kidney Stones

4.1 Introduction

The physical mechanism behind bubble formation during fiber optic delivery of pulsed laser energy in a fluid medium, has been studied extensively over the past several decades for potential laser tissue ablation applications [62]. The majority of these studies have investigated creation of bubbles during delivery of either short pulse (Q-switched) or long pulse (free running) energy from mid-infrared lasers, including Thulium:YAG ($\lambda = 2010$ nm), Holmium:YAG ($\lambda = 2100$ nm), Erbium:YSGG ($\lambda = 2790$ nm), and Erbium:YAG ($\lambda = 2940$ nm) [63][64][65][66][67]. In general, bubbles are formed by laser irradiation in a fluid environment, causing the fluid to evaporate and expand. The resulting bubble expansion leaves a low light absorbing path for the laser beam to traverse between the fiber tip and tissue surface, in effect parting the waters, hence this phenomenon is often referred to as the “Moses Effect”. The rapid expansion and collapse of the bubble provides a mechanical contribution to laser ablation, and a mechanism for unwanted movement of stone debris near the laser irradiation zone, referred to as ‘retropulsion’ [46]. Bubbles thus have direct implications for laser medical applications because the vapor bubble allows non-contact delivery of the laser radiation to the tissue in a highly absorbing fluid environment, provides a mechanical component to the laser ablation mechanism, and causes undesirable retropulsion of stone debris, even at long pulse durations where the ablation mechanism is primarily photothermal.

Ho:YAG laser lithotripsy (or kidney stone ablation) is a successful medical application involving bubble formation during fiber optic delivery of infrared laser energy in a highly

absorbing fluid medium. Bubble formation during Holmium laser lithotripsy has been previously studied in detail [19][68][15][20].

The TFL differs from the Holmium laser in several fundamental ways, which may have a direct effect on bubble characteristics and laser lithotripsy. First, the TFL wavelength of 1908 nm more closely matches a high-temperature water absorption peak in tissue, providing an absorption coefficient of $\sim 155 \text{ cm}^{-1}$, about four times higher than the water absorption coefficient of $\sim 33 \text{ cm}^{-1}$ at the Holmium laser wavelength of 2100 nm [8][9][10][11]. Second, the diode-pumped TFL laser, when electronically modulated to operate in pulsed mode, produces a more uniform square shaped temporal beam profile, as compared to the typical “shark-fin” shaped temporal beam profile produced by the flashlamp-pumped Holmium laser, in which both a macro-pulse structure 100’s microseconds long and a micro-pulse structure of a few microseconds is present (Figure 4.1). Third, TFL energy originates within an 18- μm -core, thulium doped silica fiber, which produces a near single mode spatial beam profile, in turn allowing laser energy to be more easily focused to a small spot and delivered through smaller (e.g. 50, 100, and 150- μm -core) fibers than the multimode beam profile of the Holmium laser, which is limited to use with fiber diameters $\geq 200 \mu\text{m}$ core [42][69][70][71].

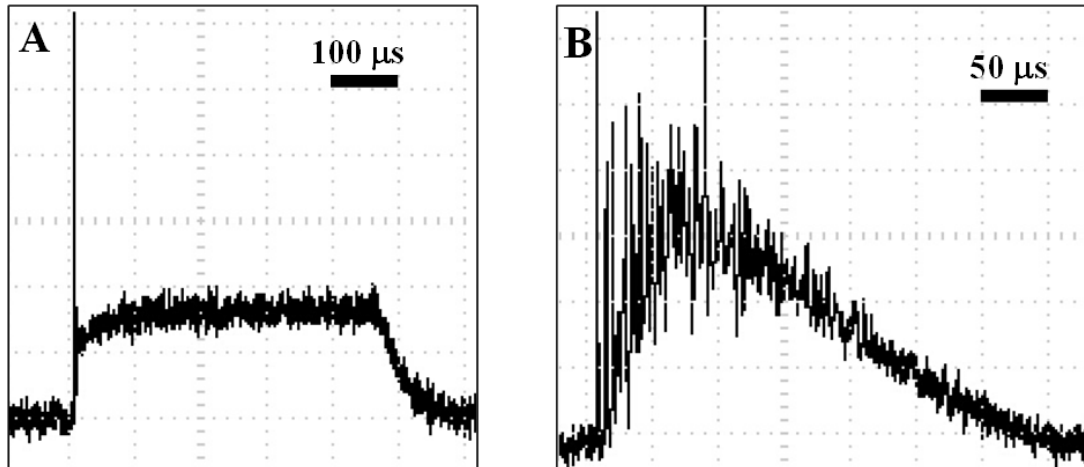


Figure 4.1. Temporal beam profiles produced by Thulium fiber laser (TFL) and Holmium:YAG laser used in this study. (a) The TFL has a 2 μs -long spike at beginning of pulse but overall energy is more uniformly distributed across $\sim 500 \mu\text{s}$ pulse, with the exception of a 100 μs fin shape at the beginning and a $\sim 75 \mu\text{s}$ taper at the end of the pulse. (b) Holmium laser has a large portion of energy delivered at beginning of macro-pulse, then decays after $\sim 75 \mu\text{s}$. Holmium beam profile also contains multiple 1-3 μs micro-pulses in $\sim 350 \mu\text{s}$ macro pulse envelope.

The purpose of this study is to use high speed imaging of TFL induced bubbles and needle hydrophone measurement of bubble pressure transients to determine the influence of these unique TFL parameters on bubble formation and how these bubble characteristics compare to current clinical laser lithotripsy systems such as the Holmium laser.

4.2 Methods

4.2.1 Thulium Fiber Laser Induced Bubble Studies

A 100-Watt, continuous-wave, Thulium fiber laser (TLR 100-1908, IPG Photonics, Oxford, MA) with a center wavelength of 1908 nm was used in these studies. A glass window was used to reflect $\sim 4\%$ of laser output beam into a temporal pulse detector (PD-10, Boston Electronics, MA) in order to synchronize the laser temporal beam profile with recording of the pressure transients and bubble dimensions. Then a 25-mm-focal-length, AR-coated, plano-convex lens was used to focus the 5.5-mm-diameter fiber laser beam from the built-in collimator to a spot diameter of $\sim 25 \mu\text{m}$ ($1/e^2$) for coupling into a separate

105- μm -core (AFS105/125, Thorlabs, Newton, NJ) or 270- μm -core, low-OH, silica optical fiber (RFID Holmium Lightguide, Dornier MedTech, Wessling, Germany). The laser was electronically modulated with a function generator (DS345, Stanford Research Systems, Sunnyvale, CA) to produce variable pulse energies of 5 - 65 mJ, and variable pulse durations of 200 - 1000 μs . A detector (PM100, Coherent, Santa Clara, CA) and power meter (EPM1000, Molectron, Portland, OR) were used to measure average power, and pulse energy was calculated by dividing average power by laser pulse repetition rate.

Figure 4.2 shows a basic diagram of the experimental setup used to capture high speed images of bubbles during TFL studies. The (105- or 270- μm -core) optical fiber was held in place and submerged in a transparent acrylic tank filled with saline. A needle hydrophone (HNC-0400, ONDA, Sunnyvale, CA) with frequency range of 1-10 MHz, and sensitivity of 170 nV/Pa was placed at an angle of 45 degrees, approximately 2 mm from the tip of the fiber to measure the pressure transients of the laser induced bubble. A precision linear stage (460A-XYZ, Newport, Irvine, CA) was used for fiber alignment. The fiber was imaged through the tank using a high-speed camera (Fastcam SA5, Photron, Tokyo, Japan) with magnifying lenses (12x zoom kit, Navitar, Rochester, NY). A high powered lamp was placed behind the tank, to properly illuminate the fiber and produce adequate contrast between the bubbles and surrounding saline. The optical fiber was aligned with the TFL, which was in turn triggered by a function generator (DS345, Stanford Research Systems). The high speed camera, the function generator, and an oscilloscope were triggered sequentially by a digital delay pulse generator (DG535, Stanford Research Systems), to ensure that the entire bubble lifetime was captured with the camera along with needle hydrophone data, for each individual experiment. The high speed camera operated

at 105,000 frames per second ($\Delta t = 9.5 \mu\text{s}$), and with a spatial resolution of $\sim 10 \mu\text{m}$, dependent on the magnification needed to ensure the bubble filled the field of view.

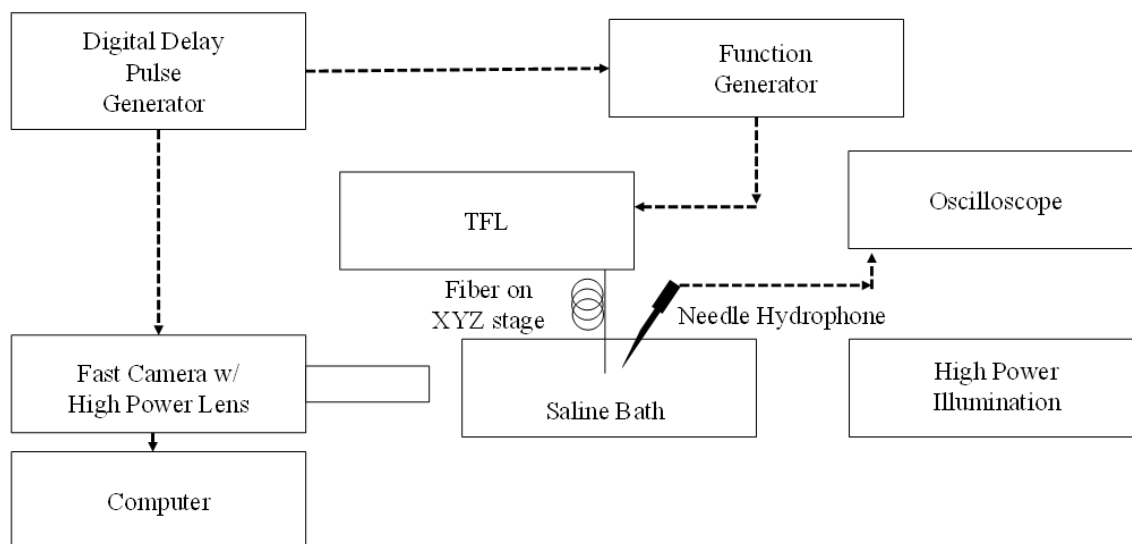


Figure 4.2. Diagram of experimental setup used with Thulium fiber laser for high speed imaging of cavitation bubbles.

For the laser lithotripsy studies, 4-5 mm diameter stone samples composed of 60% calcium oxalate monohydrate (COM) and 40% calcium phosphate (CaP) were used and placed in a small clamp under the fiber. The fiber was positioned in contact with the stone surface using a lab jack (L490, Thorlabs) to manipulate the position of the acrylic tank. The camera setup was kept fixed and any necessary adjustments were instead performed with the stone sample and fiber. Once the fiber and stone were positioned in focus, the triggering method previously mentioned was used to capture footage of the laser induced bubble formation as well as stone ablation.

4.2.2 Holmium:YAG Laser Induced Bubble Studies

A clinical Holmium:YAG laser (TwoPointOne XE, Coherent, Santa Clara, CA) with a center wavelength of 2100 nm was used with a standard, 270- μm -core, clinical, low-OH, silica optical fiber (RFID Holmium Lightguide, Dornier MedTech). The Holmium laser

was operated at variable pulse energies of 200-1000 mJ, fixed pulse duration of 350 μ s, and pulse rate of 10 Hz during the studies. Laser pulse energy was measured using a pyroelectric detector (ED-200, Gentec, Quebec, Canada) connected to an energy/power meter (EPM1000, Molelectron).

A similar experimental setup was used for Holmium as for TFL studies. However, the clinical Holmium laser could not be externally triggered, so the laser was set to 10 Hz and the camera recorded 1 s of video to capture the bubbles. Once video was obtained and an entire bubble lifetime saved, the experiment was repeated at different settings.

4.2.3 Thulium Fiber Laser (1940 nm)

A 500-Watt peak power Thulium fiber laser (TLR-50/500, IPG Photonics, Oxford, MA) with center wavelength of 1940 nm was also used in these studies. Due to advances in TFL technology the peak power was able to be modulated electronically by an internal application from 50-500 W. The pulse durations explored were 200 μ s and 500 μ s. Pulse energy was calculated using peak power and the pulse duration. A temporal profile of the beam was taken to make note of the change in pulse shape as a function of pulse energy (Figure 4.3). A 270- μ m core low OH silica fiber (RFID Holmium Lightguide, Dornier MedTech, Wessling, Germany) was inserted into SMA output coupler of the laser. The 1940 nm TFL was used to show the change in bubble dynamics with a larger range of pulse energy and pulse duration.

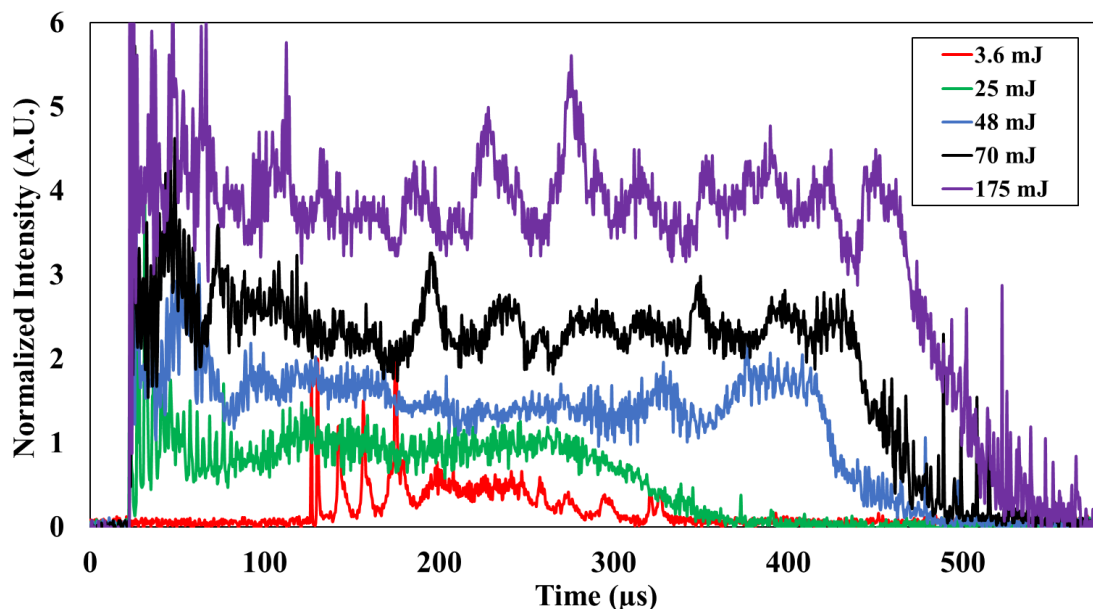


Figure 4.3 Temporal profiles of the 1940 nm laser as a function of pulse energy and time with A.U. being proportional to the intensity of light. The laser is set to a 500 μs pulse duration. The graph shows how the temporal profile of the laser changes depending on the pulse energy setting. Each pulse energy setting is scaled differently to adjust for discrepancies.

The same experimental setup as used with Ho:YAG laser was used for the 1940 nm TFL. Except the TFL was set for 50 Hz pulse rate and the fast camera was externally triggered for 1 s and a single bubble lifetime was saved. Only an $n=1$ sample size was used when analyzing 1940 nm TFL vapor bubbles for comparison with 1908 nm TFL vapor bubbles. Further analysis on 1940 nm TFL vapor bubbles should be done for statistical significance.

4.2.3 Data Analysis

MATLAB (version 2014a, MathWorks, inc., Natick, MA) code was used to analyze bubble dimensions as a function of time. The code identified bubble edges and then created a new picture for both bubble and fiber edges. Using fiber dimensions for calibration, a “microns per pixel” value was determined. The program then found the two outermost lateral points of the bubble at the fiber tip and determined bubble width. A similar method

was used to measure bubble length. The furthest vertical point for the bubble was found, and then using the fiber position, the bubble length was determined. Bubble length was defined as the furthest bubble distance from fiber tip, and bubble width was determined as two furthest bubble distances on either side of fiber tip. A representative image showing labeled bubble dimensions is provided in the inset of Figure 4.4.

A minimum of four experiments were conducted for each set of TFL parameters, and the mean \pm S.D. calculated for each of the bubble dimensions (length and width). A student's T-test was used to determine statistical significance of trends in bubble characteristics. The Holmium laser bubble experiments were only conducted once for each laser setting to confirm data of previously reported studies, and for direct comparison with our TFL data.

4.3 Results

4.3.1 Thulium Fiber Laser

Figure 4.4 displays TFL bubble widths as a function of time for variable pulse energies of 5 - 35 mJ, and for fixed pulse duration of 500 μ s. Initial bubble formation begins earlier in time as pulse energy increases, and then subsequent bubble formations become more chaotic in nature. Tables 4.1 and 4.2 summarize the TFL induced bubble dimensions as a function of pulse energy (mJ), fluence (J/cm^2), and radiant energy density (J/cm^3) for 105 μ m and 270 μ m fibers, respectively. Fluence was estimated using fiber core diameter for initial beam spot size. This value was then multiplied by the high-temperature water absorption coefficient at the TFL wavelength of 1908 nm, to provide radiant energy density. Table 4.1 shows a trend of increasing bubble dimensions (both length and width) as pulse energy increases. The mean TFL bubble length of 1200 ± 90 μ m for the 105 μ m

fiber is consistent with results found in our previous studies, in which undesirable TFL ablation and collateral damage to the ureter and Nitinol stone baskets stalled out at working distances greater than 1.0 mm [45]. Table 4.2 exhibits similar trends as Table 4.1, however, bubble widths are larger for 270 μm fiber than for 105 μm fiber.

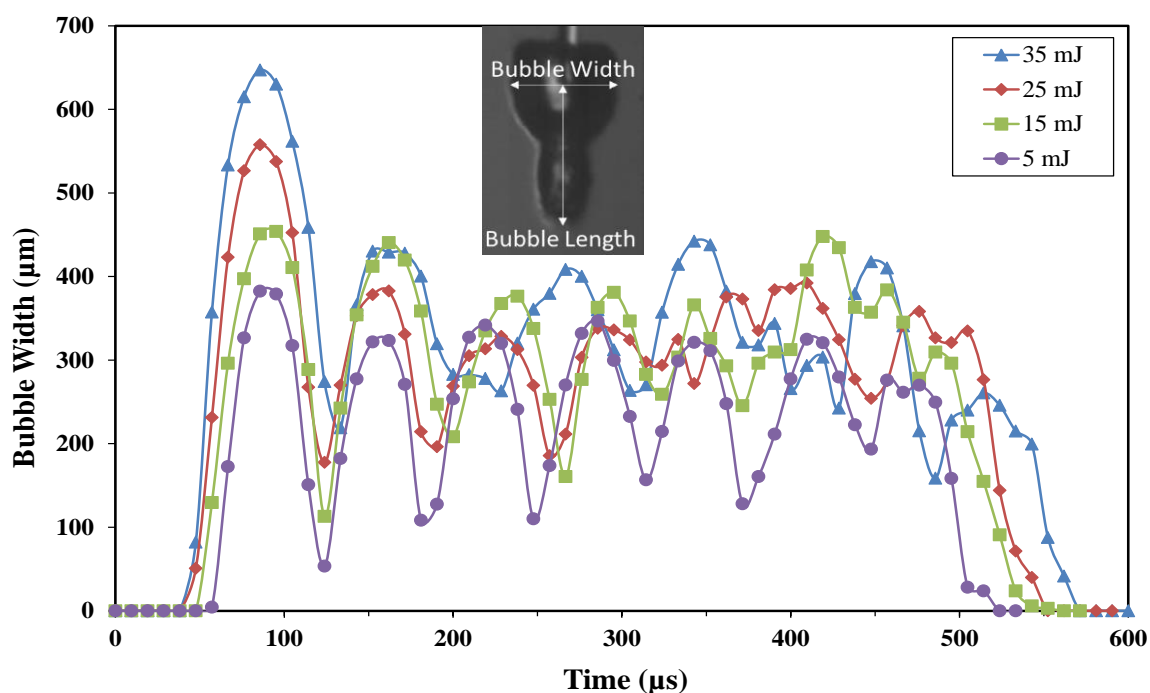


Figure 4.4 Graph of bubble width as a function of TFL pulse energy and time during a single 500 μs pulse using 105 μm fiber. The time necessary to initiate a bubble increases as pulse energy decreases. There is also a clearly defined expansion and collapse for the first bubble due to the spike observed at the beginning of the TFL temporal beam profile shown in Figure 4.1, followed by a more chaotic process for the rest of the laser pulse. The inset image of a bubble shows how width and length of bubble dimensions were measured during data analysis.

Table 4.1. Thulium fiber laser parameters and bubble dimensions using 105- μm -core fiber.

Pulse Energy (mJ)	Fluence ¹ (J/cm ²)	Radiant Energy Density ² (kJ/cm ³)	Bubble Length (μm)	Bubble Width (μm)
5	64	9.9	570 \pm 10	410 \pm 20
15	191	29.6	815 \pm 60	510 \pm 20
25	318	49.3	920 \pm 130	580 \pm 25
35	446	69.1	1200 \pm 90	650 \pm 20

¹ 100- μm -core fiber was used to calculate Fluence. Mean \pm S.D. bubble dimensions was calculated from n=4 fibers.

² A high temperature water absorption coefficient of 155 cm⁻¹ at 1908 nm was used to calculate radiant energy density [39].

Table 4.2. Thulium fiber laser parameters and bubble dimensions using 270- μm -core fiber.

Pulse Energy (mJ)	Fluence ¹ (J/cm ²)	Radiant Energy Density ² (kJ/cm ³)	Bubble Length (μm)	Bubble Width (μm)
5	9	1.4	500 \pm 20	430 \pm 10
15	26	4.0	740 \pm 90	630 \pm 10
25	44	6.9	850 \pm 30	740 \pm 10
35	61	9.5	1070 \pm 50	870 \pm 40

¹ 270- μm -core fiber was used to calculate Fluence. Mean \pm S.D. bubble dimensions was calculated from n=4 fibers.

² A high temperature water absorption coefficient of 155 cm⁻¹ at 1908 nm was used to calculate radiant energy density [39].

Figure 4.5A shows TFL temporal beam profile, needle hydrophone pressure transient data, and bubble widths, synchronized as a function of time. Figure 4.5B zooms in on a spike in the pressure corresponding with the initial 2- μs -long set of spikes in TFL temporal beam profile in Figure 4.5A. The needle hydrophone and bubble width data shows the onset of the first bubble directly after the initial spikes in the temporal beam profile. These spikes therefore appear to initiate the first cavitation bubble. This conclusion is substantiated by the difference in shape of first bubble when compared to rest of laser pulse. Maximum pressure was approximately 0.6 bars, during initial collapse of vapor bubble, for 35 mJ pulse energy and 500 μs pulse duration settings.

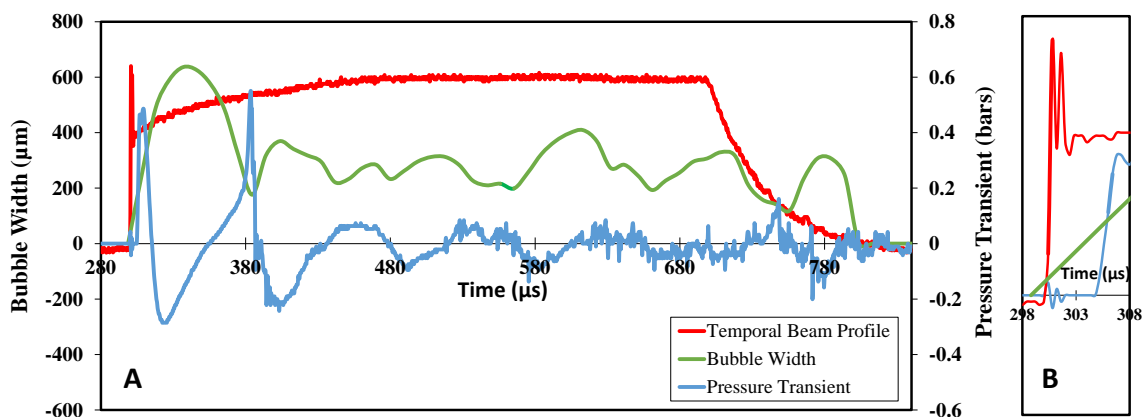


Figure 4.5 The laser temporal beam profile (red) from Figure 4.5A is superimposed with the bubble width (green), and needle hydrophone pressure data (blue), as a function of time. The synchronized data shows how bubble width influences the pressure transients, while confirming that multiple bubble collapses occur during a single laser pulse. Figure 4.5B shows a small pressure transient occurring during the initial 2- μ s-long set of spikes in the TFL temporal beam profile. The spikes are believed to be the cause of the onset of the first bubble. Note that although it appears that the bubble is expanding before the pulse, this is an artifact from the oscilloscope sampling the pressure transient and beam profile data at a smaller temporal resolution (0.4 μ s) than for the camera (9.5 μ s).

Images of the first maximum bubble expansion for each laser setting are provided in Figure 4.6, as a function of both pulse energy (5 - 65 mJ) and pulse duration (200 - 1000 μ s), for the large array of TFL parameters studied. As an example, the final column of images on the right shows a clear trend in which bubble volume increases with pulse energy, for a fixed pulse duration (1000 μ s). Alternatively, the first row of images with a fixed pulse energy (5 mJ), shows a trend of bubble volume decreasing and changing shape as pulse duration increases.

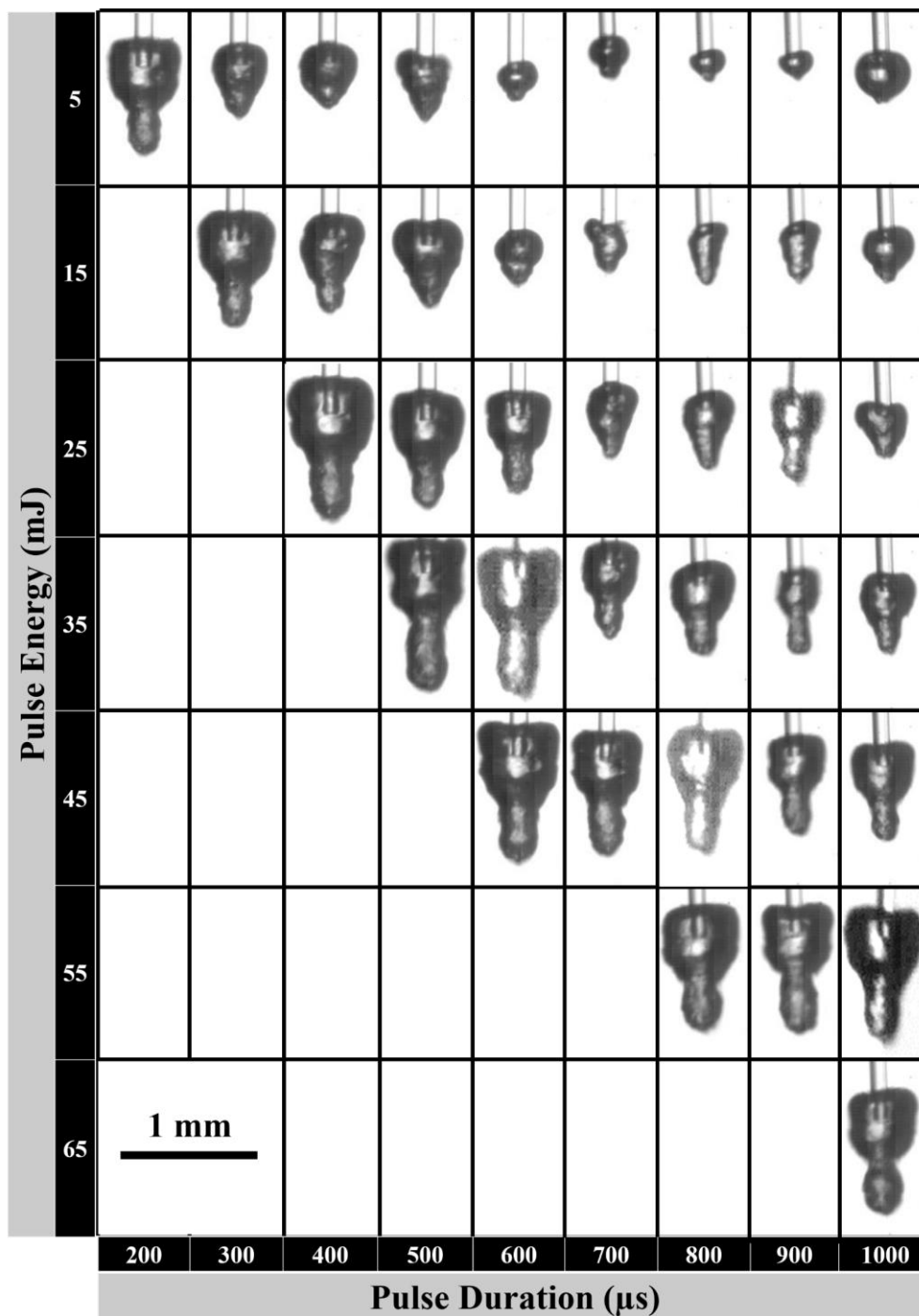


Figure 4.6. Maximum bubble size and shape as a function of both TFL pulse energy and pulse duration for 105 μm fiber. As the pulse energy increases, for a given fixed pulse duration, there is an increase in bubble dimensions. For a fixed pulse energy and increase in the pulse duration, there is a decrease observed in bubble dimensions.

The most interesting and noticeable differences between TFL and Holmium induced bubble characteristics (described further below) were the size and number of bubbles

created. TFL produced smaller bubble widths and lengths, and a stream of bubbles during a single laser pulse (Figure 4.7). The bubble stream was characterized by a multiple bubble stream, each locally expanding and collapsing axially out of phase with the other bubbles. This phenomenon has been observed in other bubble dynamics studies using Holmium laser as well, but only with low pulse energy and long pulse duration [19]. It should be noted that there is a noticeable difference in the bubble shape between the initial bubble and subsequent bubbles.

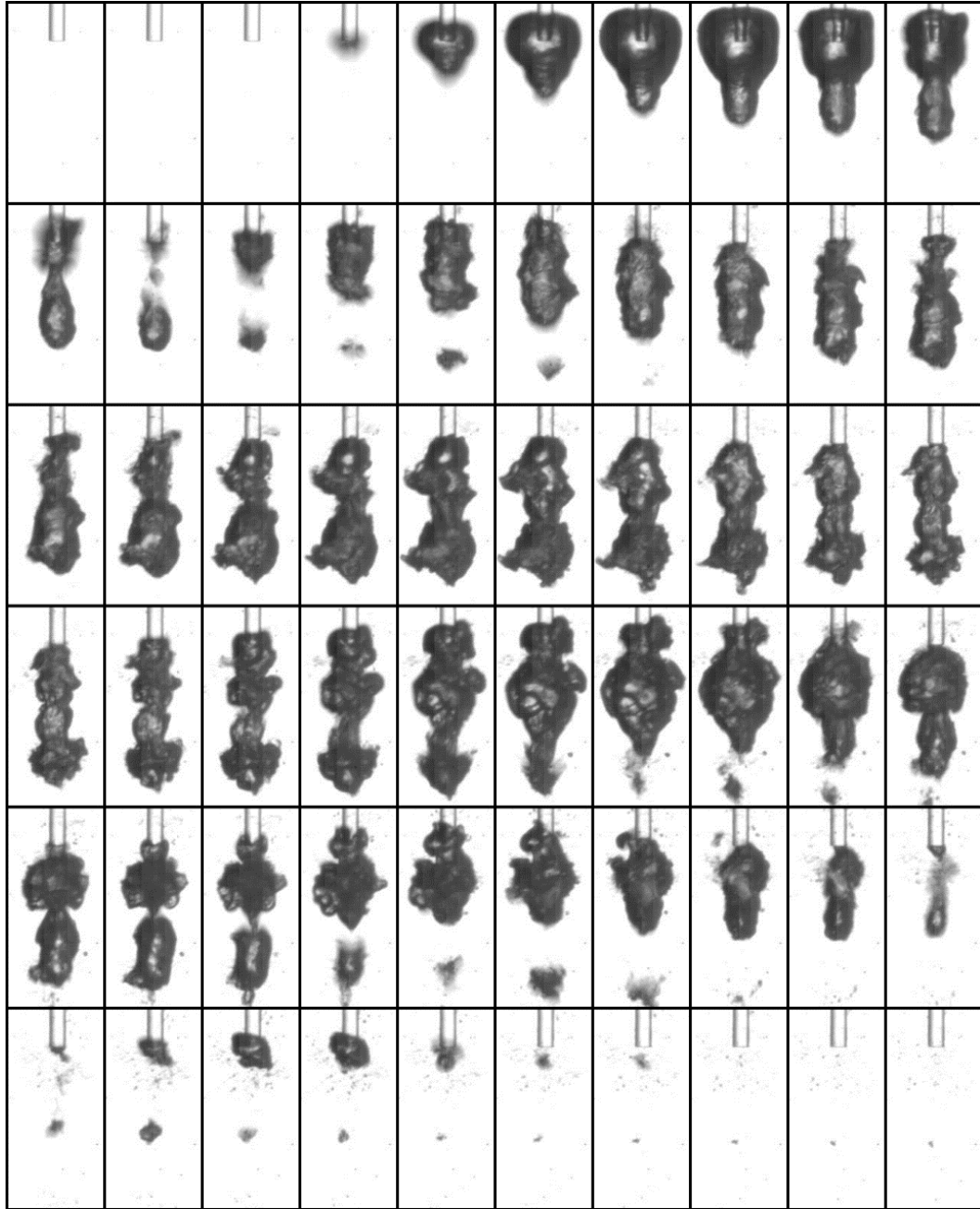


Figure 4.7 Frames taken with a high-speed camera at successive $9.5 \mu\text{s}$ intervals, showing formation of a bubble stream during a single TFL pulse delivered through a $105 \mu\text{m}$ fiber at 35 mJ and $500 \mu\text{s}$. The sequence shows multiple bubble expansions and collapses along the bubble stream. The chaotic nature after the initial bubble is also observed in these frames.

Qualitative data was also acquired with TFL fiber in contact with a kidney stone. The field of view was limited due to both the presence of stone sample and loss of visibility as stone debris obscured the field during laser ablation. Figure 4.8 shows fiber-to-stone working distance for 0 mm (contact), 0.5 mm, and 1 mm from the stone surface, before,

during, and after laser irradiation. When comparing post-ablation images for both contact and 1 mm working distances, the amount of stone debris decreases as working distance is increased. This is expected because energy needed to evaporate the saline increases as fiber working distance is increased, and hence the effective laser fluence at stone surface decreases. For a 1 mm working distance, the majority of energy is absorbed by saline during bubble formation.

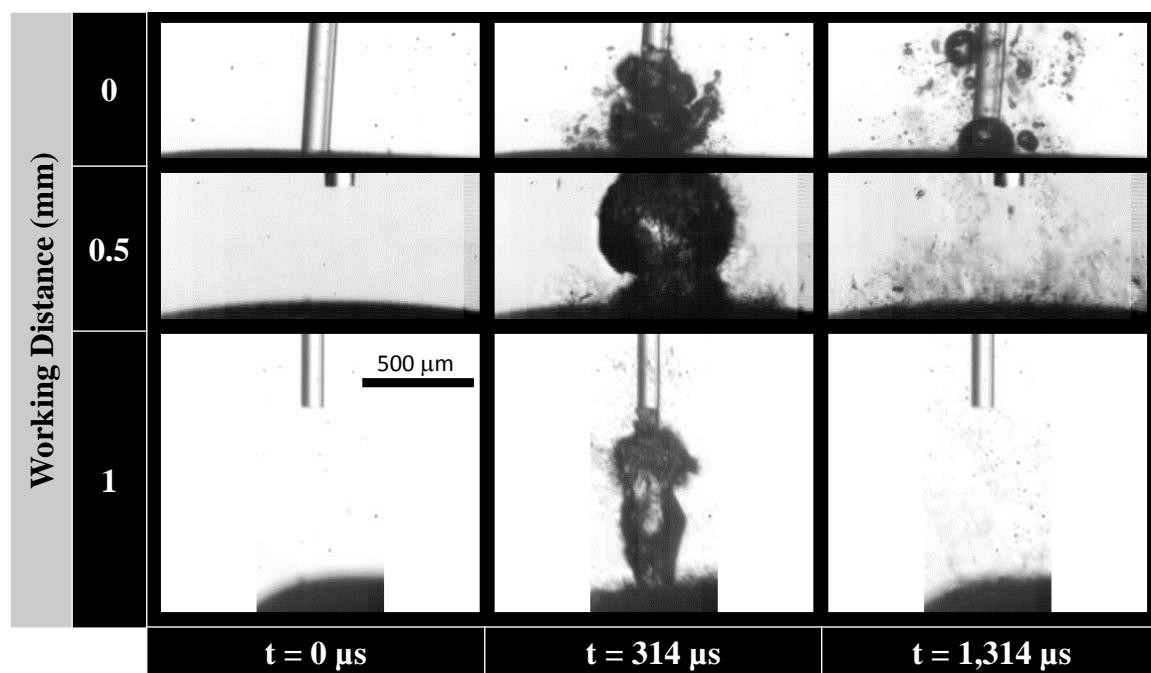


Figure 4.8. Laser induced vapor bubble and stone debris and as a function of fiber-to-stone working distance and time for TFL laser settings of 35 mJ pulse energy, 500 μs pulse duration, and 105- μm -core fiber. There is a larger amount of debris produced by a fiber in contact mode (0 mm) compared to a noncontact working distance of 1 mm away, at which laser stone ablation stallout occurs. Note that the third row of images (1 mm working distance) were acquired at a different aspect ratio (128 x 344) than the other rows of images (320 x 184).

4.3.2 Holmium Laser

Figure 4.9 displays Holmium laser bubble dimensions as a function of variable pulse energies (200 - 1000 mJ) and fixed pulse duration (350 μs). Bubble volume increased as pulse energy increased, as expected. Although the same “pear” bubble shape was observed for both lasers, maximum Holmium bubble dimensions (length and width) were four times

larger than for TFL using a similar 270 μm fiber, for the range of laser parameters studied (Tables 4.2 and 4.3). The larger Holmium laser induced bubble dimensions are most likely due to the greater peak power used. For example, a Holmium laser typically operating at 600 mJ pulse energy and 350 μs pulse duration during a clinical laser lithotripsy procedure generates a peak power of 1700 W, as compared to only 70 W from TFL operating at 35 mJ and 500 μs . The rate at which the saline is heated to produce a phase change from liquid to vapor is highly dependent on the rate of energy deposition into the medium, which is in turn dependent on absorption coefficient and peak power. Needle hydrophone data was also taken to compare with the TFL data acquired. The maximum pressure measured for 600 mJ pulse energy setting was approximately 7.5 bars during first collapse of vapor bubble.

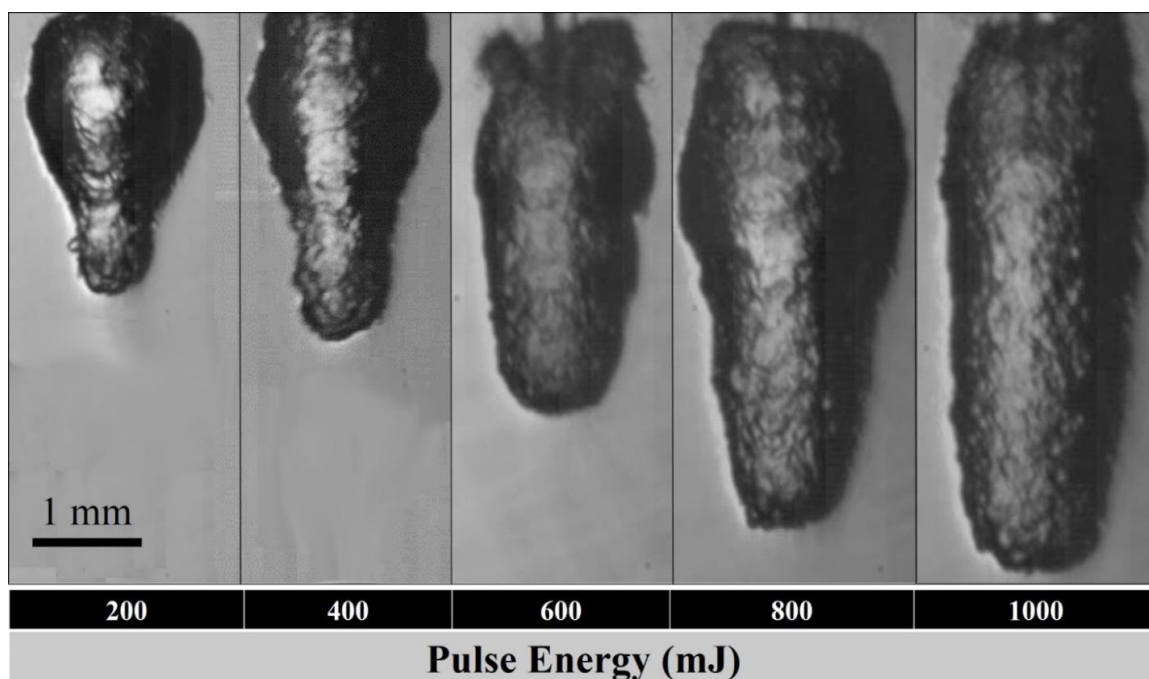


Figure 4.9. Maximum bubble size and shape as function of Holmium laser pulse energy for a fixed pulse duration of 350 μs , using a 270 μm fiber. Bubble dimensions increase as pulse energy increases, as expected.

Table 4.3. Holmium:YAG laser parameters and bubble dimensions using 270- μm -core fiber.

Pulse Energy (mJ)	Fluence ¹ (J/cm ²)	Radiant Energy Density ² (kJ/cm ³)	Bubble Length (μm)	Bubble Width (μm)
200	336.7	10.1	2100	1910
400	673.4	20.2	2790	2200
600	1010.1	30.3	3270	1980
800	1346.8	40.4	3710	2650
1000	1683.5	50.5	4910	2660

¹A 270- μm -core fiber was used to calculate fluence.

²A high temperature water absorption coefficient of 33 cm⁻¹ at 2120 nm was used to calculate radiant energy density [39].

The typical Ho:YAG vapor bubble is characterized by a single expansion and collapse of the bubble, the collapse causes a large pressure transient. Figure 4.10 shows a succession of frames from a 1000 mJ / 350 μs Ho:YAG laser pulse. This dynamic differs from the TFL vapor bubble in that the TFL vapor bubble does not produce large pressures from the last collapse, due to multiple collapses during the laser pulse and is the main reason for a reduction of repulsion from the TFL. Figure 4.11 shows a representative pressure transient for the Ho:YAG laser.

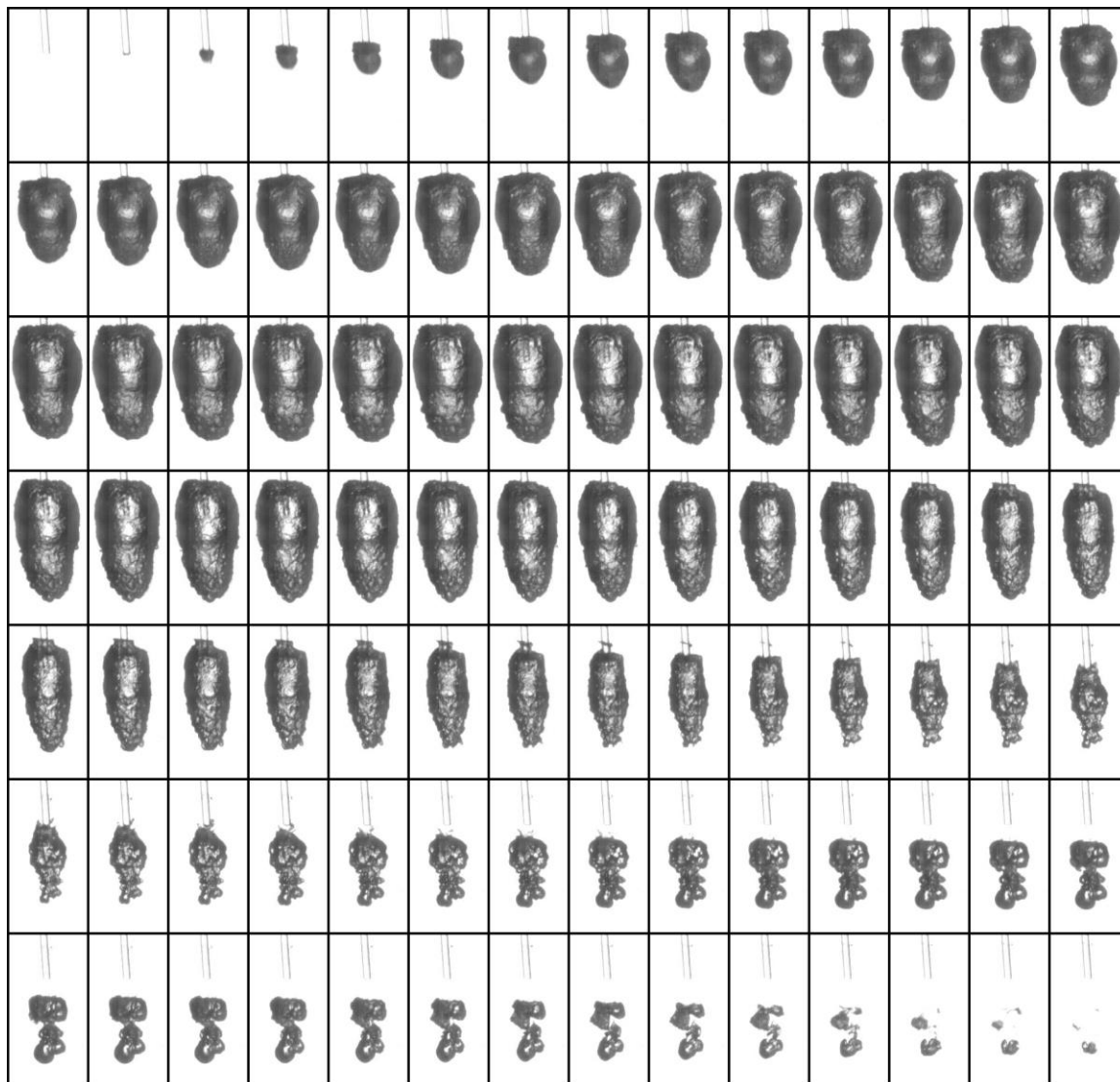


Figure 4.10. Ho:YAG vapor bubble frames with $9.5 \mu\text{s}$ intervals for a 1000 mJ , $350 \mu\text{s}$ laser pulse, showing an initial expansion to a single collapse, that rebounds at the end of the laser pulse.

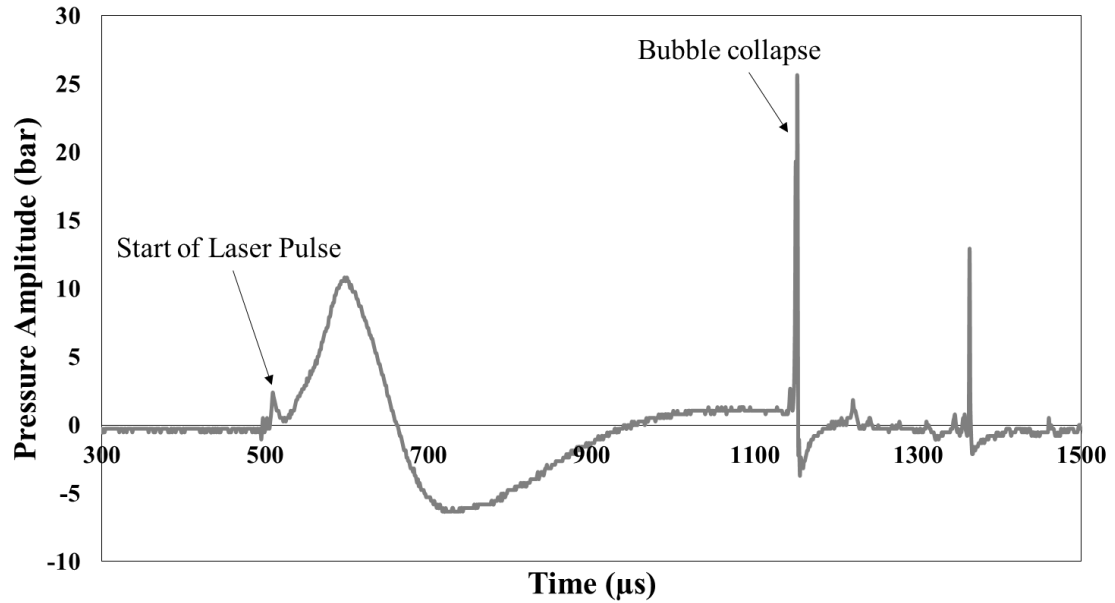


Figure 4.11. Representative Holmium:YAG vapor bubble pressure transient with pulse energy of 800 mJ, and pulse duration of 350 μs .

A more complete study of Holmium laser induced bubbles was not performed due to the already extensive literature available [19][65][66][67][72][73][74][75].

4.3.3 Thulium Fiber laser (1940 nm)

The stream of bubbles is still observed in the dynamics of the 1940 nm TFL vapor bubble when operating at the same 35 mJ 500 μs laser parameters. However, there is a change in the number of oscillations as the peak power is increased. Figure 4.12 shows bubble width as a function of time for several different peak power settings (350 W, 140 W, 70 W).

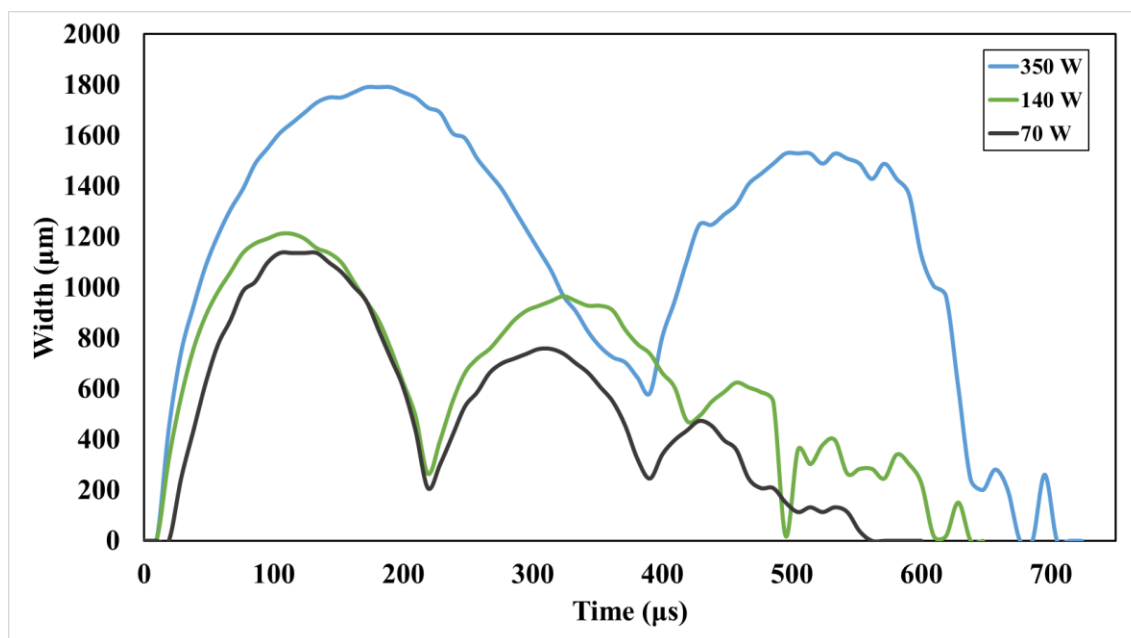


Figure 4.12. Bubble width as a function of time for different peak powers of the TFL emitting a 1940 nm wavelength. The number of bubble expansions and collapses increase as the peak power decreases.

4.4 Discussion

The stream of multiple bubbles produced from a single TFL pulse is perhaps the most interesting difference between current observations and previous reports. Since radiant energy density (J/cm^3) produced by each laser was similar at the fiber tip (Tables 4.1 and 4.3), the TFL bubble stream may be due in part to the TFL temporal beam profile. However, the TFL bubble stream is most likely caused by the differing peak power between the TFL and Ho:YAG laser. The mechanical force produced by bubble collapse has been previously reported to decrease as multiple bubbles are produced, for a Holmium laser operating with 200 mJ at 1100 μs [19]. This was interpreted to mean that bubble collapse is dampened if the laser pulse continues to emit energy during the collapse phase. In that specific study, bubbles were generated ~ 90 degrees out of phase, so mechanical force waves were destructively interfering, and a smaller net force was measured. The study

also concluded that bubble dimensions reached a quasi-steady state for pulses longer than 460 μs , applicable to our study [19].

The authors have attributed the differing bubble dynamics between the TFL and Ho:YAG to be caused by the lasers operating at differing peak powers. As mentioned previously, typical Ho:YAG laser settings are in the 1000's of Watts peak power, while TFL operates in the 10's of Watts peak power. With the advent of the 1940 nm laser being able to operate in 100's of Watts peak power, it would be expected that the pressure transient produced from a larger peak power TFL would exhibit similar bubble dynamics as the Ho:YAG. This means that the pressure spike caused by the collapse of the bubble would become apparent. Preliminary studies of the pressure transients produced from a high peak power pulse of the TFL emitting 1940 nm wavelength have been conducted. While there is pressure produced from the collapse of the bubble the results are inconclusive.

The absolute maximum pressures measured were 7.5 and 0.6 bars, for Ho:YAG and TFL respectively. Higher Holmium pulse energies (800 mJ) produced pressures up to 26 bars. Kidney stone retropulsion will increase as maximum pressures increase. The observation that TFL produces pressures about an order of magnitude lower than Ho:YAG confirms previous empirical studies which have concluded that TFL stone ablation efficiency increases due to a decrease in stone retropulsion [76].

For thermal confinement to be satisfied, the laser pulse duration must be shorter than the thermal relaxation time, given by $\tau_{diffusion} = \frac{\delta^2}{\kappa}$, where δ is optical penetration depth (cm) and κ is thermal diffusivity (cm^2/s) in water for our study. Thermal confinement is

achieved for both TFL ($\tau_{diffusion} = 32.5 \text{ ms}$) and Holmium laser ($\tau_{diffusion} = 185 \text{ ms}$) used in this study, so thermal diffusion during the laser pulse does not appear to be a factor.

Figure 4.4 shows that as pulse energy decreases, time from laser initiation to bubble initiation increases. This was most likely due to the energy (or fluence) necessary to create a bubble [73]. The dependence of bubble formation on rate of energy deposition has been previously described [62] and provides insight into the empirical relationship found in Figure 4.4. A similar effect of increased bubble onset times has been reported for constant pulse energy when pulse duration is increased [19]. The threshold fluence required to induce a bubble, based on superheating of water, has also been reported [73]. These calculations lead to the interpretation that faster energy deposition into water also leads to faster bubble formation. The same bubble formation delay as a function of fluence (or pulse energy in our study) was also reported [73].

Tables 4.1 and 4.3 showed that the amount of energy absorbed by saline (radiant energy density) was of the same order of magnitude for TFL at 35 mJ versus Holmium at 1000 mJ, the absolute value was slightly larger for TFL. The rest of the data showed that the Holmium laser induced bubble had a 4x larger volume and generated different bubble dynamics compared to TFL. The larger Holmium bubble dimensions and multiple bubbles are not just due to larger fiber diameter. For example, Tables 4.1 and 4.2 show that when TFL is operated with a 105- or 270- μm fiber, there is a slightly larger width for the larger fiber ($P < 0.05$) in Table 4.2, however, the lengths are similar ($P > 0.05$). Multiple bubbles were also observed during TFL operation with 270 μm fiber. The larger bubble dimensions and differing bubble dynamics are therefore primarily a byproduct of the larger peak power produced by Holmium laser and not significantly influenced by larger fiber diameter. This

is interesting given that previous research groups have reported an increase in bubble dimensions as fiber diameter increases [74].

Figure 4.5 displays synchronized data of the temporal beam profile, bubble width, and pressure transient data from a needle hydrophone. The needle hydrophone data corresponds well with the bubble width data in Figure 4.5A. The figure also shows that the first bubble collapse is responsible for maximum pressure produced by bubble. This is consistent with previously reported pressure transient data for laser induced bubbles. However, completion of the bubble does not produce a large pressure transient. This is most likely due to bubble collapsing asymmetrically along axial direction, causing resulting pressure waves to mostly destructively interfere. Figure 4.5A also confirms the qualitative observation of an initial bubble collapse followed by a chaotic bubble chain of locally collapsing bubbles in axial direction. Figure 4.5B shows that the initial series of spikes in the laser temporal beam profile causes formation of the initial bubble. It should be noted that although it appears as if the bubble begins to expand slightly before the laser pulse begins, this is an artifact due to the difference in sampling rates between the oscilloscope (0.4 μ s) and high-speed camera (9.5 μ s) camera used in our study.

Variations in TFL bubble dimensions as a function of both pulse duration and pulse energy is also shown in Figure 4.6. As pulse energy increased, more energy was absorbed by the saline and converted into generating a bubble with ever greater volume. As pulse duration increased, the same amount of energy was deposited over a longer time period. Correspondingly, the peak power decreased with longer pulse duration, causing bubble formation closer to the fiber tip. While this was not observed for every laser setting, when the entire range of laser settings were examined, the trend became clear. The bubble has

been reported to be more “pear” shaped for longer pulse durations and more “spherical” at short pulse durations [19].

When the fiber was in contact with the stone, only one bubble expanded and contracted away from the surface, different than when there was no sample in front of the fiber. Multiple bubble collapses re-appeared when the fiber was only 250 μm from stone surface. A plausible explanation for the presence of only a single bubble is due to unequal pressure surrounding the bubble. No pressure was exerted by saline on the bubble from the bottom due to the stone surface, and once the stone was ablated, it was displaced with expanding gas. The bubble expansion only had to counteract pressure acting from an angle of 180 degrees instead of 360 degrees. This explanation is also consistent with observations that TFL provides improved ablation in contact mode [45]. When the fiber was a short distance away from the stone surface, a portion of the energy was used for creating multiple bubbles between the fiber and stone surface.

TFL ablation stallout at a fiber-to-sample working distance of about 1 mm was previously reported [77] and is qualitatively observed in Figure 4.8, showing a fiber at working distances of 0, 0.5, and 1 mm away from a kidney stone. The final images show substantially more debris after the TFL pulse delivered in contact mode than at 1 mm. These observations are directly applicable to the clinic, because they not only determine the maximum working distance for efficient laser lithotripsy before ablation stalls out, but they also factor into the safety of the procedure as well. For example, this short TFL working distance may provide a greater safety margin from accidental perforation of the ureter or destruction of nitinol stone basket device during laser irradiation, as compared to 4-5 mm maximum working distance previously reported for Holmium laser [45].

4.5 Conclusions

TFL parameters differ in several fundamental ways from Holmium laser, including smaller fiber delivery, more strongly absorbed wavelength, low pulse energy/high pulse rate operation, and more uniform temporal pulse structure. High speed imaging of laser induced bubbles and needle hydrophone measurement of pressure transients were performed to determine influence of these laser parameters on bubble formation. TFL bubble dynamics were unique in that a stream of multiple bubbles was produced during a single laser pulse. TFL bubble dimensions were also four times smaller than for Holmium laser due to lower peak power and smaller fiber diameter. These observations are consistent with previous non-contact TFL ablation studies reporting stallout at working distances beyond 1.0 mm, as compared with non-contact Holmium laser ablation at distances up to 5 mm. The pressure transients for Holmium and TFL measured 7.5 bars and 0.6 bars, respectively, confirming previous empirical evidence that TFL produces less stone retropulsion.

CHAPTER 5: Investigation of the Thulium Fiber Laser Ablation Mechanism for Real and Artificial Kidney Stones in Air and Water Mediums using Scanning Electron Microscopy

5.1 Introduction

Previous studies have determined Ho:YAG laser lithotripsy to be primarily a photothermal ablation mechanism from direct absorption by the stone material [15]. Both the Ho:YAG and TFL operate at similar pulse durations (100's μ s), and pulse energies (10's to 1000's mJ). The similar laser parameters has led previous researchers citing Ho:YAG ablation mechanism (photothermal) the same as TFL [78]. However, no Scanning Electron Microscope (SEM) images or evidence of primary ablation mechanism for TFL lithotripsy has been documented. The purpose of this study is to consider preliminary findings for the primary ablation mechanism of TFL lithotripsy.

5.2 Theory

5.2.1 Photothermal Ablation Mechanism

Direct absorption of near-IR radiation leads to non-radiative decay, heat generation, and a consequent rise in temperature that is responsible for chemical decomposition, melting, and ablation. This process typically occurs at long laser pulse durations ($> 1 \mu$ s), and low irradiances ($\ll 100 \text{ MW/cm}^2$) [20]. To date, laser lithotripsy has been considered to be predominantly a photothermal ablation mechanism [15]. Temperature change due to irradiation is a function of the absorption coefficient and specific heat of a material [20]. Temperature rise chemically decomposes and melts stones depending on thermal properties. However, optical absorption coefficients of different dry stone compositions have been reported to be similar at near-IR wavelengths, inconsistent with widely varying

ablation thresholds and ablation rates, leading to the hypothesis that other mechanisms may contribute to stone ablation [16]. A list of thermal breakdown temperatures, Hounsfield unit densities, and ablation thresholds for different kidney stone compositions was compiled from multiple sources (Table 1) [16][77][79][80]. Thermal breakdown temperature is defined as chemical decomposition of a material due to heat. Hounsfield unit is defined as a linear transformation of the original linear attenuation coefficient of a material into a new scale in which radiodensity of water is defined as 0 HU and air as -1000 HU. In short, the Hounsfield unit describes radiodensity of a material. Differences in kidney stone breakdown temperatures are most likely due to differences in thermal properties and density.

Table 5.1. Thermal and mechanical properties of different kidney stone compositions, compiled from multiple sources [16][77][79][80].

Stone Composition	Breakdown Temperature (°C)	Hounsfield Unit Density (HU/mm)	TFL Ablation Threshold (J/cm ²)
MAP	100	53 ± 38	NA
COM	206	105 ± 43	20.8
Cystine	264	45 ± 4	NA
UA	360	50 ± 24	6.5

MAP = Magnesium Ammonium Phosphate; COM = Calcium Oxalate Monohydrate; UA = Uric Acid

5.2.2 Micro-explosion Ablation Mechanism

Kidney stones are typically immersed in a fluid environment composed of urine accompanied by constant saline irrigation during laser lithotripsy, where water serves as the dominant optical absorber of IR laser energy. Although laser lithotripsy is primarily a photothermal ablation mechanism, there are secondary mechanical ablation effects, due to water absorption [19][81]. Laser irradiation causes water trapped in pores inside hard calculi to vaporize, creating high pressure in a localized region [20]. Even in the absence of vaporization, large differences in the thermal expansion coefficient between stone material ($10\text{-}70 \times 10^{-6} / ^\circ\text{C}$) and water ($207 \times 10^{-6} / ^\circ\text{C}$) may lead to a significant rise in

pressure inside the stone [82]. The abrupt pressure change from the vapor produces a mechanical stress wave within the stone, which may be sufficient for ablation. However, even if the stress wave is not alone sufficient for ablation, it facilitates removal of weakened material from the irradiation site [15]. Recent high power TFL studies have reported an increase in ablation volume due to an increase in water content, as well as a change in ablation as a function of pore size of bladder stones [29].

5.2.3 Ablation Mechanism Studies with Other Hard Tissues

Previous studies have reported on how the primary chromophore determines the laser ablation mechanism for dental enamel by comparing different wavelengths with high water absorption versus high mineral absorption [83]. High absorption in enamel resulted in the ablated surface appearing smooth and melted, due to thermal damage. However, high water absorption produced significant mechanical damage at the surface, resembling fragmentation. In a similar manner, this study describes the use of scanning electron microscopy (SEM) to examine TFL kidney stone ablation mechanisms, specifically the dependence of the primary absorber on laser energy.

5.3 Methods

5.3.1 Thulium Fiber Lasers ($\lambda = 1908$ and 1940 nm)

This study utilized two Thulium fiber lasers (TFL). The first TFL was a 100 W, continuous-wave (CW) laser (TLR 100-1908, IPG Photonics, Oxford, MA) with 1908 nm wavelength, electronically modulated using a function generator (DS345, Stanford Research Systems, Sunnyvale, CA) to produce 500- μ s pulses for lithotripsy studies, similar to Ho:YAG laser pulse lengths of 350-700 μ s. The TFL produced a Gaussian mode beam profile, originating from an 18- μ m-core thulium-doped silica fiber, with a built-in

collimator providing a 5.5-mm-diameter output beam. A 25-mm-focal-length lens was used to focus the collimated TFL beam down to a $1/e^2$ spot diameter of $\sim 25 \mu\text{m}$, for coupling into a 200- μm -core, low-OH, silica optical fiber (FP200ERT, Thorlabs, Newton, NJ), for use in stone ablation studies. All experiments were performed with a TFL output energy per pulse of 35 mJ, pulse duration of 500 μs , pulse rate of 300 Hz, average power of 10.5 W and irradiation time of 10 s, similar to previously published studies, for comparison [44]. The lower pulse energy setting was representative of a ‘dusting’ operation mode during laser lithotripsy.

The second TFL (TLR-50/500, IPG Medical, Marlborough, MA) with 1940 nm wavelength, was operated in pulsed mode, and capable of 500 W peak power and 50 W average power output. Peak power, pulse rate, and pulse duration were modulated electronically by internal software. A 270- μm -core, silica fiber (RFID Holmium Lightguide, Dornier MedTech, Germany) with SMA connector was attached to the laser. All experiments were performed with output energy per pulse of 200 mJ, pulse duration of 500 μs , pulse rate of 53 Hz, average power of 10.5 W, and irradiation time of 10 s. The higher energy output of this TFL enabled operation in a ‘fragmentation’ mode for laser lithotripsy.

5.3.2 Kidney Stone Samples

Calcium oxalate and uric acid stones comprise over 90% of all stones encountered in the clinic [8]. Uric acid (UA), and calcium oxalate monohydrate (COM) stones were obtained from a stone analysis laboratory (Labcorp, Oklahoma City, OK). All samples were desiccated in an oven for 30 min. before irradiation. The stones were placed in glassware and held with a mechanical clamp, with or without water, and irradiated with a

hand held optical fiber for a total time of 10 s. During experiments utilizing water, each sample was fully submerged ~ 1 min before beginning the test. Artificial UltraCal30 (Capital Ceramics, West Valley City, UT) and BegoStone plus (Bego, Bremen, Germany) stones were used to determine their feasibility as stone phantoms. The UltraCal30 and BegoStone plus powder/water mixture was kept at a fixed weight ratio of 100:38, and 100:20, respectively, consistent with the previous literature [84].

5.3.3 Scanning Electron Microscopy (SEM)

Kidney stone samples were sputter coated with a 30 nm gold layer prior to SEM (JSM-6460 LV, Jeol, Peabody, MA) to analyze natural particle size and laser ablation effects on the stone surface. The SEM had a maximum resolution of 10 nm, magnification of $5\times$ to $300,000\times$, and accelerating voltage of 0 to 30 kV. Images of stones were taken at 10 and 20 μm scales. A few images were also obtained at higher magnifications, however, obtaining clear images was limited by the stones' irregular terrain and declining depth of field as a function of numerical aperture.

5.4 Results

5.4.1 Natural COM Stones

Figure 5.1 shows the natural structure of two different COM stones. Figure 1A has a rectangular crystal like growth pattern, while Figure 1B has a less structured, circular-like growth pattern. Both structures are partially ordered and have a distinctive form. Variation in shapes is not uncommon, as COM crystals have been reported to vary in both shape and form [85]. Constituent particle sizes ranged from 2-30 μm for the rectangular structure.

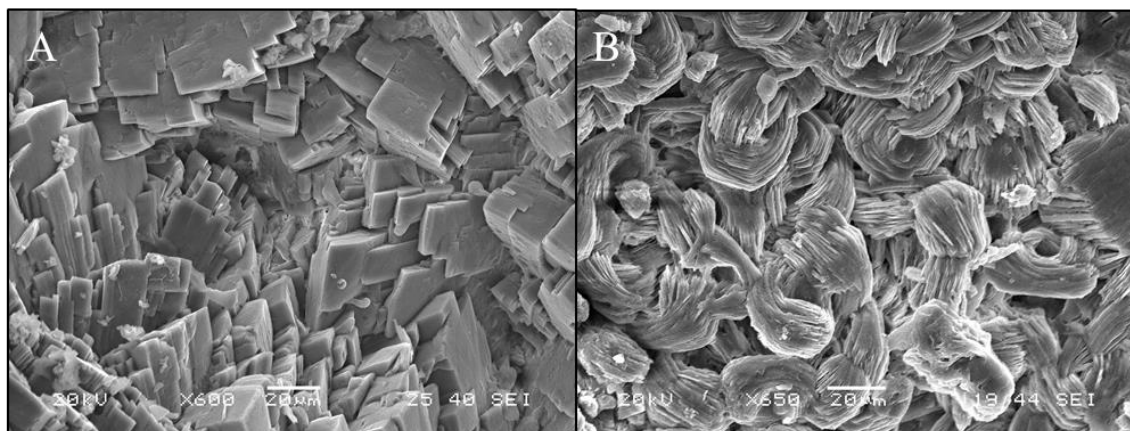


Figure 5.1. SEM images of different natural COM formations taken at magnifications of (A) 1,600 \times and (B) 1,100 \times .

5.4.2 Irradiation of COM Stones in Water at 1908 nm

The natural stone composition in Figures 5.2 and 5.3 corresponds to Figure 5.1B. After laser irradiation (1908 nm) of a COM stone in water, a char spot was observed in the crater with lighter discoloration surrounding it (Figure 5.2). There were numerous large fractures outside of the charred crater, presumably due to micro-explosions during ablation.

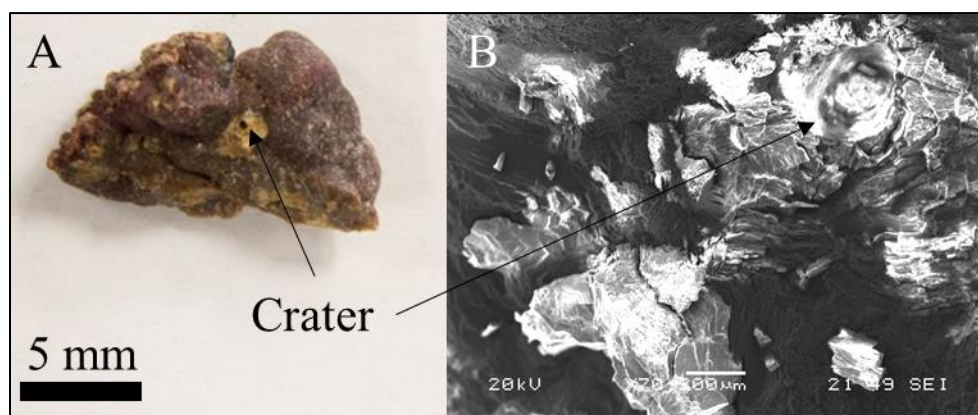


Figure 5.2. Ablation crater and char formed by irradiation from the 1908 nm TFL in a water environment. (A) Photograph of ablation crater with arrows designating char spot. (B) SEM image taken at 70 \times magnification.

SEM images inside of the crater are shown in Figures 5.3A-D. Figures 5.3AB are images inside the char spot. The natural material appears melted due to direct heating. Figures 5.3CD show a lighter discolored area around the char spot, and mechanical fracturing, presumably due to micro-explosions from subsurface heating of the water.

During laser irradiation in water, evidence of both thermal decomposition of material and micro-explosions in water, can be observed to affect the stone material. When comparing Figure 5.3 to a natural stone in Figure 5.1B, there is a significant difference. A combination of mechanical ablation and thermal decomposition apparently caused structures to take a more linear shape. This was not observed during irradiation of COM stones in air, as described below.

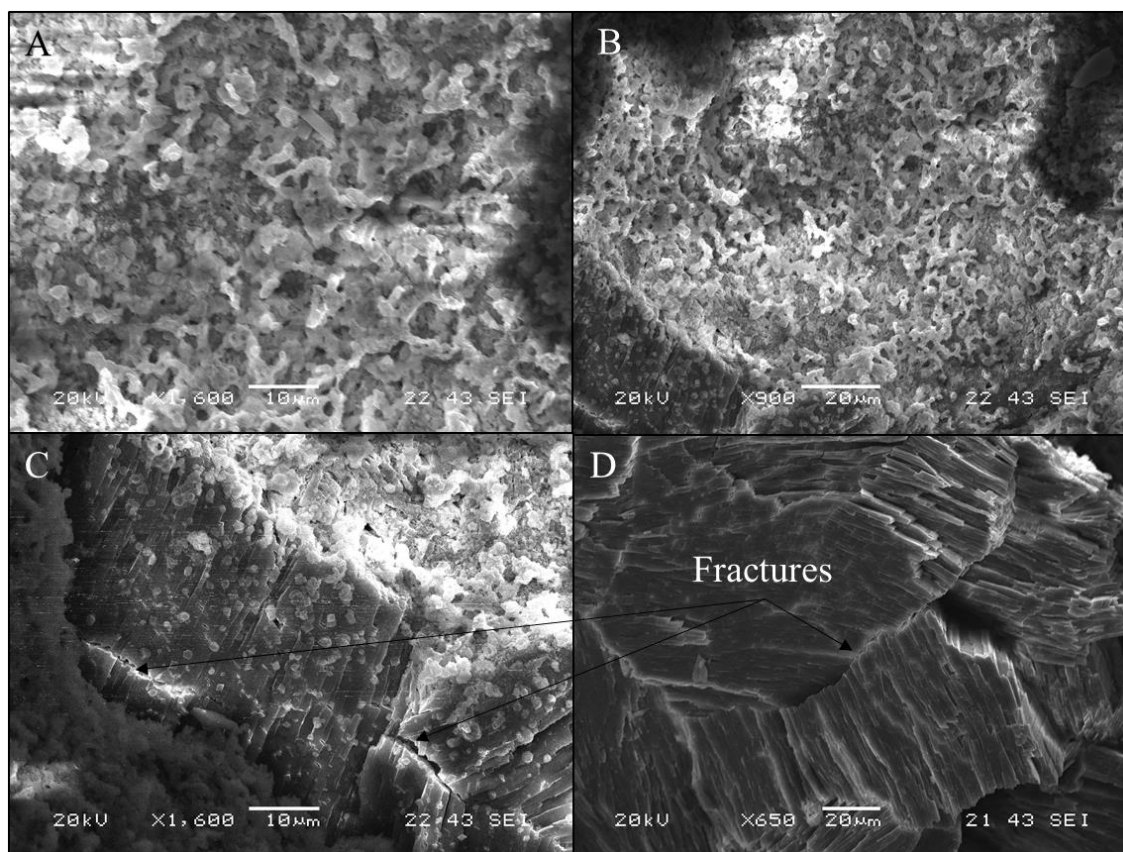


Figure 5.3. (A,B) SEM images taken at magnifications of 1,600 \times and 900 \times , inside the char spot of COM stones irradiated at 1908 nm in water, showing melting of calculi. (C,D) SEM images taken outside of char spot on COM stone, but inside crater, at magnifications of 1,600 \times and 650 \times , with arrows pointing to mechanically induced fracturing.

5.4.3 Irradiation of COM Stones in Air at 1908 nm

Laser irradiation (1908 nm) of COM stones in air produced significant ash, and the fiber jacket was ignited by the heat. Figure 5.4 shows the ash and SEM images of the ablation

crater. The ash was removed using compressed air to preserve the ablation byproducts. COM material was melted but there were no signs of mechanical damage inside or around the crater. The stone was examined at up to 12,000 \times magnification (not shown), with no signs of fracturing. The lack of observable mechanical damage (e.g. fractures) in the absence of water in this study lends further evidence to the observed mechanical component of ablation in hydrated stones being due to subsurface vaporization of water.

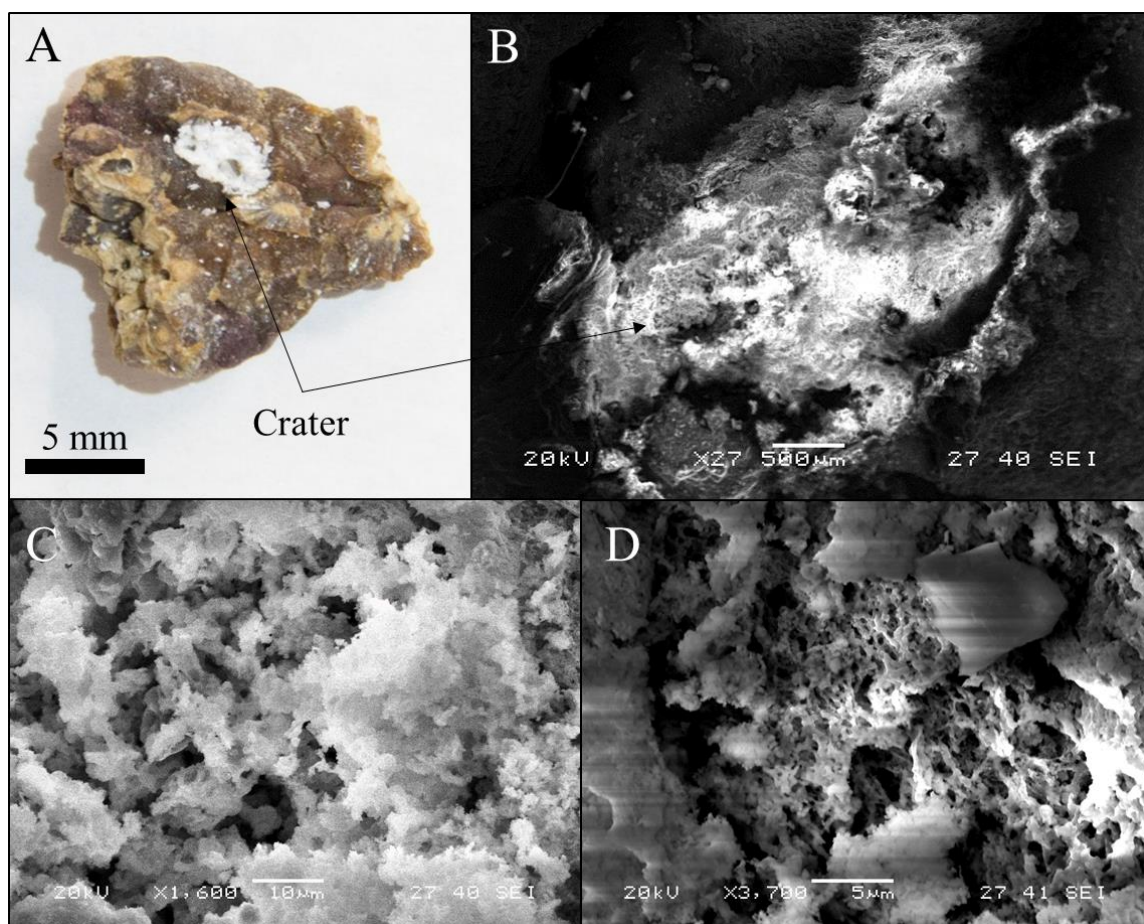


Figure 5.4. (A) Photograph of COM stone after irradiation in air with (B) SEM counterpart in image at 27 \times magnification. (C,D) COM stone irradiated in an air environment inside the crater at magnifications of 1600 \times and 3700 \times .

5.4.4 Natural UA Stones

The natural order of UA stones appears less organized when compared to COM material (Figure 5.5). The UA material has a distinct jagged edged polygonal shape of the

constituent particles, which are less uniform in size and shape compared to natural COM material. The particle sizes ranged from 1-40 μm , with no consistent shape.

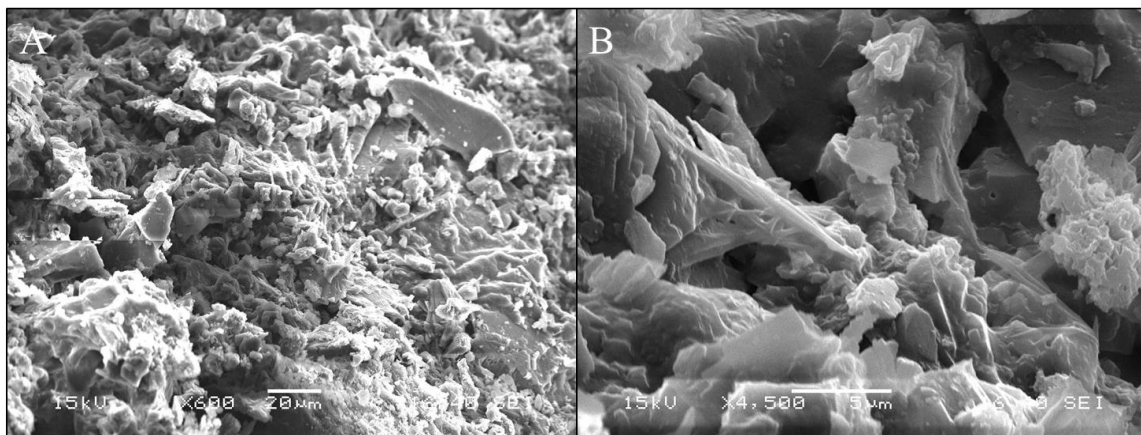


Figure 5.5. (A,B) SEM images of natural uric acid calculi taken at magnifications of 600 \times and 4,500 \times .

5.4.5 Irradiation of UA Stones in Water at 1908 nm

Minimal charring was observed during laser irradiation (1908 nm) of UA stones submerged in water, most likely due to energy being absorbed by the water. Figure 5.6 shows a photograph of ablation craters formed after laser irradiation and magnified SEM images. Mechanical fracturing was produced when the UA stone was irradiated in water. The stone sample remained similar to its natural state in Figure 5.5. The presence of mechanical damage is consistent with the higher thermal breakdown temperature, and lower Hounsfield unit, in a water environment for UA stones.

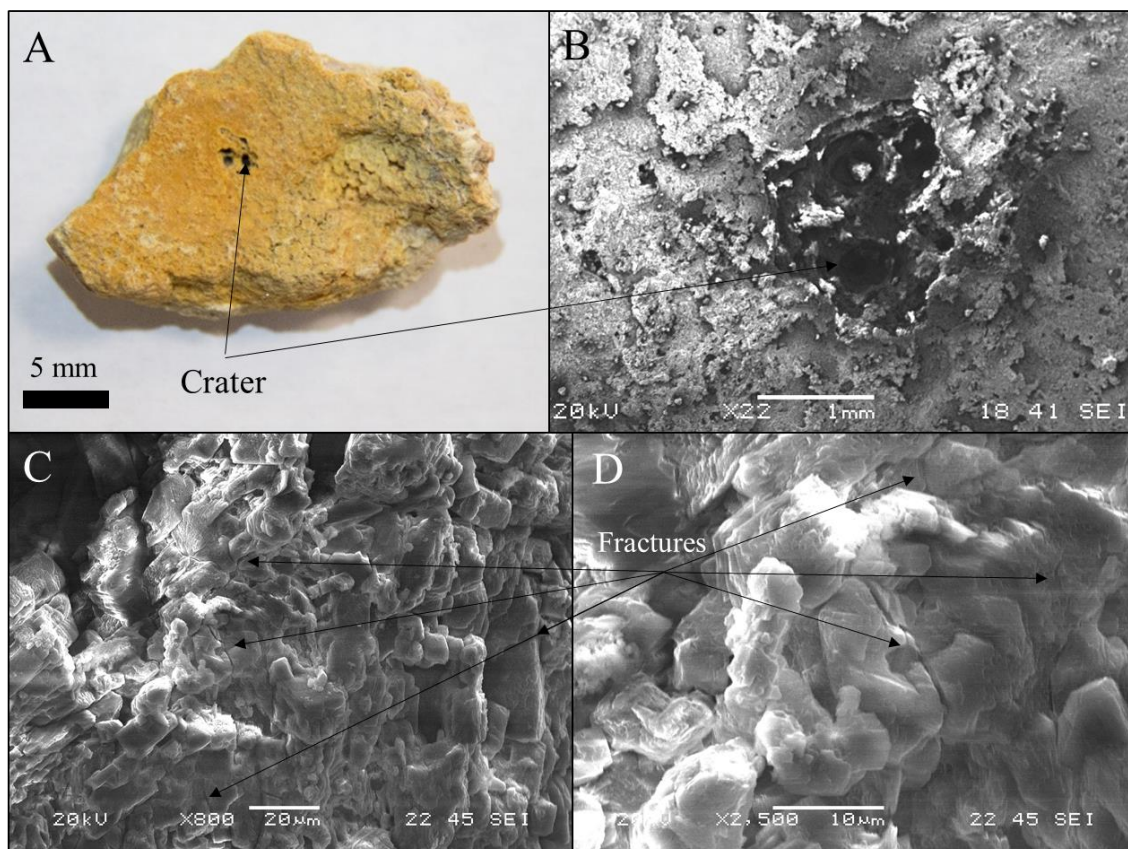


Figure 5.6. (A) Photograph of ablation crater in UA stone after irradiation at 1908 nm in water; (B,C,D) SEM images taken at magnifications of 22 \times , 800 \times , and 2,500 \times . Mechanical damage in the form of multiple fractures in (C) and (D), is shown by arrows.

5.4.6 Irradiation of UA Stones in Air at 1908 nm

Laser irradiation at 1908 nm of UA stones in air, resulted in significant charring of the stone surface. The heat generated during irradiation in air also ignited the jacket of the fiber. Figure 5.7 shows an image of the UA stone and the crater formed. However, the crater's size was too large to be imaged in its entirety using SEM. Magnified SEM images of the ablation crater show that there was no apparent mechanical damage on the UA stone. The natural calculi formations transformed from a rigid polygonal shape to bulbous spheres, due to melting from direct heating of the stone. The increase in charring is also consistent with the high thermal breakdown temperature, and the absence of fractures is consistent with the lack of water, as observed with laser irradiation of COM stones.

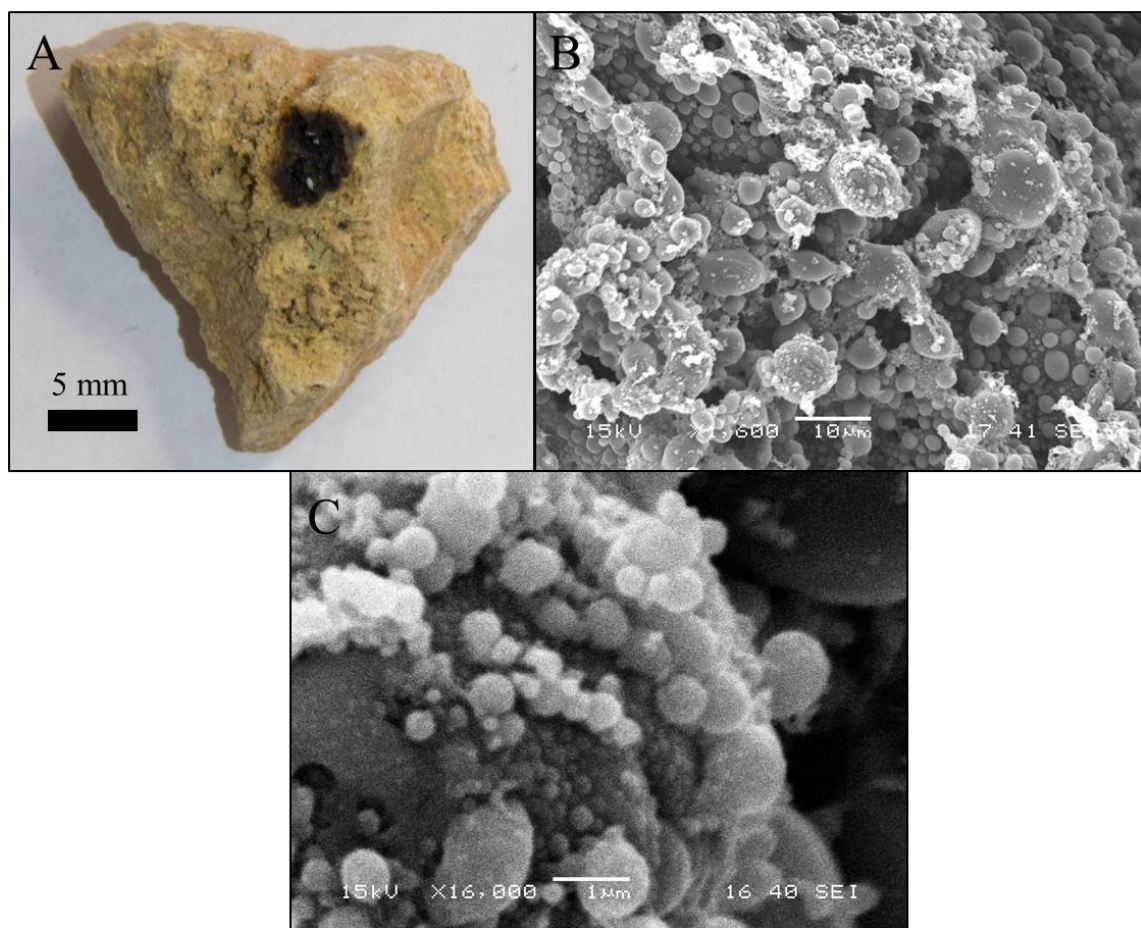


Figure 5.7. (A) Photograph of crater in UA stone after irradiation at 1908 nm in air. (B,C) SEM images at magnifications of 1,600 \times and 16,000 \times . Direct melting of the stone surface is observed, without any mechanical damage (e.g. fractures).

5.4.7 Irradiation of COM Stones in Water at 1940 nm

A 1940 nm TFL was operated at a higher pulse energy and a lower pulse rate, representative of a ‘fragmentation’ ablation mode. The average power and total energy delivered was kept the same as the low pulse energy and high pulse rate ‘dusting’ setting previously described. It should also be noted that the 1940 nm wavelength provided a slight decrease in water absorption when compared to the 1908 nm wavelength [39]. COM and UA samples were irradiated in a water environment with a TFL operating at 1940 nm. The COM sample did not char, but left a light discoloration compared to the rest of the stone (Figure 5.8). Melting of the material is shown in magnified SEM images, but a

majority of the calculi is mechanically fractured. There also appears to be a more substantial amount of fracturing in comparison to COM irradiation in water by the TFL at 1908 nm with lower pulse energy of 35 mJ.

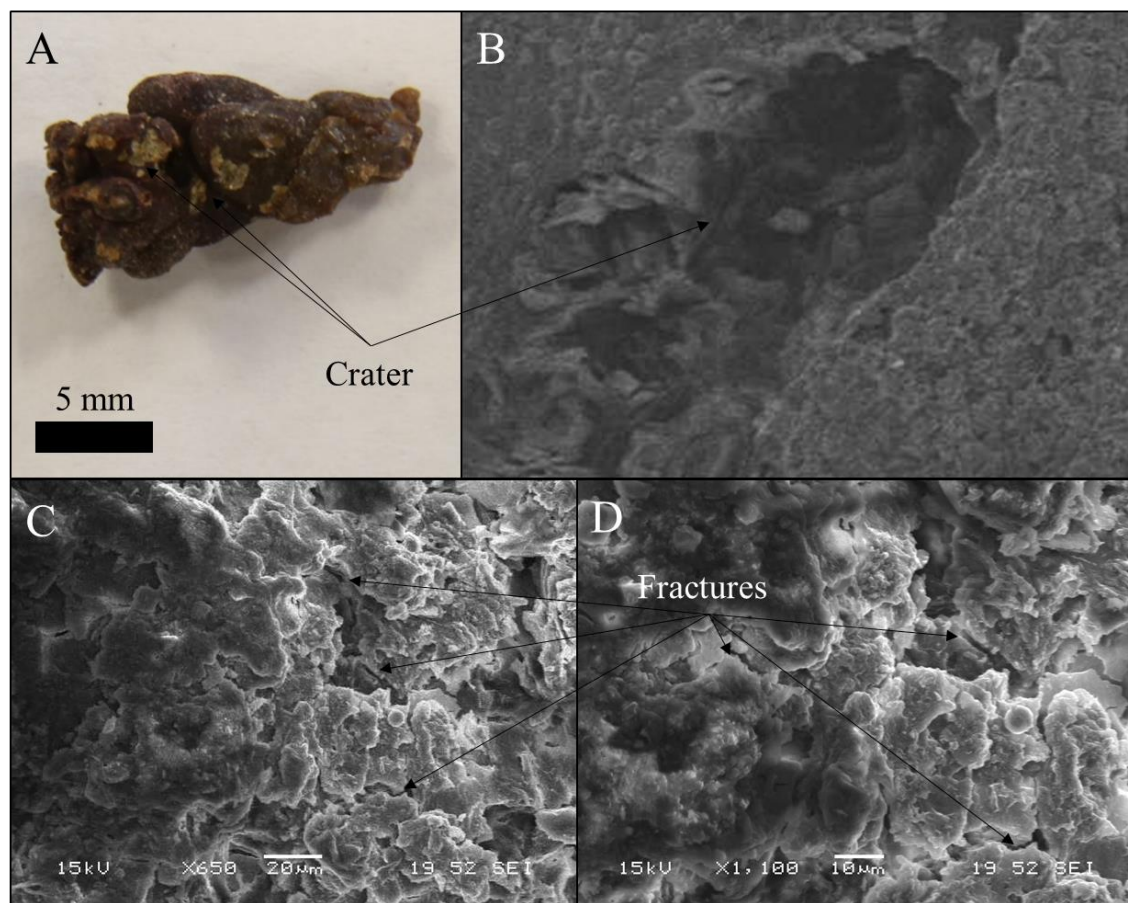


Figure 5.8. (A) Photograph of COM stone in water after irradiation at 1940 nm with high pulse energy. (B,C,D) SEM images at magnifications of 60 \times , 650 \times , and 1,100 \times . (C,D) Significant fracturing due to micro-explosions, with a small amount of melting in the material is observed.

5.4.8 Irradiation of COM Stones in Air at 1940 nm

Ash and charring of COM stones in air were produced from TFL irradiation at 1940 nm and high pulse energy (Figure 5.9). The resulting crater was similar to the crater left behind from irradiation at 1908 nm with a COM stone. The magnified SEM images show melting of the COM stone very similar to the SEM images of irradiation with a 1908 nm

wavelength. The primary ablation mechanism is most likely thermal breakdown of the hard tissue.

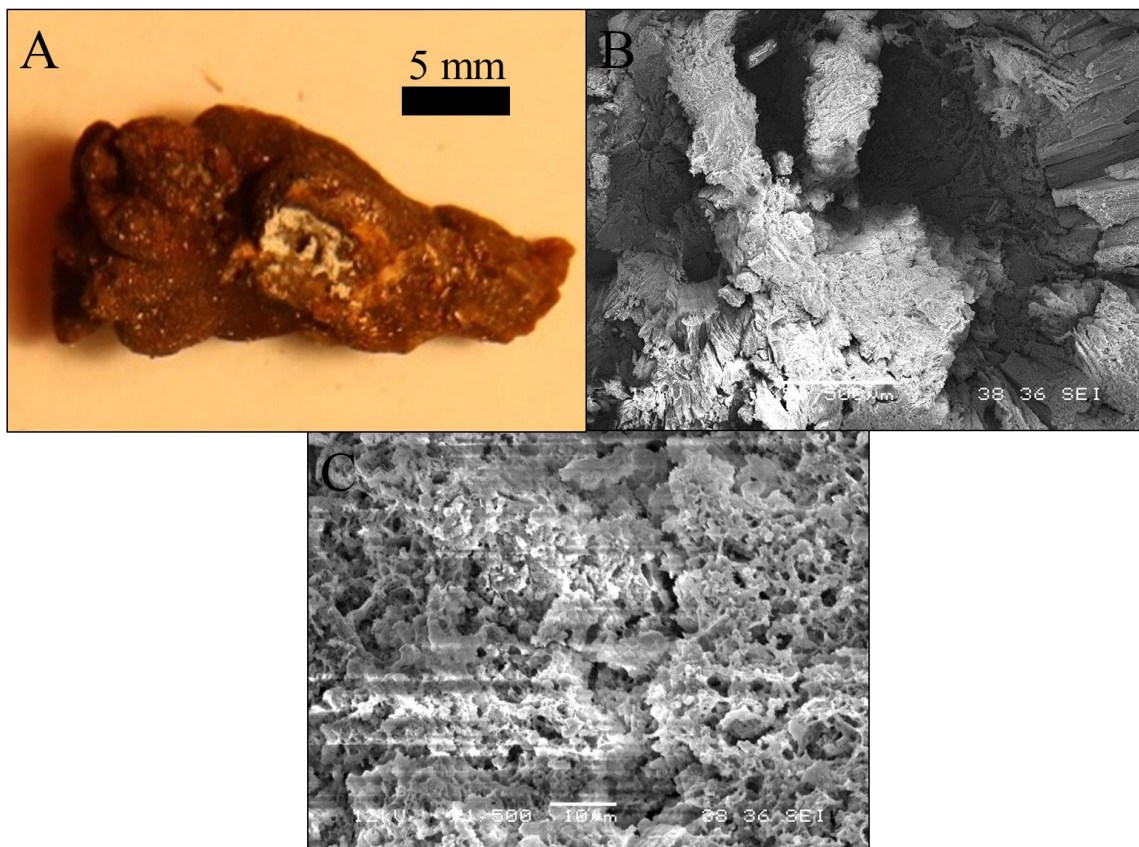


Figure 5.9. (A) Photograph of COM stone after laser irradiation at 1940 nm in air. (B,C) SEM images of ablation crater taken at magnifications of 50 \times and 1500 \times . (C) Melted material caused by thermal build up from direct absorption of light by stone material.

5.4.9 Irradiation of UA Stones in Water at 1940 nm

Thermal ablation and melting was more apparent in the UA samples (Figure 5.10). Stone material was fused together due to melting, but mechanical fracturing was also observed as well. Although difficult to quantify, mechanical fracturing appeared more widespread during TFL irradiation at 1940 nm, consistent with observations for COM stones. This was presumably due to higher pulse energy from 1940 nm laser, which increased the amount of water vaporized [86].

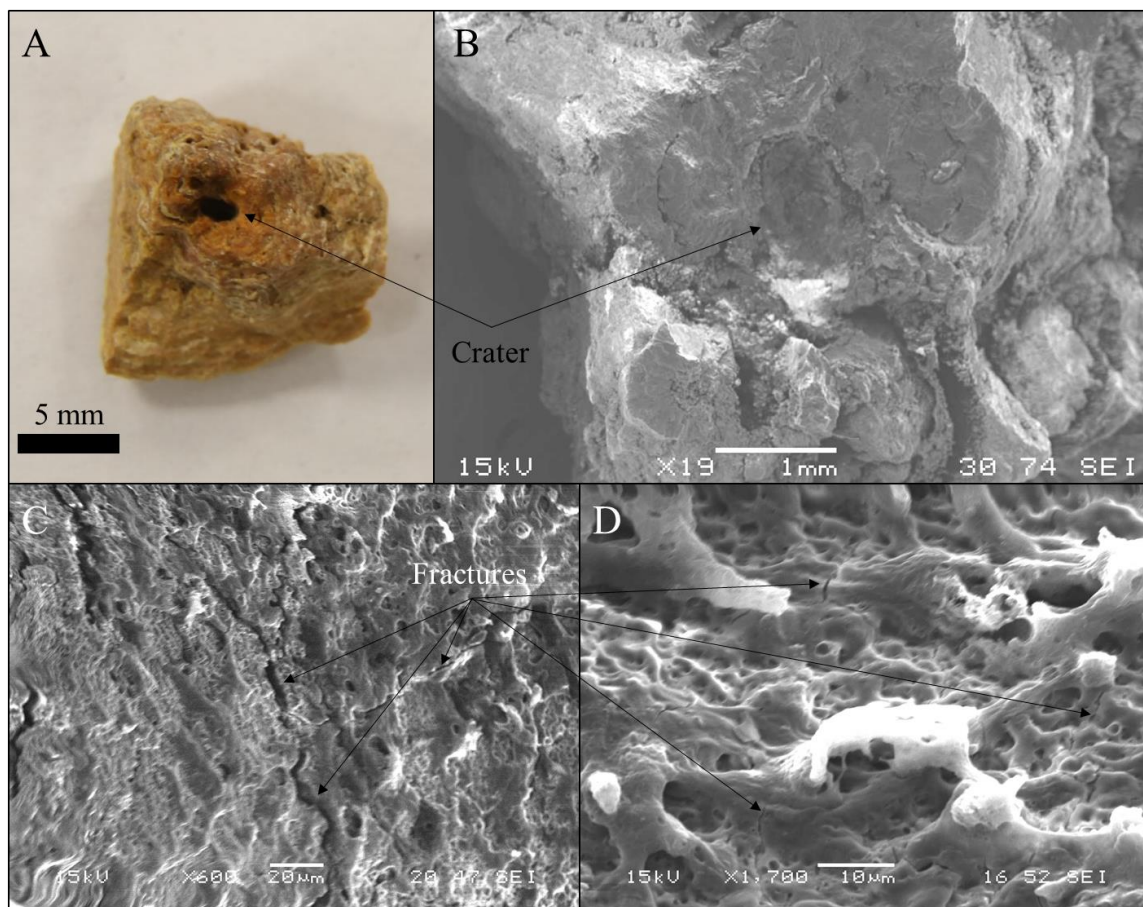


Figure 5.10. (A) Photograph of UA stone in water after irradiation at 1940 nm with high pulse energy; (B,C,D) SEM images at 19 \times , 600 \times , and 1,700 \times magnification. Significant mechanical fractures are present as indicated by the arrows.

5.4.10 Irradiation of UA Stones in Air at 1940 nm

A large amount of heat and char was produced during laser irradiation (1940 nm) of UA stones in air (Figure 5.11). There were no signs of mechanical fracturing, consistent with the micro-explosion theory. The crater was similar to the charred crater created in a UA stone at 1908 nm. The resulting magnified SEM images show melting of the native stone material. The primary mode of ablation was most likely direct absorption and thermal breakdown of the material.

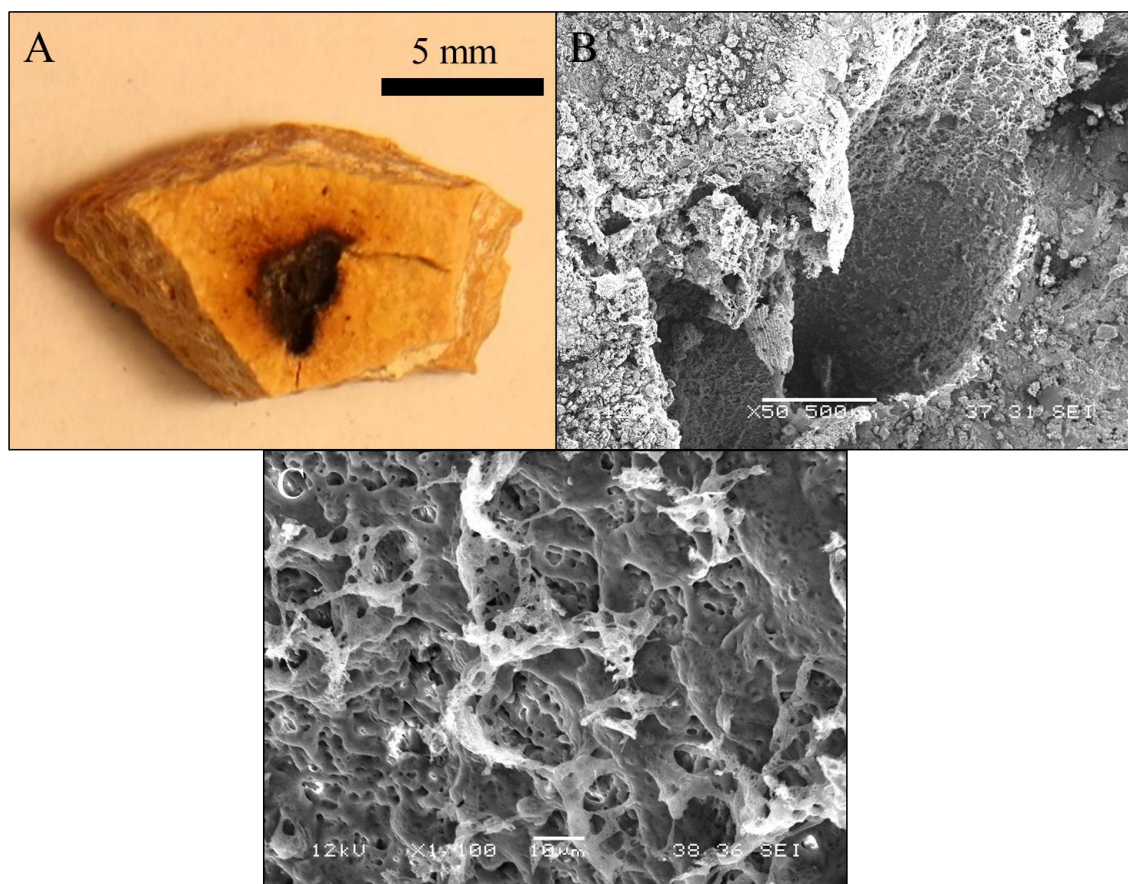


Figure 5.11. (A) Photograph of UA stone after laser irradiation at 1940 nm in an air. (B,C) SEM images at 50 \times , and 1,100 \times magnification. (C) The material inside of the crater has been melted from direct photothermal interaction with the laser light.

5.4.11 BegoStone Artificial Stone Phantom

The natural material of BegoStone does not take a well-defined shape. The constituent particle sizes range from 2 to 20 μm . Some constituent particles appear to be fused together like a homogeneous medium, while other parts look to be independent building blocks. Laser irradiation (1908 nm) of BegoStone was conducted (Figure 5.12). Magnified SEM results of BegoStone in water are inconclusive. Material inside of the crater is similar to the BegoStone's natural state. Fracturing was not observed. A proposed explanation of these observations is that the micro-explosion process ablates by taking apart constituent particles rather than by fracturing an amorphous medium. Laser irradiation (1908 nm) of

BegoStone in air is consistent with this theory. The material inside the crater appears to be melted and smoothed over. Figure 5.12A-C shows a representative image of the natural material as well as each ablation process.

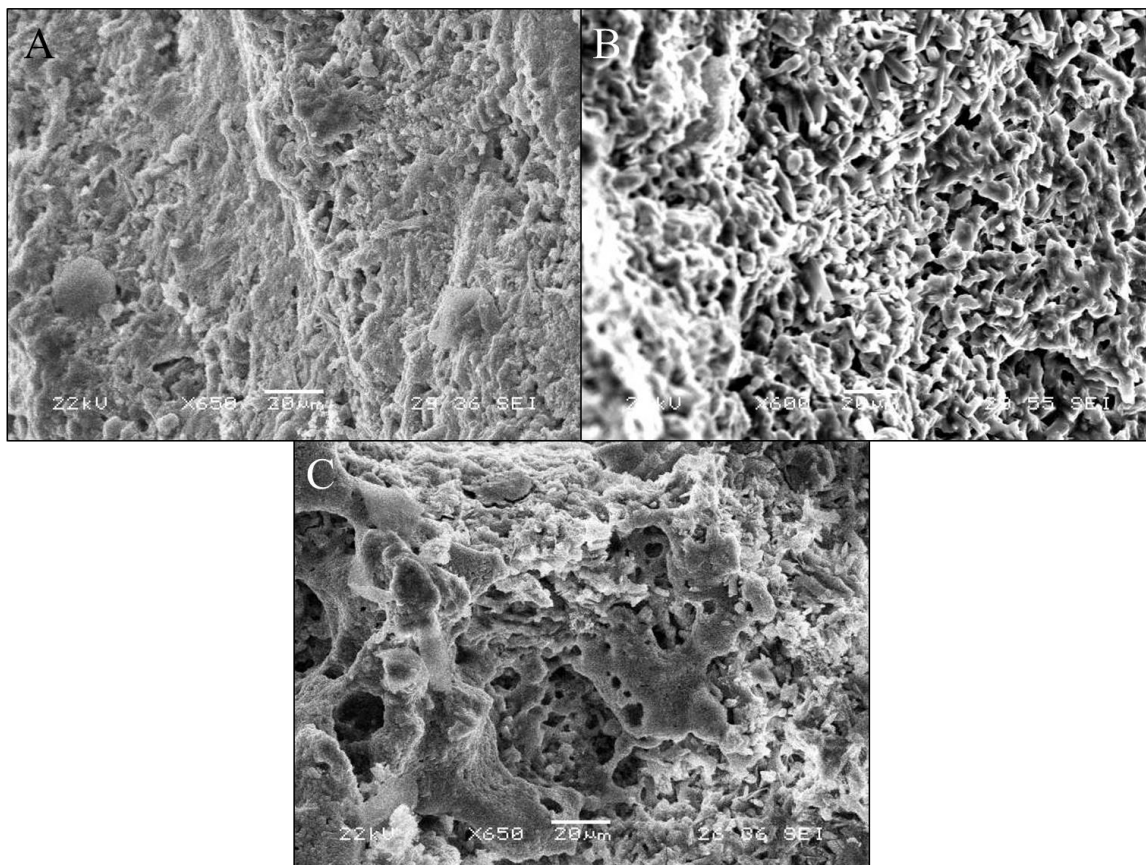


Figure 5.12. SEM images of BegoStone stone phantoms at 600× and 650× magnification with (A) natural material, and after irradiation in (B) water, and (C) air environments using a 1908 nm wavelength laser.

BegoStone stone phantom was also irradiated using a 1940 nm wavelength in both water and air (Figure 5.13). Laser irradiation (1940 nm) in water produced similar results to laser irradiation at 1908 nm. Magnified SEM images inside the crater show minimal change in the natural state of the material. This is most likely due to micro-explosions ablating the material where the constituent particles are connected, which leaves minimal fracturing of the material after ablation. Irradiation in an air environment produced expected results.

The material inside the crater appeared to be melted and fused together. This is similar to what was observed after laser irradiation at 1908 nm.

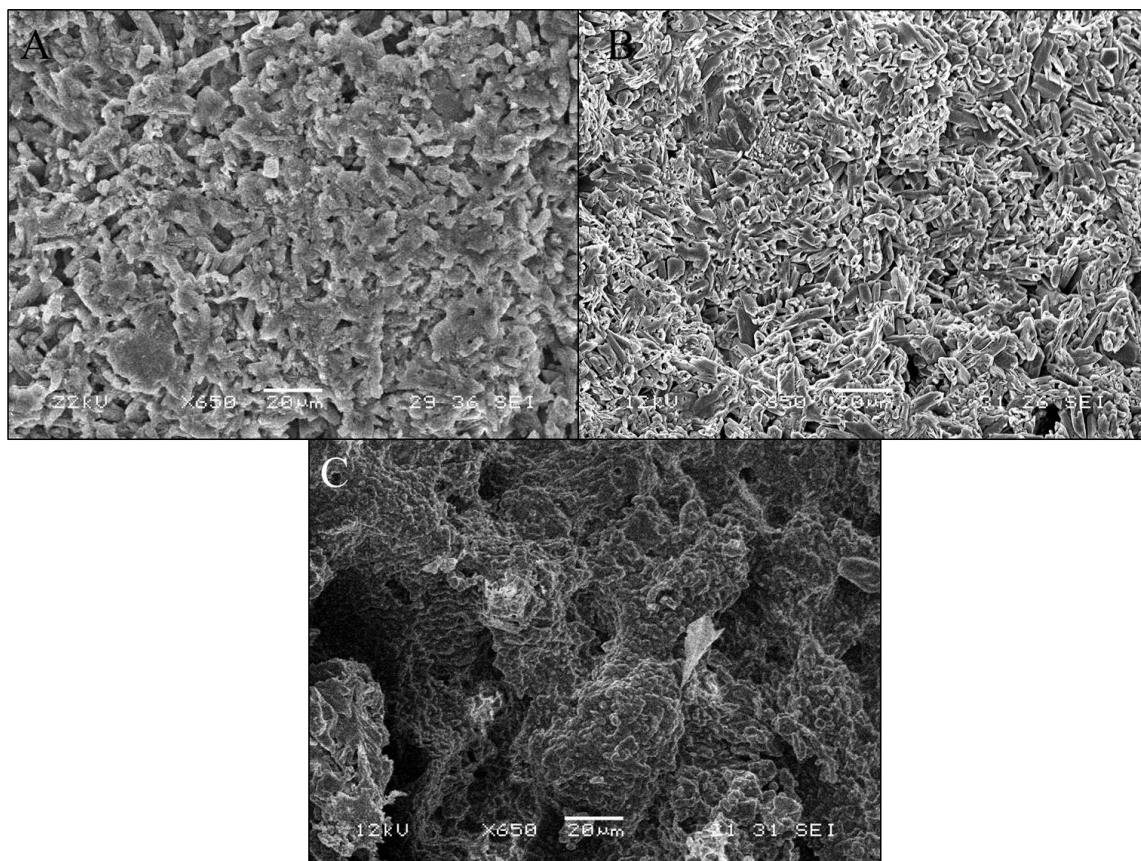


Figure 5.13. SEM images of BegoStone material at 650 \times magnification with (A) natural material, and laser irradiation at 1940 nm in (B) water, and (C) air.

5.4.12 UltraCal30 Artificial Stone Phantom

Another common stone phantom, UltraCal30, was examined. UltraCal30 was irradiated at both 1908 and 1940 nm wavelengths in water and air. At 1908 nm, ablation in water produced a crater with little to no charring of the material. However, SEM magnified images show that at both 1908 and 1940 nm, the material is similar to its natural state. This is the same result observed after laser irradiation of the BegoStone stone phantom using both wavelengths. Ablation at 1908 nm in air produced char and a small ablation crater. The material inside of the crater showed some signs of melting and possible fracture points.

However, the altered material was not markedly different from the material's natural state. This makes it difficult to assume the primary ablation mechanism and therefore makes the results inconclusive. SEM images after laser irradiation at 1908 nm, in air and water, are shown in Figure 5.14B-C.

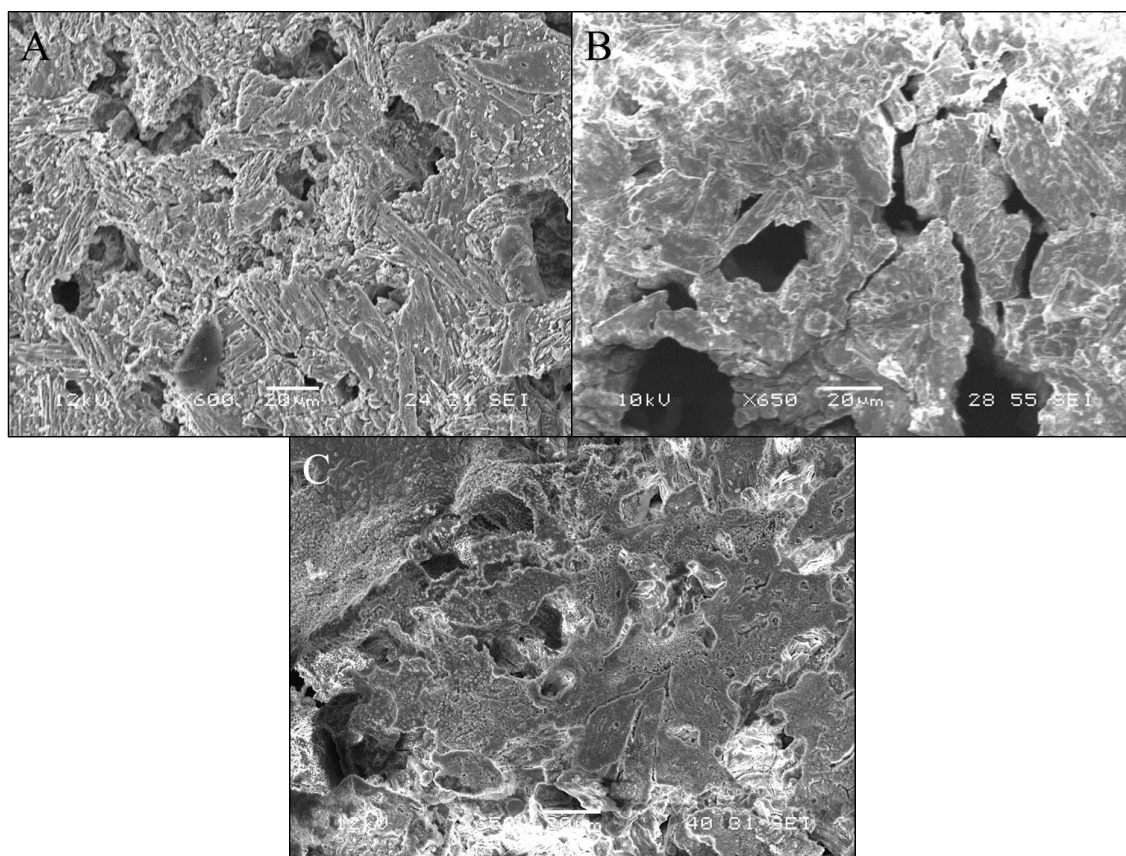


Figure 5.14. SEM image of UltraCal30 stone phantoms at 600 \times and 650 \times magnifications of (A) natural material, and laser irradiation at 1908 nm in (B) water, and (C) air.

Interestingly, laser irradiation at 1940 nm of UltraCal30 in air produced no char. There was minimal alteration of UltraCal30 material. The material inside the crater did not show any signs of melting or fracturing. It is possible that the light was coupling into water inside the stone phantom, placed there during preparation of the sample. However, the results are still inconclusive for the primary ablation mechanism. Figure 5.15A-C shows representative images of each experimental state for the 1940 nm laser studies.

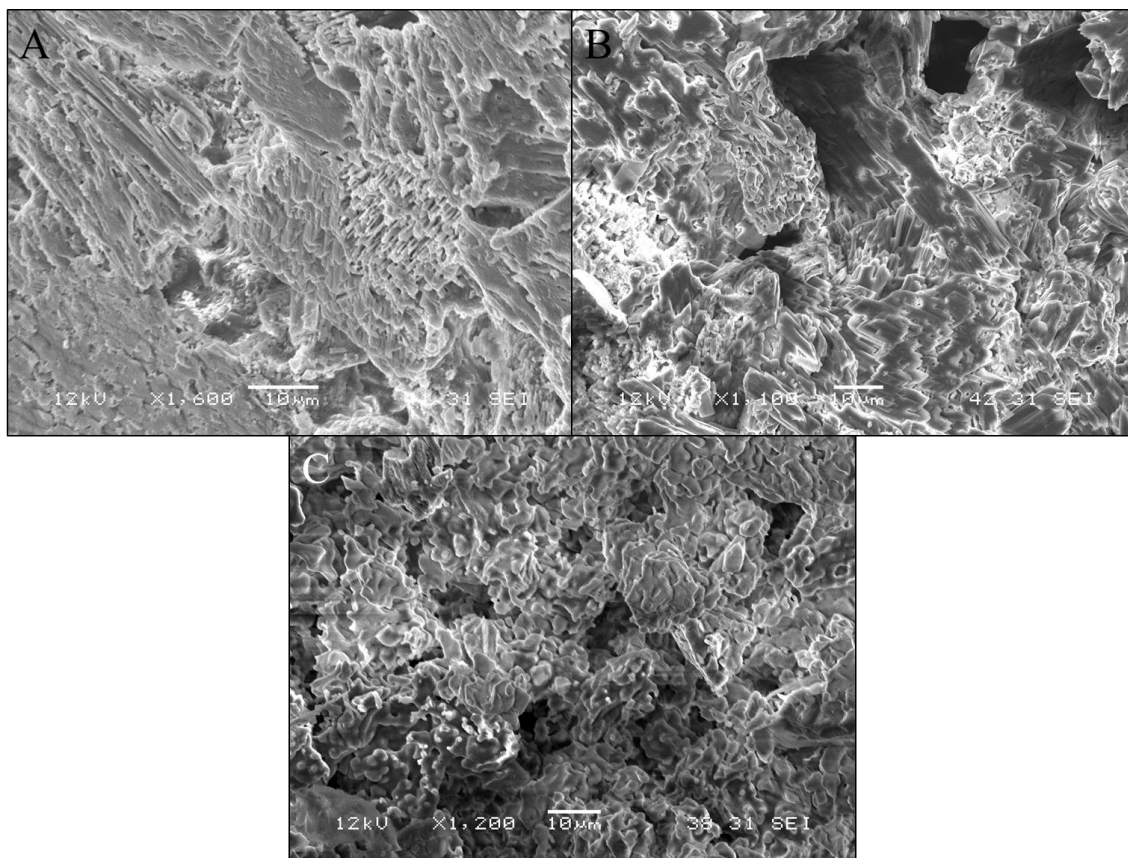


Figure 5.15. SEM image of UltraCal30 stone phantom at 1,100 \times - 1,600 \times magnifications of (A) natural material, and laser irradiation at 1940 nm in (B) water, and (C) air.

5.4.13 UltraCal30 and BegoStone Artificial Stone Phantom Results

Each stone phantom was irradiated by a TFL at 1908 and 1940 nm in air and water environments. The air environment results typically resembled what would be expected, e.g. melting of the material. However, there were only small signs of fracturing observed in UltraCal30 irradiated in water. There was minimal evidence of melting with the samples, and both materials appeared similar to their natural state when in a water environment. Widespread micro-fractures were not observed, unlike for UA and COM stones irradiated in a water environment. These differences between UltraCal30/BegoStone phantoms and natural kidney stones suggest that artificial stones

are not representative models for laser lithotripsy studies. Future ablation studies will be considered to confirm this interpretation.

5.5 Discussion

SEM images of COM and UA stones show that they have different physical properties, which is critical in determining the stone ablation mechanism. Table 5.1 provides the thermal breakdown temperature, Hounsfield unit density, and ablation threshold for different kidney stones. The Hounsfield unit density (HU/mm) for COM is larger than for UA, so COM stones are more dense [80]. A UA stone has a higher melting temperature, but a lower Hounsfield unit and would be more likely to ablate through micro-explosions before thermal breakdown occurs. This was observed when comparing SEM images of each stone irradiated with the TFL at 1908 nm in water. The UA material appeared similar to its natural state, but with significant fracturing, while COM was primarily melted with some fracturing present. Therefore, both mechanical and thermal properties of kidney stones greatly influence the primary ablation mechanism.

Another influential factor in ablation is the surrounding medium. Air and water environments were examined in this study. Both 1908 and 1940 nm TFL wavelengths are highly absorbed in water due to a high temperature water absorption peak near 1910 nm and a low temperature water absorption peak near 1940 nm [39]. During laser irradiation in water, the water acts as the primary absorber. This decreases the radiant heat, and also promotes the ablation process through micro-explosions. Both COM and UA stones irradiated in water exhibited more fracturing than when they were irradiated in air. There was still evidence of primary absorption by the material itself, indicated by melting of the natural material when examining the COM stone irradiated by TFL at 1908 nm in water.

However, this may be due to the fiber being kept fixed during irradiation, resulting in charring on the stone, and thus artificially increasing the absorption coefficient of the material. This is most likely the case, because the amount of char for COM irradiated in water was much less than observed in air.

Furthermore, it should be noted that the specific technique of controlling the optical fiber during the procedure may also influence the primary ablation mechanism. For example, there are at least two general ways of controlling the fiber during irradiation, “drilling” and “scanning”. The drilling technique consists of advancing the distal fiber optic tip further into the stone during formation of the ablation crater. This approach results in rapid evaporation of the water, leaving no path for excess heat to diffuse, thus resulting in charring of the stone. This char formation in turn artificially increases the absorption coefficient of the material, causing the primary ablation mechanism to be predominantly thermal in nature. On the contrary, the scanning method involves moving the distal fiber optic tip laterally across the stone surface during ablation. This approach allows better heat diffusion by water, and promotes the micro-explosion mechanism. A mixture of both techniques of manipulating the fiber was used during these experiments, in an effort to simulate the technique applied during a typical clinical procedure.

Laser irradiation of the stone in air only enabled ablation through direct absorption, thus creating significant heat, not only producing significant charring of both UA and COM stones, but also igniting the fiber jacket. SEM images show melting of the material with minimal signs of fracturing, which is thought to be caused by micro-explosions.

The artificial stone phantoms did not leave behind ablated surfaces similar to those seen with real kidney stones during irradiation in both water and air environments. It is believed

that the absence of melted material during ablation in air is due to the laser primarily coupling into the high water content (20% and 38% water content for Begostone and Ultra Cal30, respectively) in both artificial stone types, resulting in less energy being absorbed by the stone material.

The differences in ablation in a water environment between artificial and real kidney stones may be caused by several factors. First, the artificial stones could be separating at the bonding point of the constituent particles during the micro-explosion ablation. This would not leave fracture planes in the material after ablation. Second, the absorption coefficient of the artificial material may be significantly lower than the absorption coefficient of the natural material. Optical absorption by kidney stones has been analyzed at infrared wavelengths of 2.5 μm and greater [87]. However, limited data is available in the 1-2 μm wavelength regime for artificial and real kidney stones.

The two competing ablation processes are also influenced by laser parameters. There are two primary ablation modes used during lithotripsy, ‘dusting’ and ‘fragmentation’ [51][88]. Both regimes are dependent on laser pulse energy and pulse rate. Dusting occurs at low pulse energies and high pulse rates, while fragmentation occurs at high pulse energies and low pulse rates. The TFL at 1908 nm was operated in dusting mode (35 mJ / 300 Hz), and the TFL at 1940 nm in fragmentation mode (200 mJ / 53 Hz), based in part on technical limitations of the 1908 nm laser. SEM images show that more fractures occurred using the 1940 nm laser parameters for COM and UA stones, while more melting was observed using the 1908 nm laser parameters. Table 5.2 summarizes the observations for the different parameters explored.

Initially, stone pore size was also to be studied. However, the stone surfaces did not exhibit open pores. There was some evidence of subsurface pores after stones were physically broken apart. However, SEM images were not taken of altered stones because mechanical damage caused during the separation process may potentially create artificial pores and fractures not present in the stone's natural state.

Table 5.2. Qualitative description of ablation effects on kidney stones and stone phantoms as a function of medium, wavelength, and stone composition.

Medium	Wavelength (nm)	COM	UA	Ultracal30	BegoStone
Native State	NA	Crystal like with several formations	Jagged polygonal structures, no distinct structure	Non-uniform constituent particles, no distinct structure	Non-uniform constituent particles, no distinct structure
Ablation in Air	1908	Significant ash, structure fused together (thermal damage)	Significant char, material melted into round structure (thermal damage)	Small signs of melting. May have some fracturing.	Melting of material
	1940	Significant ash, structure fused together	Significant char, material fused together from melting	Signs of melting, possible fractures	Ash produced, material melted into round structure
Ablation in Water	1908	Minimal char with fused material & fracturing outside char zone (thermal & mechanical damage)	Minimal char, no observed fusion of material & significant fracturing inside crater (mechanical damage)	No melting, large fractures in material	No melting or observable fractures
	1940	No charring, minimal fusion of material & significant fracturing (mechanical damage)	Char observed with fusion of material & significant fracturing (thermal & mechanical damage)	Possible signs of melting, no signs of fracturing	No melting or observable

COM = Calcium Oxalate Monohydrate; UA = Uric Acid

5.6 Conclusion

The effects of both direct thermal ablation (e.g. melting and decomposition) as well as micro-explosions (e.g. cracks and fractures) were observed in scanning electron microscopy images, showing that both long pulse, infrared laser ablation processes depend on multiple factors, including laser energy, stone composition, and surrounding environment. These results should help determine optimum laser parameters for ablation of uric acid and calcium oxalate monohydrate kidney stones, which are commonly encountered during laser lithotripsy in the clinic. Furthermore, both UltraCal30 and BegoStone artificial stone phantoms, commonly used in laser lithotripsy laboratory studies, were found to be un-representative of real kidney stone samples for studying the ablation mechanism. Future ablation rate studies are also planned to quantify stone ablation rates as a function of laser energy, stone composition, and stone environment.

CHAPTER 6: Comparison of 1908 and 1940 nm Wavelengths for Thulium Fiber Laser Lithotripsy

6.1 Introduction

Current high power TFLs operate at 1940 nm, a more efficient and less expensive wavelength [29][30][31]. The 1940 nm ($\mu_a = 120 \text{ cm}^{-1}$) wavelength matches a low temperature water absorption peak, producing a $\sim 27 \%$ increase in low temperature water absorption coefficient compared with the 1908 nm wavelength ($\mu_a = 88 \text{ cm}^{-1}$) [40]. However, this trend is reversed, with a $\sim 13 \%$ increase in the high temperature water absorption coefficient between the $\lambda = 1908 \text{ nm}$ ($\mu_a = 155 \text{ cm}^{-1}$) and $\lambda = 1940 \text{ nm}$ ($\mu_a = 135 \text{ cm}^{-1}$) (Figure 1.4) [39]. This change in water absorption at 1940 nm may potentially result in a higher ablation threshold and translate into lower ablation efficiency and ablation rates.

Water is well known to be a major absorber of IR laser radiation, and therefore plays a primary role in the ablation mechanism for both soft and hard tissues, including laser lithotripsy. The dynamic absorption coefficient of water has been studied in the near to mid-IR spectrum [39][40][41][89][90]. The low-temperature 1940 nm water absorption peak at 22 °C shifts to 1920 nm at higher water temperatures, measured up to 70 °C [39]. Due to the dynamic absorption coefficient of water, as well as a wide range of laser parameters and stone compositions encountered during lithotripsy, the exact stone ablation mechanism is difficult to understand, but is attributed to several mechanisms, including photothermal absorption by the stone material and resulting chemical decomposition, as well as micro-explosions due to absorption and thermal expansion of water in the cracks and pores near the stone surface [20][81][91].

The connection between dynamic water absorption and laser ablation has been studied extensively [38][92][93][94][95]. Previous studies have analyzed the effect of a dynamic water absorption coefficient on tissue ablation, using different methods. Several studies measured ablation threshold and ablation rates as metrics for ablation efficiency [38][92]. The soft tissue ablation threshold varied inversely with the water absorption coefficient, consistent with simple ablation models. However, for hard tissues (e.g. bone) there was minimal difference in ablation threshold as a function of wavelength presumably due its lower water content. A similar effect may be observed with kidney stones. Previous experiments lead to the hypothesis that due to low water content and small difference in wavelength that the 1908 and 1940 nm wavelengths will have similar ablation thresholds, and ablation rates.

Other experiments quantified thermal damage depth near the ablation crater as another metric for ablation efficiency [93]. While thermal damage to kidney stones is not a clinical concern and therefore was not analyzed, several interesting conclusions were made on the effect of dynamic water absorption. A general convention to limit thermal damage is to choose a laser pulse duration less than the thermal diffusion time, for a given tissue and laser wavelength [93]. The thermal diffusion time varies inversely with the tissue absorption coefficient, so higher absorption yields a shorter thermal diffusion time. When using a pulse duration below the thermal diffusion time of the tissue, a simple model can be used to determine thermal damage based on the threshold fluence and absorption coefficient of the tissue. However, for an Er:YAG laser (2.94 μm), thermal damage observed was a much as 100 times greater than the predicted of 1 μm thermal damage depth calculated with the simple model, for a train of micropulses delivered below the thermal

diffusion time. This difference between theory and experiment was explained by a dynamic change in absorption coefficient during tissue ablation that can alter ablation mechanism [93]. This experiment showed that a difference in absorption coefficients between wavelengths is not the only criteria for determining ablation efficiency.

Another study showed that little to no difference in low temperature water absorption between wavelengths produced a noticeable difference in ablation, due to the shift in water absorption as a function of temperature [94]. A comparison between Er:YAG (2.94 μm) and Er:YSGG (2.79 μm) lasers for short pulse ablation was conducted. Due to the dynamic change in absorption coefficient as a function of energy, the Er:YSGG laser wavelength had a larger effective absorption coefficient than Er:YAG laser wavelength, contrary to predictions based on static, low temperature water absorption coefficients. This in turn resulted in Er:YSGG laser wavelength having a shorter penetration depth.

One study concluded that despite a significant difference in water absorption coefficients between Thulium:YAG (2.01 μm) and Holmium:YAG (2.12 μm) wavelengths (Figure 7.1), no difference in ablation rates was observed [95]. The study analyzed thermal damage, ablation rate, and threshold radiant exposure to determine ablation efficiency. Although the low temperature water absorption coefficient was 2.7x greater for Thulium:YAG wavelength, there was no statistical difference for any of the metrics measured, likely due to only a small change in the water absorption coefficient. This previous finding strengthens our hypothesis of there being minimal statistical difference in ablation threshold and ablation rates between the TFL wavelengths of 1940 and 1908 nm.

The tissue ablation process of long pulse lasers utilizes several physical phenomenon and is therefore difficult to predict based on a difference in a single physical parameter.

The purpose of this study is to determine whether there is a measurable difference in kidney stone ablation threshold and/or ablation rates between the two main TFL wavelengths, 1908 and 1940 nm, using similar laser parameters.

Previous studies have also looked at the production of TFL induced vapor bubbles from near-IR radiation [86]. This information is important because laser lithotripsy procedures are conducted in a water environment. Vapor bubbles enable non-contact transmission of the laser energy to the kidney stone. The bubble dimensions and dynamics relate to stone repulsive forces and effective ablation distance. A longer length vapor bubble allows the light to travel further and thus increase the effective range at which non-contact ablation can occur. However, too long of a vapor bubble may increase the probability of complications such as collateral damage to adjacent soft tissues such as the ureter wall. Previous experiments have examined the TFL emitting at a 1908 nm wavelength and found an effective range of ~ 1 mm, much shorter than the Ho:YAG range of 4-5 mm. The third arm of this study will analyze and compare bubble dimensions and dynamics for both TFL wavelengths.

6.2 Methods

6.2.1 Thulium Fiber Laser Parameters

Two Thulium fiber lasers were tested (Figure 6.1). The first TFL was a 100 W, continuous-wave (CW) laser (TLR 100-1908, IPG Photonics, Oxford, MA) with 1908 nm wavelength, electronically modulated using a function generator (DS345, Stanford Research Systems, Sunnyvale, CA) to produce 500- μ s pulses, similar to Ho:YAG laser pulse lengths of 350-700 μ s. The TFL produced a Gaussian mode beam profile, originating from an 18- μ m-core thulium-doped silica fiber, with a built-in collimator providing a 5.5-

mm-diameter output beam. A 25-mm-focal-length AR-coated lens was used to focus the collimated TFL beam down to a $1/e^2$ spot diameter of $\sim 25 \mu\text{m}$, for coupling into a 200- μm -core, low-OH, silica optical fiber (FP200ERT, Thorlabs, Newton, NJ) with 0.22 numerical aperture (NA), for use in stone ablation studies. All experiments were performed with similar laser parameters to previous published studies (Table 6.1) [44]. The lower pulse energy, high pulse rate laser settings was representative of a ‘dusting’ ablation mode.



Figure 6.1. Thulium fiber lasers operating at (A) 1908 nm and (B) 1940 nm.

Table 6.1. Laser and fiber parameters used for 1908 and 1940 nm wavelength Thulium fiber lasers.

Pulse Energy (mJ):	35
Pulse Duration (μs):	500
Pulse Rate (Hz):	300
Average Power (W):	10.5
Fiber Core Diameter (μm):	200

A second TFL (TLR-50/500, IPG Medical, Marlborough, MA) with 1940 nm wavelength, was operated in pulsed mode, and capable of 500 W peak power, 50 W average power output. Peak power, pulse rate, and pulse duration were modulated electronically by internal software. A 200- μm -core silica fiber (FP200ERT, Thorlabs) with 0.22 NA and SMA connector was attached to the laser. All experiments used same laser parameters for both lasers (Table 6.1).

To confirm that two lasers were operated using similar parameters, both the power and pulse duration were externally calibrated. The power was calibrated using a power sensor (PM100-19C, Coherent, Santa Clara, CA) and meter (EPM2000, Molectron, Portland, OR). Pulse energy was determined by dividing average power by the pulse rate. A diode (PD-10.6, Boston Electronics, Brookline, MA) and oscilloscope (TDS 2002B, Tektronix, Beaverton, OR) were used to measure the pulse duration. Figure 6.2 provides a comparison of the temporal beam profiles.

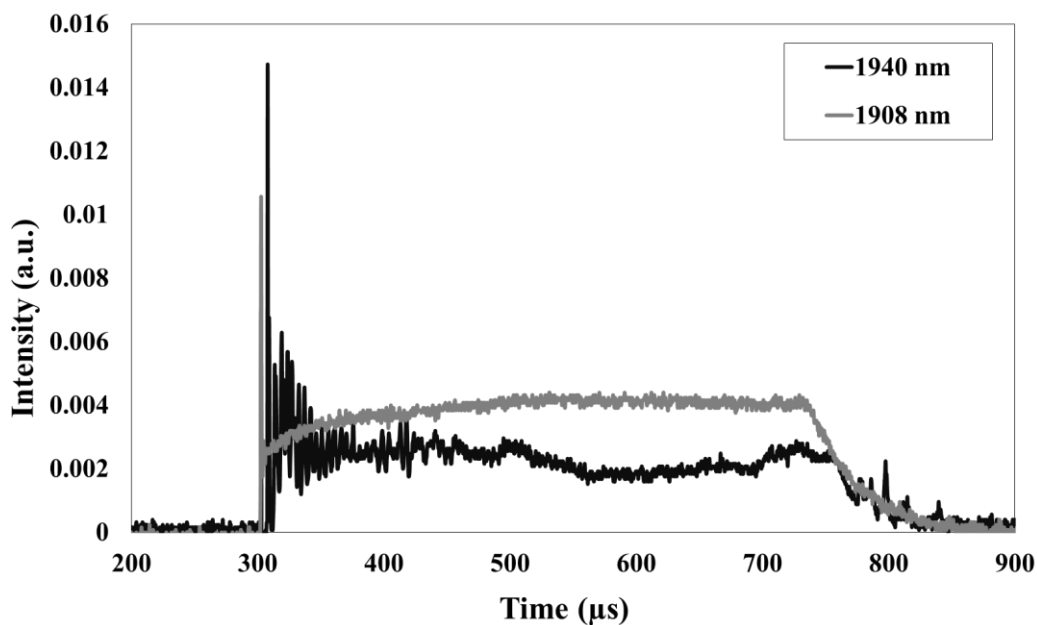


Figure 6.2. Temporal beam profiles of the two Thulium fiber lasers show a roughly similar shape, with each laser having an approximately 500 μs pulse length as measured from baseline to baseline.

6.2.2 Uric Acid Stone Samples

Uric acid (UA) stones, which account for ~ 15% of all stones encountered in the clinic [8], were used in this study due to the consistency in composition, shape, size, and color between the samples available. All stones were obtained from a stone analysis laboratory (Labcorp, Oklahoma City, OK). Stone samples were desiccated in an oven for 45 min at 100 °C and then weighed immediately using an analytic balance (Model AB54-S, Mettler-Toledo, Switzerland). Figure 6.3 provides representative images of UA stones used during the experiments.



Figure 6.3. Representative images of uric acid stone samples used during experiments. All stones were of similar shape, size (6-9 mm diameter) and mass (~ 260 mg).

6.2.3 Ablation Rate Measurements

The experimental set up for measuring stone ablation rates consisted of a large transparent container filled with saline and circulating irrigation using a water pump. Saline flow during experiments was used to clear stone debris for improved visibility, and to reduce potential thermal buildup near the ablation site. Each stone was placed on a 1 mm sieve, and irradiation time was recorded until all fragments fell through the sieve. The ablation rate was then calculated by dividing initial stone mass by total irradiation time. A 0.5 mm sieve was placed below the first sieve to collect a majority of the stone fragments. Fiber tips were prepared using an automated fiber optic polisher (Radian, Krelltech

Morganville, NJ) and fiber output power was measured before each experiment to confirm that any differences in ablation rate were not due to a potential change in laser power.

Figure 6.4 shows a diagram of the experimental setup.

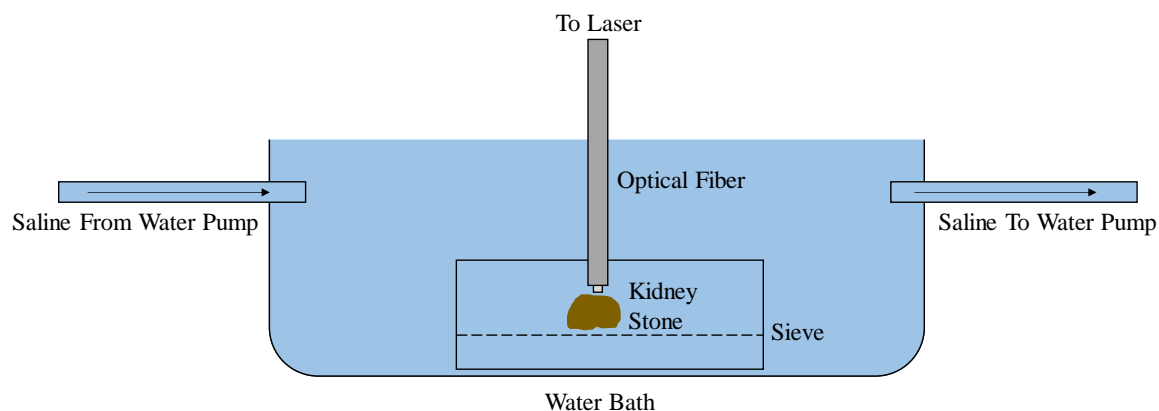


Figure 6.4. Diagram of experimental set up used to measure stone ablation times and then calculate stone ablation rates. The optical fiber was placed in contact mode with the stone for each experiment. A water pump was used for saline irrigation. In each experiment, the total time for all stone fragments to fall through the sieve was measured.

6.2.4 Ablation Threshold Measurements

To measure ablation threshold for each laser wavelength, a stone was held fixed and submerged in a saline bath. Laser pulse rate was kept constant at 50 Hz, and a total of 6000 pulses were delivered to each stone with the fiber in contact mode. Pulse energy was increased in small increments until mass loss could be measured using an analytical balance. Ablation threshold was determined by plotting mass loss (mg) vs radiant exposure (J/cm^2) with a linear fit and finding the x-intercept. Experimental procedures for measuring ablation threshold were based on previous studies [38][95].

6.2.5 Laser Induced Vapor Bubbles

A fast camera (Fastcam SA5, Photron, Tokyo, Japan) was used to image the laser induced vapor bubble produced from both lasers, at similar settings in a water medium.

The camera was operated at 105,000 frames per second ($\Delta t = 9.5 \mu\text{s}$) with a spatial

resolution of $\sim 15 \mu\text{m}$ per pixel. The bubble's diameter, length, and dynamics were measured, and analyzed using image processing with Matlab for each laser. The goals of the experiments were to compare size and dynamic changes laser induced vapor bubbles for both Thulium fiber laser wavelengths.

6.3 Results

Figure 6.5 shows the ablation rate results. For each group (1908 and 1940 nm), initial stone mass was $266 \pm 61 \text{ mg}$ vs. $262 \pm 54 \text{ mg}$, respectively. Ablation rates at 0.92 ± 0.18 , and $0.91 \pm 0.14 \text{ mg/s}$, respectively, with no statistical difference observed in ablation rates between the two laser wavelengths using similar laser parameters. The highest estimated error produced by the measuring equipment was 1.6 % of the measured value, additional error can be contributed to sample variability, and human error.

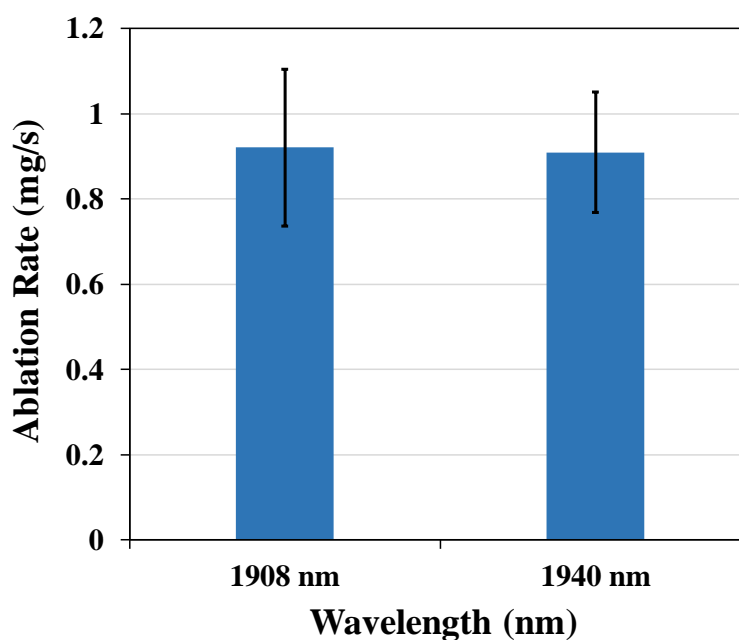


Figure 6.5. Ablation rates calculated from initial stone mass and total laser irradiation time for 1908 and 1940 nm TFLs ($n = 10$).

Figure 6.6 shows graphs of mass loss (mg) vs. radiant exposure (J/cm^2) for both the 1908 and 1940 nm wavelengths. The threshold values calculated from each graph

measured 8 ± 7 and 5 ± 13 J/cm² for the 1908 and 1940 nm wavelengths, respectively. The value of 8 ± 7 J/cm² for the 1908 nm wavelength is similar to the 6.5 J/cm² reported in previous literature for uric acid stones at 1908 nm wavelength [77]. The large error in the calculations is due to the compounding error created by each measurement. However, the data is sufficient to prove that the 1908 and 1940 nm lasers provide similar ablation thresholds as well as ablation rates.

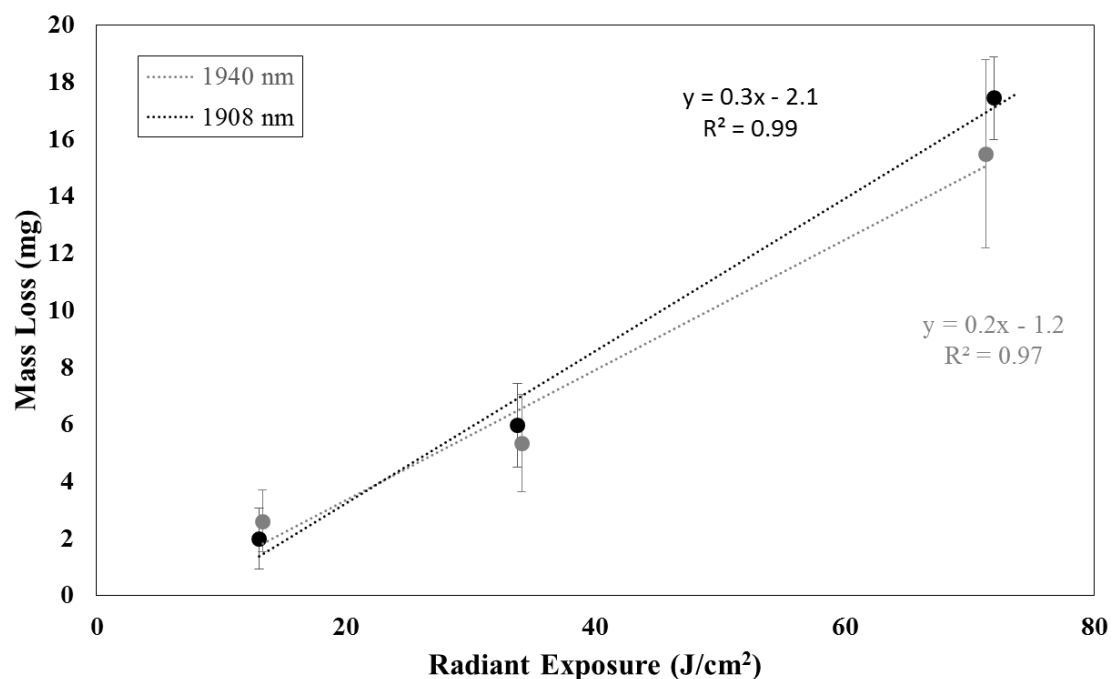


Figure 6.6. Mass loss vs. radiant exposure for (A) 1908 nm and (B) 1940 nm thulium fiber lasers. Threshold values of 8 ± 7 and 5 ± 13 J/cm² were calculated, respectively.

Figure 6.7 shows an image after the expansion of the first bubble for (A) 1940 nm laser, and (B) 1908 nm with the bubble lengths measuring 990 ± 30 μ m, and 690 ± 40 μ m, respectively. The 1940 nm laser produces a longer bubble, consistent with a smaller low temperature absorption coefficient in water.

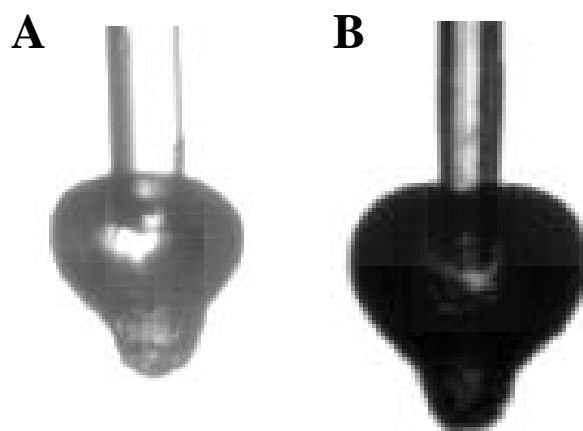


Figure 6.7. Image of first bubble expansion (A) 1908 and (B) 1940 nm at $\sim 120 \mu\text{s}$ into pulse duration for each laser.

Figure 6.8 displays bubble width dimensions as a function of time for both 1940 and 1908 nm laser wavelengths. The 1908 nm laser produced a smaller bubble width than 1940 nm wavelength, which is consistent with the theory of 1908 nm having a smaller optical penetration depth. The maximum width for 1908 and 1940 nm were $820 \pm 30 \mu\text{m}$, and $1150 \pm 40 \mu\text{m}$, respectively.

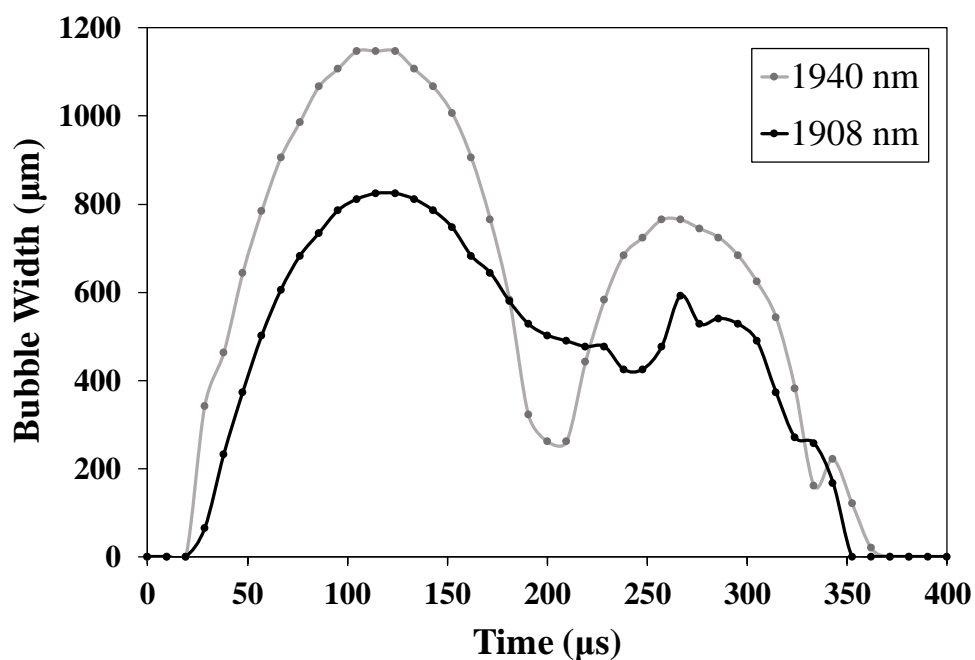


Figure 6.8. Bubble width dimensions for 1908 and 1940 nm laser wavelengths. Both bubbles produced two distinct expansions. However, the 1908 nm laser bubble did not fully collapse from first bubble, most likely due to a greater maximum length produced at end of laser pulse.

6.4 Discussion

The primary chromophore during laser lithotripsy is water. However, due to the multiple ablation mechanisms, the absorption coefficient is not the only indicator of ablation rate. Water only contributes to half of the ablation process through micro-explosions [20][81]. The other ablation mechanism is caused by direct absorption of light by the material, a higher water absorption coefficient would impede ablation through this mechanism by absorbing energy before it is able to reach the kidney stone [20]. The dynamics of the entire kidney stone ablation process is more complex and cannot be determined just from the water absorption coefficient of the water.

Similar ablation rates between the two IR wavelengths for similar laser parameters is not unprecedented. For example, our results between two TFL wavelengths is similar to previous reports comparing Thulium:YAG ($\lambda = 2010$ nm) and Holmium:YAG ($\lambda = 2120$ nm) lasers in soft tissue studies, in which an almost 2x higher water absorption coefficient of Thulium:YAG over Holmium:YAG (65 vs. 33 cm^{-1}) also produced no difference ablation rates [95].

A change in the water absorption by only an integer factor seems to have little effect on the ablation efficiency. Water content of the material is a better determinant of ablation efficiency. Previous studies between soft and hard tissues found a more dramatic change in the threshold ablation as a function of wavelength for soft tissue than hard tissue [92]. This is caused by the amount of water present in the tissue sample. Hard tissue (e.g. bone) typically has a water content of up to 30 %, compared with a much higher water content of 70-80% for soft tissue [96]. A higher content of the primary chromophore is a known contributor to increased ablation efficiency.

Due to lower water content in the stone and only a relatively small difference in the low temperature water absorption coefficient between the two wavelengths tested, there was no observable difference in the ablation threshold. Previous reports do show a difference in threshold ablation between the Ho:YAG (2120 nm) and TFL (1908 nm) [38]. However, there is a much larger difference in water absorption coefficients observed between Ho:YAG and TFL wavelengths at the high temperatures. The difference in water absorption coefficients between the 1908 and 1940 nm wavelengths are insufficient to observe a difference in the ablation threshold for uric acid stones.

Large errors were associated with the calculation of the ablation threshold of uric acid stones, due to multiple factors. The mass scale used had an error of ± 1 mg, and at the low radiant exposure values used, the mass loss was close to the error of the scale. This error compounded 15 times for each measurement created a large overall error for the ablation threshold calculation. However, even with the large errors, both wavelengths produced stone ablation thresholds sufficiently similar to determine that there was no large difference between lasers.

Vapor bubble dimensions and dynamics had small differences between the two wavelengths. Maximum width difference between 1908 and 1940 nm laser wavelengths may be explained by the smaller low temperature water absorption coefficient of 1940 nm laser, thus producing a longer bubble. This trend was also observed when comparing vapor bubbles created from 1908 nm wavelength TFL and 2120 nm wavelength of Ho:YAG [86]. Bubble dynamics did differ slightly as well which may be due in part to the chaotic nature of the bubble produced and small sample size ($n=1$) available for analysis. Such difference may also be attributable in part to the difficulty in producing the exact same laser

parameters for each laser. For example, laser pulse duration was directly dependent on pulse energy. However, differences in laser parameters were small and bubble size and dynamics between laser wavelengths were similar.

6.5 Conclusions

For similar laser parameters, Thulium fiber lasers operating at 1908 and 1940 nm wavelengths (closely matching a high and low temperature water absorption peak, respectively) did not produce a statistically significant difference in uric acid stone ablation thresholds or ablation rates. This result is attributed to the multiple ablation mechanisms present, including not only micro-explosions due to water absorption, but also direct absorption of the laser energy by the stone material, resulting in thermal decomposition of the stone material.

CHAPTER 7: High Power Holmium:YAG vs Thulium Fiber Laser for Dusting of Calcium Oxalate Kidney Stones

7.1 Introduction

7.1.1 Holmium laser lithotripsy

The Ho:YAG laser has been the standard laser for lithotripsy for over two decades. The Ho:YAG laser operates at an infrared wavelength of 2120 nm, and delivers energy through 200-1000 μm core, low-OH, silica optical fibers. Due to the flashlamp-pumped configuration, the laser operates in pulsed mode, typically with settings of 0.2-2.0 J pulse energy, 350-1500 μs pulse duration, pulse rates of 5-80 Hz, and average power up to 120 W. The recent availability of Ho:YAG lasers with high pulse rates (up to 80 Hz) allows more flexible operation but with a corresponding increase in size and cost of the laser.

Clinically, there are at least two common techniques used during laser lithotripsy, 'fragmentation' and 'dusting' ablation modes [22][23]. The 'fragmentation' mode is characterized by use of a high pulse energy (0.5 - 2.0 J) and low pulse rate (5 - 30 Hz). The stone is rapidly fractured into larger fragments. However, the 'fragmentation' operation mode also produces strong retropulsion effects, potentially resulting in migration of the remaining stone fragments from easily accessible areas such as the lower ureter into less accessible locations such as the kidney. This may impede the urologist's ability to efficiently ablate stones. In the past, only low power (≤ 20 W) and low pulse rate (≤ 30 Hz) Ho:YAG lasers were available, primarily limiting operation to a 'fragmentation' ablation mode.

The ‘dusting’ ablation mode utilizes low pulse energy (0.2 - 0.4 J) and high pulse rate (50-80 Hz) laser settings. The ablated debris is characterized as ‘dust’ (< 0.5 mm) and can be easily passed spontaneously by the patient. The ‘dusting’ mode results in lower stone retropulsion, but may not be able to ablate harder stones requiring a ‘fragmentation’ mode [24]. Currently, there is a clinical trend to move towards a dusting mode operation for laser lithotripsy [24][25]. This current ‘dusting’ trend is due to several factors. First, increase in stone ablation with an increase in pulse rate has been reported with the HoYAG laser [97]. Additional studies have shown that both a longer pulse duration, and lower pulse energy reduces stone retropulsion [26]. A major limitation for Ho:YAG laser lithotripsy arises from retropulsion and a need to limit its influence [98]. The current evidence shows a more favorable outcome for patients with a low pulse energy high pulse rate operation during laser lithotripsy [99].

7.1.2 Thulium fiber laser lithotripsy

The Thulium fiber laser (TFL) is currently being studied as a potential alternative to the Ho:YAG laser for treatment of kidney stones [28][29][30][31][32][33]. While the majority of reports have been based on pre-clinical, laboratory studies, the TFL has also shown promise in early clinical studies [34][35][36][37]. Electronic modulation enables the TFL to be operated at 5-500 mJ pulse energies, 100 μ s to 100’s of ms, and pulse rates of 1-2000 Hz, optimal for a ‘dusting’ mode technique. The TFL wavelength of 1940 nm also more closely matches a water absorption peak than the Ho:YAG wavelength of 2120 nm, for more efficient stone ablation [38]. The low pulse energy, high pulse rate ‘dusting’ mode of the TFL also reduces retropulsion and ablates stones faster than high pulse energy, low pulse rate ‘fragmentation mode’ operation of the Ho:YAG laser [44].

Previous laboratory studies comparing Holmium to TFL were either limited by the TFL in pulse rate or the Ho:YAG in average power [38][76]. Such technical limitations prevented direct comparison of both lasers using similar laser lithotripsy settings. However, the recent availability of both higher power TFL and Ho:YAG lasers now allows comparative studies with the ability to operate in ‘fragmentation’ and ‘dusting’ mode ablation settings. This experimental study compares stone ablation rates and stone fragment sizes between Ho:YAG and TFL when dusting stones using high average power settings.

7.2 Methods

7.2.1 Holmium:YAG Laser

The Ho:YAG laser (120H, Lumenis, Yokneam, Israel) used in the experiments was able to operate at an average power up to 120 W and pulse rate up to 80 Hz. For these experiments, three ‘dusting’ mode settings were used for comparison (Table 7.1). A 200- μm -core, silica optical fiber (SlimLine 200, Boston Scientific, Marlborough, MA) was used with both lasers. Two pulse duration laser settings were used in the study, short and long. The short and long pulse duration settings were approximately 250 μs and 1200 μs , respectively. Laser setting G1 utilized the short pulse setting, while the long pulse setting was used for G2, and G3. Figure 6.1 displays the temporal beam profile using the short pulse duration setting for the Ho:YAG laser.

Table 7.1. Summary of laser settings used for ‘dusting’ ablation mode in TFL and Ho:YAG laser lithotripsy experiments.

Setting	Pulse Energy (mJ)	Pulse Rate (Hz)	Average Power (W)	Pulse Duration	
				Ho:YAG	TFL
G1	200	50	10	Short (250 μs)	Short (500 μs)
G2	200	80	16	Long (1200 μs)	Short (500 μs)
G3	400	80	32	Long (1200 μs)	Long (1000 μs)

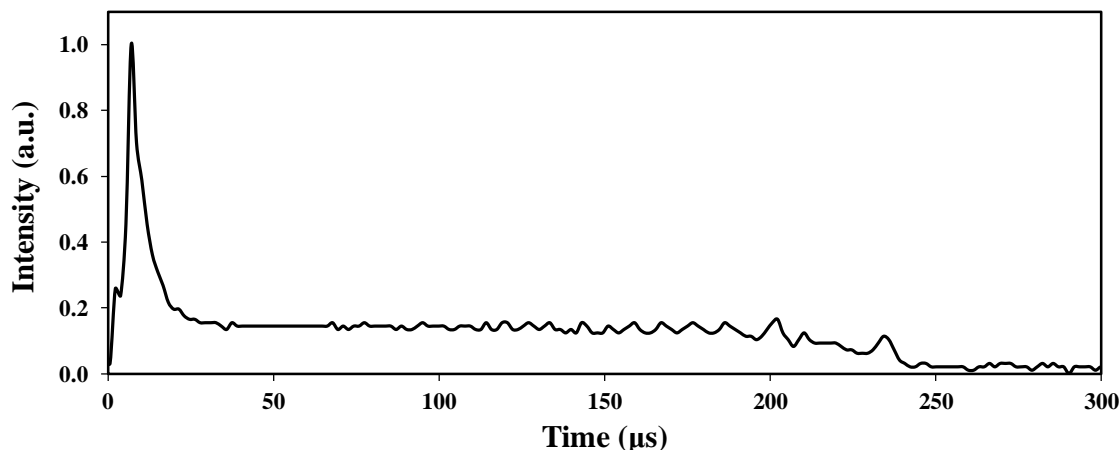


Figure 7.1. Temporal beam profile of short pulse Ho:YAG laser setting. The pulse duration measures $\sim 250 \mu\text{s}$. The pulse shape has a sharp initial spike followed by a more uniform profile.

7.2.2 Thulium fiber laser (TFL)

The Thulium fiber laser (IPG Medical, Marlborough, MA) used in these studies operated at a wavelength of 1940 nm. The TFL was capable of 50 W average power, 500 W peak power, and pulse rates up to 2000 Hz, allowing operation in either a ‘fragmentation’ or ‘dusting’ mode for ablation. For this study, TFL pulse duration settings were 500 μs , and 1000 μs for short and long pulse, respectively. For these studies G1, and G2 was operated in short pulse, while G3 was operated in long pulse (Figure 7.2).

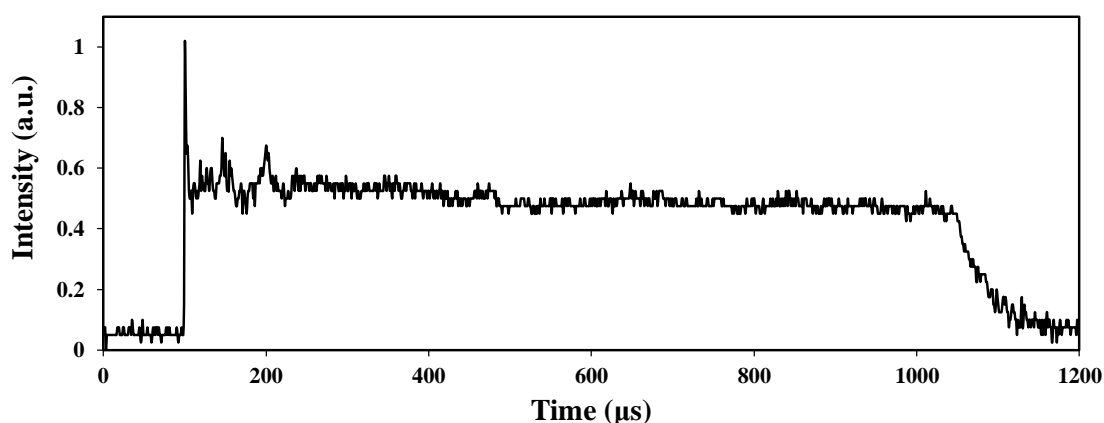


Figure 7.2. TFL temporal beam profiles for long pulse laser setting (G3), showing a more uniform profile than Ho:YAG laser.

7.2.3 Kidney Stone Samples

Calcium oxalate stone samples were obtained from a stone analysis laboratory (Dr. Michele Daudon, Tenon Hospital, Paris, France). Each stone was desiccated in an oven at 90 °C for 45 min and then weighed before experiments. A total of $n = 5$ stones were used for each setting, and 15 stones for each laser, with average initial stone mass ranging from 216 to 297 mg. Samples were chosen to maintain a similar average mass between each group.

7.2.4 Experimental Setup

An experimental setup consisting of 1 x 1 cm cuvette with 1 mm sieve was custom built. An inflow and outflow port connected to saline pumps (NE-9000, New Era Pump Systems, Farmingdale, NY) was used for saline irrigation, with thermocouples set at each port to monitor temperature as well (Figure 7.3). A separate 0.5 mm sieve was added to the 2.5 x 2.5 cm cuvette used as a saline reservoir and able to collect fragments that passed through the 1 mm sieve. All experiments were recorded with video for future analysis.

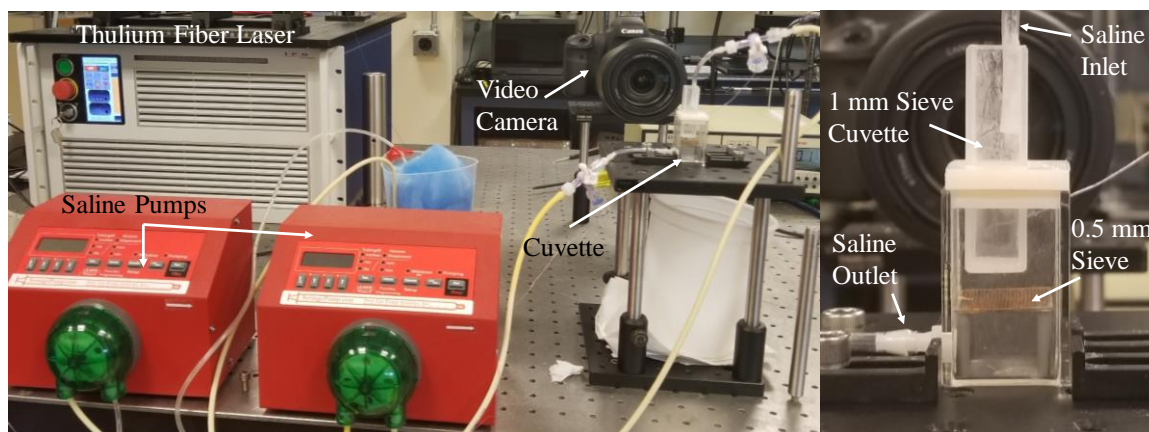


Figure 7.3. Photograph of experimental setup (left) with a magnified image of the ablation chamber (right).

Stone ablation times and fragment sizes were measured. Ablation rate (mg/s) was calculated by subtracting final stone mass from initial stone mass and dividing by time,

with continuous laser operation time limited to ≤ 5 min. To acquire the stone fragments after ablation, debris collected by the sieves in the experimental setup were filtered again using a 0.5 mm sieve. During this filtering process, the fragments were washed with water, placed in polystyrene conical tubes, and labeled. After all experiments were completed and all the fragments were collected, a pipette was used to remove excess water from the tubes. The fragments in the conical tubes were then desiccated in an oven at 80 °C for ~ 3 hrs. After desiccation, an analytical balance was used to weigh each stone fragment category for each sample. Weight percentage of stone fragments < 0.5 mm, between 0.5 - 1.0 mm, and > 1.0 mm were measured and compared.

A camera set up was used to stitch images of the stone fragments between 0.5 - 1.0 mm. The setup utilized two motorized linear actuators (LTA-HS, Newport, Irvine, CA), and a motion controller (ESP300, Newport, Irvine, CA) to move the fragment samples (Figure 4). A CMOS camera (DCC1645C-HQ, Thorlabs, Newton, NJ) with lens system captured images at preset coordinates. All images were put into an image stitching program (Adobe Photoshop CS6, San Jose, CA) to generate a larger image of the entire sample field. The stitched image was then analyzed using image processing software (Matlab R2017a, MathWorks, Natick, MA) and the fragment equivalent diameter was reported. 'Equivalent diameter' was calculated by equating the stone fragment area, calculated in pixels, to the area of a circle and then finding the diameter of the equivalent circle.

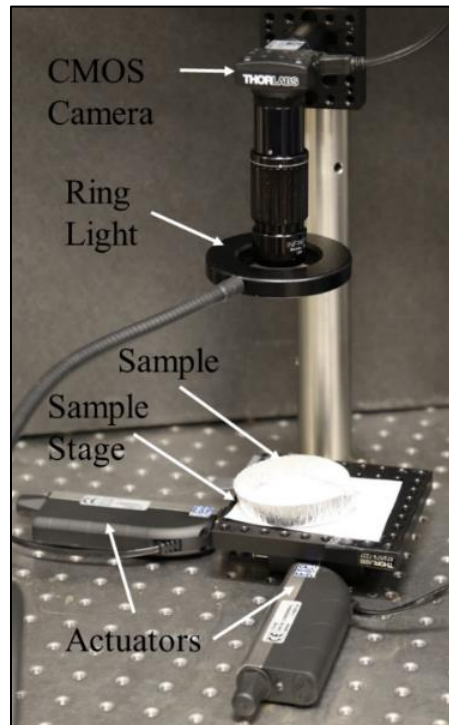


Figure 7.4. Image of stitching microscope setup. Actuators move the sample while the CMOS camera acquires images. The images are later stitched together to analyze the fragment size.

7.3 Results

For all three settings, TFL ablation rate was higher than for Ho:YAG laser (G1: 0.8 ± 0.2 vs. 0.3 ± 0.2 , $p = 0.01$; G2: 1.0 ± 0.4 vs. 0.6 ± 0.1 , $p = 0.04$; G3: 1.3 ± 0.9 vs. 0.7 ± 0.2 mg/s (Figure 7.5). For the 32 W (G3) setting, results were not statistically significant, due in part to strong stone retropulsion effects observed.

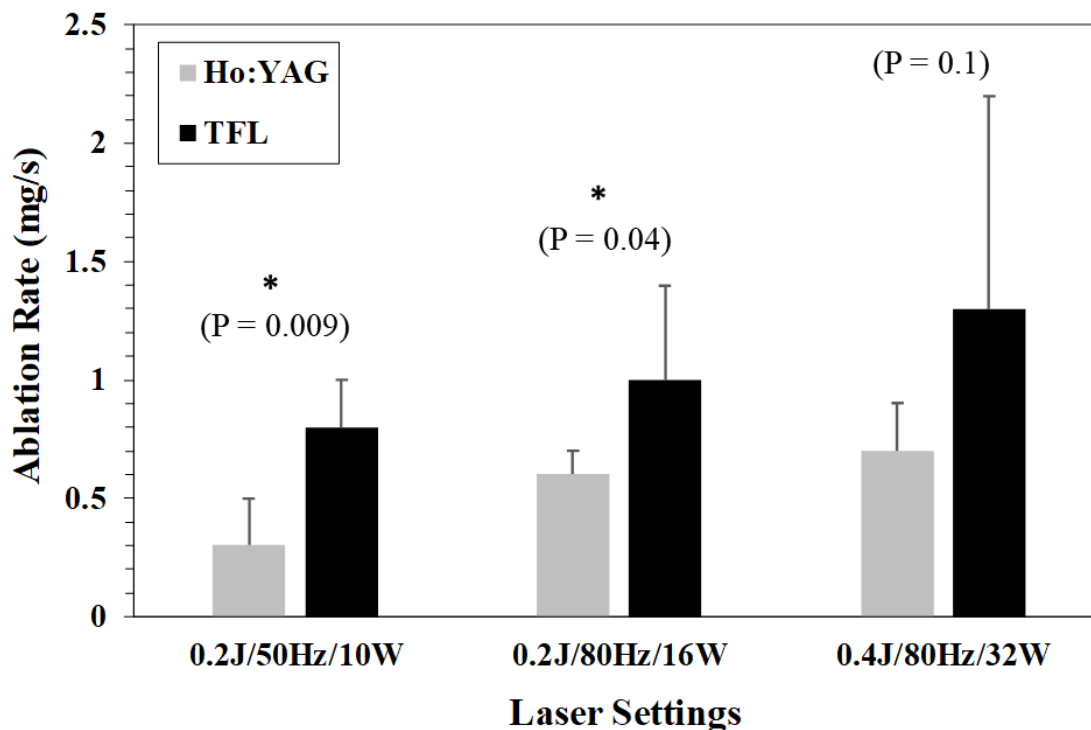


Figure 7.5. Ablation rate as a function of average power for TFL and Ho:YAG lasers. The P-value is labeled for each setting.

For all settings combined, 9 out of 15 (60%) stones treated with TFL were completely fragmented in ≤ 5 min, while only 1 out of 15 (7%) stones treated with Ho:YAG laser were completely fragmented in ≤ 5 min. The TFL also produced a greater percentage of smaller stone fragments (< 1 mm) than the Ho:YAG laser for each setting, although this was not statistically significant for all groups. Percentages of stone fragments < 0.5 mm were: G1: 73 ± 14 vs. 34 ± 16 ; G2: 78 ± 12 vs. 71 ± 8 ; G3: 86 ± 4 vs. 73 ± 10 %. Percentages of stone fragments between 0.5 - 1.0 mm were: G1: 4 ± 4 vs. 2 ± 1 ; G2: 11 ± 5 vs. 4 ± 2 ; G3: 14 ± 4 vs. 10 ± 7 %. Percentage of stone fragments > 1.0 mm were: G1: 23 ± 17 vs. 65 ± 17 ; G2: 11 ± 16 vs. 25 ± 9 ; G3: 0 vs. 17 ± 14 %. This data is summarized in Table 7.2.

Table 7.2. Percent (%) of stone fragments falling within each size range as a function of laser type and settings.

Stone Fragment Size:	< 0.5 mm		0.5 < x < 1 mm		> 1 mm	
Laser Setting:	TFL	Ho:YAG	TFL	Ho:YAG	TFL	Ho:YAG
G1: 0.2 J / 50 HZ / 10 W	73 ± 14	34 ± 16	4 ± 4	2 ± 1	23 ± 17	65 ± 16
G2: 0.2 J / 80 HZ / 16 W	78 ± 12	71 ± 8	11 ± 5	4 ± 2	11 ± 16	25 ± 9
G3: 0.4 J / 80 HZ / 32 W	86 ± 4	73 ± 10	14 ± 4	10 ± 7	0	17 ± 14

Histogram data of fragment size as a function of stone equivalent diameter is shown in Figure 7.6. There was no significance in the interpretation of the data. The actual fragment sizes changed between each experimental setting.

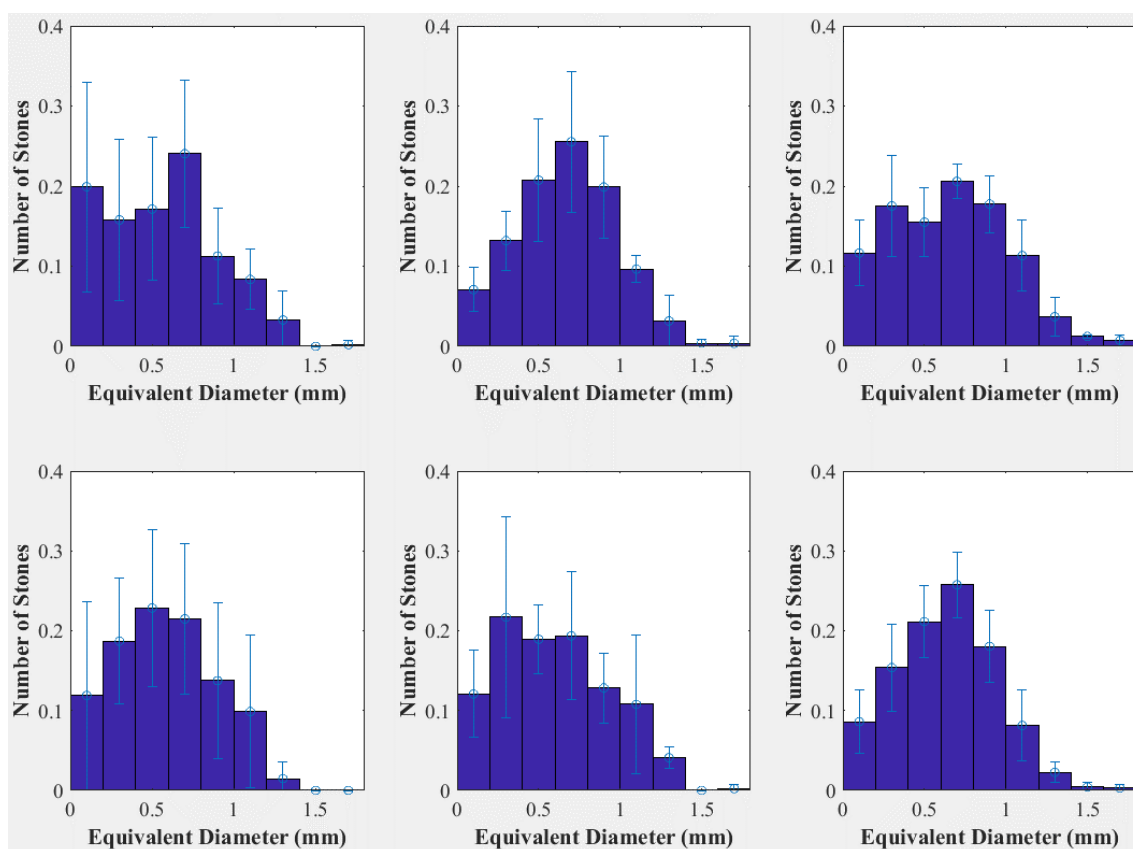


Figure 7.6. Histograms of fragment size normalized by total number of fragments, for TFL (top row) and Ho:YAG (bottom row), with laser settings (G1, G2, G3) in columns. A greater number of large fragments (> 1.5 mm) were observed at higher pulse energies.

While there was not a statistically significant trend in the histogram data, the total number of fragments varied as a function of laser type and settings (Table 7.3).

Table 7.3. Total number of stone fragments collected within size range of $0.2 < x < 2$ mm as a function of laser type and setting (n = 5 sample size).

Laser Settings	TFL	Ho:YAG
G1: 0.2 J / 50 Hz / 10 W	61 ± 23	26 ± 11
G2: 0.2 J / 80 Hz / 16 W	101 ± 5	71 ± 29
G3: 0.4 J / 80 Hz / 32 W	129 ± 34	111 ± 44

7.4 Discussion

The TFL completely ablated all stones in setting G3, and overall, a greater percentage of stones were completely ablated in < 5 min for TFL (60%) than for Ho:YAG laser (7%). This is most likely due to the decrease in retropulsion generated by the TFL [38]. Lower retropulsion allows more energy to be deposited to the stone rather than be delivered into the surrounding saline medium.

Settings G1 and G2 both show a statistically significant difference in ablation rate between TFL and Ho:YAG laser. Lower stone retropulsion allowed a more accurate measurement of the ablation rates with lower standard deviations. The higher TFL ablation rate as compared with the Ho:YAG laser, shows that a lower TFL stone ablation threshold translates into greater ablation. Previous studies reported a 4x lower TFL ablation threshold compared to Ho:YAG lasers [44]. In this study, the difference in ablation rate was not a factor of 4x, most likely due to direct absorption of the energy by the saline in front of the stone. This would result in a fraction of the laser energy being wasted heating the water, which would not contribute directly into stone ablation.

The setting G3 was not statistically different between TFL and Ho:YAG lasers. This was due in part to large error bars in the TFL group caused by a single data point. It was also noted that for setting G3 the time to ablate stones into small fragments was < 40 s, with the remaining time spent chasing small fragments, due to strong retropulsion effects. We speculate that the true ablation rate for setting G3 (32 W) is skewed and cannot be

accurately calculated due to the strong retropulsion observed. However, retropulsion is a clinically relevant influence on ablation rate and cannot be ignored. A better alternative is to look at fragment size, to try and determine if any lost stone (caused by retropulsion) could be potentially problematic for a patient.

Comparison of fragment percent mass between Ho:YAG and TFL shows that fragments < 0.5 mm were highest among all TFL laser settings. When analyzing fragments > 1 mm, Ho:YAG had highest percentage among all three group laser settings. This demonstrates that for comparison of ‘dusting’ mode ablation laser settings, the TFL produces more dust (< 0.5 mm) than Ho:YAG laser. This result is logical due to the increase in water absorption at TFL wavelength. Stronger absorption causes more efficient fracturing of the stone from ‘micro-explosions’ caused by the water [81].

A previous dusting study by another research group reported that a high Ho:YAG laser pulse energy generated more fragments < 1 mm in diameter [23]. In that study, average power was kept constant and laser energy and pulse rate were varied. An increase in dust with an increase in pulse energy was observed. However, they did not report mass of the other fragment sizes, $1 < x < 3$ mm, and > 3 mm, and only Bego stone phantoms were used.

When analyzing fragment percent mass of Ho:YAG data, there was apparent error caused by handling of the sample fragments after the experiments. The Ho:YAG arm of the experiments was performed offsite with limited resources. Recovering the $0.5 < x < 1$ mm fragments may not have been conducted as accurately as necessary. This is the primary reason for a lower percentage of total fragments collected when comparing Ho:YAG to TFL (Table 7.3). During transport of the samples, > 1 mm fragments may have been jostled

inside of the large container and not recovered during the measurement phase. These errors carried over into the analysis of the histogram data.

The histogram data did not show any observable differences between lasers or laser settings. Fragments from $0.5 < x < 1$ mm diameter were the only samples analyzed. There are several potential points of error from the setup. First, saline may not have been completely washed away during recovery of stone fragments, resulting in residual sodium growth deposits in the samples after drying, and most likely the source of fragments < 0.5 mm. Also, some samples were attached to the side of conical tubes after drying and had to be physically removed, which could have further fractured the fragments. Another source of error was the resolution of the imaging setup, calculated to be $\sim 11 \mu\text{m}/\text{pixel}$. This resolution may have been insufficient to accurately measure fragment size or to distinguish between two larger fragments situated close together. In future studies, fragments must be thoroughly washed before being placed in a conical tube and a desiccation process utilizing a vacuum, rather than heat, would be preferable. This will help reduce sodium deposits and need for physical removal of fragments after desiccation. Also, an increase in camera magnification and number of images taken per sample should reduce error.

Alternatively, using laser diffraction methods to calculate fragment size could eliminate error altogether. Previous studies utilizing laser diffraction to analyze stone fragments produced by a TFL in ‘dusting’ ablation mode showed low average diameters, on the order of 100’s of micrometers [100]. However, there was only an $n = 4$ sample size and the $0.1 \text{ J} / 50 \text{ Hz}$ laser setting was only compared to a CW setting. A CW laser setting is not clinically relevant due to stone retropulsion, patient safety, and thermal build up. The data

does give insight into the average size of debris from TFL lithotripsy, but little statistical data is presented for further analysis or comparison to this study.

During the fragment analysis, the number of total stone fragments for each laser setting showed a statistically significant trend. As the laser average power was increased, a noticeable increase in total stone fragments from 0.2 to 2 mm was reported (Table 6.3). This can be explained by the increase in average power and pulse energy, which also increases ablation rate [44][101].

Overall, the data in this study suggests that the TFL produces smaller fragments, and ablates stones more rapidly than the Ho:YAG laser, for similar settings. These properties make the TFL laser an attractive alternative to Ho:YAG for laser lithotripsy. Several clinical studies have recently been conducted using the TFL for laser lithotripsy [34][35][36][37].

7.5 Conclusions

The Thulium fiber laser produced higher stone ablation rates and smaller stone fragments than the Holmium:YAG laser. Further, clinical studies to evaluate the TFL as an alternative laser lithotripter are warranted.

CHAPTER 8: Conclusion

Kidney stone disease is responsible for 5.3 billion dollars in medical costs annually [3]. There is a need for an efficient and effective treatment method. Limitations of Ho:YAG lithotripsy, and the advantages of TFL lithotripsy have been shown throughout this document. The experiments provide evidence of the feasibility for the transition of TFL into the clinic for laser lithotripsy.

TFL lithotripsy is able to operate in a ‘dusting’ ablation mode at clinically relevant ablation rates. This was done by pulsing the laser up to 500 Hz with a 35 mJ pulse energy. It was also shown that kidney stone ablation rate increases linearly as a function of pulse rate. However, not comparison with the Ho:YAG laser was made directly.

Operation times were compared between the TFL and Ho:YAG lasers, using an in vitro ureter model, with the stone allowed to move freely. Operative time and temperature data near the ablation site was tested to confirm safe operating parameters. TFL operation time was found to be shorter than for the Ho:YAG laser. Peak temperature in the saline environment increased with TFL pulse rate by ~ 6 °C, but was determined safe through Arrhenius integral calculations. The shorter operation time was a product of a decrease in retropulsion from the TFL.

A primary cause of retropulsion is the expansion and collapse of the laser induced vapor bubble representative of near-IR radiation in a fluid environment. The laser vapor bubble also creates a modality for removal of weakened/ablated material, increase ablation efficiency. It was found that the TFL operating at lower peak power (70 W) produces a stream of bubbles expanding and collapsing during the laser pulse. The dynamic differed

than typical Ho:YAG laser bubble dynamics, which produce a single bubble expansion and collapse. It was determined that the TFL vapor bubble chain collapses almost 90 degrees out of phase with itself along the axial direction of the fiber, causing destructive interference of any pressure wave that was produced.

Laser lithotripsy utilizes a photothermal ablation mechanism. During irradiation in both water and air environments SEM images were used to qualify the amount of ablation occurring from direct absorption of the material, or through ‘micro-explosions’ caused from absorption by water in the stone. The effects of both direct thermal ablation (e.g. melting and decomposition) as well as micro-explosions (e.g. cracks and fractures) were observed from irradiation in a water environment. Showing that both long pulse, infrared ablation processes depend on multiple factors. Furthermore, both UltraCal30 and BegoStone artificial stone phantoms, commonly used in laser lithotripsy laboratory studies, were found to be un-representative of real kidney stone samples for studying the ablation mechanism.

A comparison between 1908 nm and 1940 nm emitting TFL lasers was made, due to the approximate 20 % difference in low temperature water absorption coefficient. The ablation rate, ablation threshold, and laser vapor bubbles were compared using the same laser parameters. It was found that both the 1908 nm and 1940 nm emitting TFL lasers do not produce a statistically relevant difference among all three categories. This result is attributed to the multiple ablation mechanisms present, including not only micro-explosions due to water absorption, but also direct absorption of the laser energy by the stone material, resulting in thermal decomposition of the stone material.

A second comparison between Ho:YAG and TFL was conducted with both lasers operating with the same laser parameters. The ablation rate, and information on stone debris size was analyzed. It was found that the TFL produced higher stone ablation rates and smaller stone fragments than the Ho:YAG laser.

Overall, the experiments provided show that the Thulium Fiber Laser is a feasible alternative to Ho:YAG laser for lithotripsy.

REFERENCES

- [1] M. S. Pearle, E. A. Calhoun, G. C. Curhan, "Urologic Diseases in America Project: Urolithiasis," *J. Urol.* 173(3), 848-857 (2005).
- [2] T. Vos, et al, "Global, regional, and national incidence, prevalence, and years lived with disability for 301 acute and chronic diseases and injuries in 188 countries, 1990-2013: a systematic analysis for the Global Burden of Disease Study 2013," *Lancet* 386(9995), 743-800 (2015).
- [3] C. S. Saigal, G. Joyce, A. R. Timilsina, "Direct and Indirect Costs of Nephrolithiasis in an Employed Population: Opportunity for Disease Management," *Kidney Int.* 68(4), 1808-1814 (2005).
- [4] D. T. Oberlin, A. S. Flum, L. Bachrach, R. S. Matulewicz, and S. C. Flurry, "Contemporary surgical trends in the management of upper tract calculi," *J. Urol.* 193(3), 880-884 (2015).
- [5] C. D. Scales, A. C. Smith, J. M. Hanley, C. S. Saigal, "Prevalence of Kidney Stones in the United States," *Eur. Urol.* 62(1), 160-165 (2012).
- [6] T. H. Brikowski, Y. Lotan, M. S. Pearle, "Climate-Related Increase in the Prevalence of Urolithiasis in the United States," *Proc. Natl. Acad. Sci.* 105(28), 9841-9846 (2008).
- [7] O. W. Moe, "Kidney Stones: Pathophysiology and Medical Management," *Lancet.* 367, 333-344 (2006).
- [8] D. M. Wilson, "Clinical and laboratory approaches for evaluation of nephrolithiasis," *J. Urol.* 141 (3.2), 770-774 (1989).
- [9] National Kidney and Urologic Diseases Information Clearinghouse (NKUDIC). (n.d.). (NIH.gov) Retrieved January 21, 2015.
- [10] F. L. Coe, A. Evan, and E. Worcester, "Kidney stone disease," *J. Clin. Invest.* 115, 2598-2608 (2005).
- [11] A. J. Hendrix, W. E. Strijbos, D. W. de Knijff, J. J. Kums, W. H. Doesburg, and W. A. Lemmens, "Treatment for extended-mid and distal ureteral stones: SWL or ureteroscopy? Results of a multicenter trial," *J. Endourol.* 13(10), 727-733 (1999).
- [12] K. Kijvikai, G. E. Haleblan, G. M. Preminger, and J. de la Rosette, "Shock wave lithotripsy or ureteroscopy for the management of proximal ureteral calculi: an old discussion revisited," *J. Urol.* 178 (4 Pt 1), 1157-1163 (2007).
- [13] C. D. Scales, J. C. Lai, A. W. Dick, J. M. Hanley, J. van Meijgaard, C. M. Setodji, and C. S. Saigal, "Comparative effectiveness of shock wave lithotripsy and ureteroscopy for treating patients with kidney stones," *JAMA Surg.* 149, 648-653 (2014).
- [14] M. Ordon, D. Urbach, M. Mamdani, R. Saskin, J. J. D'AHoney, K. T. Pace, "The Surgical Management of Kidney Stone Disease: Population Based Time Series Analysis," *J. Urol.* 192, 1450-1456 (2014).

- [15] K. F. Chan, G. J. Vassar, T. J. Pfefer, J. M. Teichman, R. D. Glickman, S. T. Weintraub, and A. J. Welch, "Holmium:YAG laser lithotripsy: a dominant photothermal ablative mechanism with chemical decomposition of urinary calculi," *Lasers Surg. Med.* 25(1), 22-37 (1999).
- [16] A. Roggan, U. Bindig, W. Wäsche, and F. Zgoda, "Action mechanisms of laser radiation in biological tissues," *Applied Laser Medicine*. Ch. I-3.1. Pg. 87. ISBN:3-540-67005-X (2003).
- [17] I. Itzkan, D. Albagli, M. L. Dark, L.T. Perelman, C. von Rosenberg, M. S. Feld, "The thermoelastic basis of short pulsed laser ablation of biological tissue," *Proc. Natl. Acad. Sci. USA.* 92, 1960-1964 (1995).
- [18] M. Frenz, "IR-Lasers in Medicine: Basics and Applications [post-doctoral thesis]," Bern: Universität Bern, (1998).
- [19] E.D. Jansen, T. Asshauer, M. Frenz, M. Motamedi, G. Delacretaz, A.J. Welch, "Effect of pulse duration on bubble formation and laser induced pressure waves during holmium laser ablation," *Lasers Surg. Med.* 18, 278-293 (1996).
- [20] K. F. Chan, T.J. Pfefer, J.M.H Teichman, and A.J. Welch, "A perspective on laser lithoripsy: the fragmentation process," *J Endourol*, 15(3), 257-273 (2001).
- [21] O. Lindau, and W. Lauterborn, "Cinematographic observation of the collapse and rebound of a laser-produced cavitation bubble near a wall," *J. Fluid Mech*, 479, 327-348 (2003).
- [22] A. P. Patel and B. E. Knudsen, "Optimizing use of the Holmium:YAG laser for surgical management of urinary lithiasis," *Curr. Urol. Rep.* 15, 397 (2014).
- [23] M. J. Bader, T. Pongratz, W. Khoder, C. G. Stief, T. Herrmann, U. Nagele, and R. Sroka, "Impact of pulse duration on Ho:YAG laser lithotripsy: fragmentation and dusting performance," *World J. Urol.* 33, 471-477 (2015).
- [24] J. Tracey, G. Gagin, D. Morhardt, J. Hollingsworth, and K. R. Ghani, "Ureteroscopic high-frequency dusting utilizing a 120-W holmium laser," *J. Endourol.* 32, 290-295 (2018).
- [25] C. A. Dauw, L. Simeon, A. F. Alruwaily, F. Sanguedolce, J. M. Hollingsworth, W. W. Roberts, G. J. Faerber, J. S. Wolf, and K. R. Ghani, "Contemporary practice patterns of flexible ureteroscopy for treating renal stones: results of a worldwide survey," *J. Endourol.* 29, 1221-1230 (2015).
- [26] D. S. Finley, J. Petersen, C. Abdelsehid, M. Ahlering, D. Chou, J. Borin, L. Eichel, E. McDougall, and R. V. Clayman, "Effect of Holmium:YAG laser pulse width on lithotripsy retropulsion in vitro," *J of Endourol*, 19(8), 1041-1044, (2005).
- [27] B. E. Knudsen, R. D. Glickman, K. J. Stallman, S. Maswadi, B. H. Chew, D. T. Beiko, J. D. Denstedt, and J. M. H. Teichman, "Performance and safety of Holmium:YAG laser optical fibers," *J. Endourol.* 19(9), 1092-1097 (2005).
- [28] N. M. Fried, "Thulium fiber laser lithotripsy: An in vitro analysis of stone fragmentation using a modulated 110-watt Thulium fiber laser at 1.94 μm ," *Lasers Surg. Med.* 37(1), 53-58 (2005).

- [29] V. Zamyatina, V. Minaev, I. Yaroslavsky, A. Koyalenko, A. Vinarov, and G. Altshuler, "Super pulse thulium fiber laser for lithotripsy," *Lasers Surg. Med.* 48, Abstract #28 (2016).
- [30] P. Glybochko, G. Alshuler, A. Vinarov, L. Rapoport, M. Enkeev, N. Grigoriev, D. Enikeev, N. Sorokin, A. Dymov, R. Sukhanov, M. Taratkin, and V. Zamyatina, "Comparison between the possibilities of holmium and thulium laser in lithotripsy in vitro," *Eur. Urol. Suppl.* 16, Abstract #226 (2017).
- [31] A. Dymov, P. Glybochko, Y. Alyaev, A. Vinarov, G. Altshuler, V. Zamyatina, N. Sorokin, D. Enikeev, V. Lekarev, A. Proskura, and A. Koshkarev, "Thulium lithotripsy: from experiment to clinical practice," *J. Urol.* 197, Abstract #V11-11 (2017).
- [32] A. Gross, B. Becker, M. Taratkin, D. Enikeev, L. Rapoport, and C. Netsch, "Wavelength and pulse shape effects on stone fragmentation of laser lithotripters," *J. Urol.* 199(4S), e293, Abstract # MP24-10 (2018).
- [33] I. Yaroslavsky, V. Vinnichenko, T. McNeill, A. Novoselteva, I. Perchuk, A. Vybornov, G. Altshuler, and V. Gapontsev, "Optimization of a novel Tm fiber laser lithotripter in terms of stone ablation efficiency and retropulsion reduction," *Proc. SPIE* 104680H, 1-9 (2018).
- [34] A. G. Martov, D. V. Ergakov, M. A. Guseinov, A. S. Andronov, S. V. Dutov, V. A. Vinnichenko, and A. A. Kovalenko, "Initial experience in clinical application of thulium laser contact lithotripsy for transurethral treatment of urolithiasis," *Urologiia* Mar (1), 112-120 (2018).
- [35] D. Ergakov, A. G. Martov, and M. Guseynov, "The comparative clinical study of Ho:YAG and Superpulse Tm fiber laser lithotripters," 17(2), e1391, Abstract # 991 (2018).
- [36] O. Traxer, L. Rapoport, D. Tsarichenko, A. Dymov, D. Enikeev, N. Sorokin, S. Ali, G. Akopyan, D. Korolev, A. Proskura, V. Lekarev, and R. Klimov, "First clinical study on superpulse thulium fiber laser lithotripsy," *J. Urol.* 199(4S), e321, Abstract # V03-02 (2018).
- [37] A. Dymov, P. Glybochko, Y. Alyaev, A. Vinarov, G. Altshuler, V. Zamyatina, N. Sorokin, D. Enikeev, V. Lekarev, A. Proskura, and A. Koshkarev, "Thulium lithotripsy: from experiment to clinical practice," *J. Urol.* 197(4S), Abstract # V11-11 (2018).
- [38] R. L. Blackmon, P. B. Irby, and N. M. Fried, "Comparison of Holmium:YAG and Thulium fiber laser lithotripsy: ablation thresholds, ablation rates, and retropulsion effects," *J. Biomed. Opt.* 16(7), 071403 (2011).
- [39] E. D. Jansen, T. G. van Leeuwen, M. Motamedi, C. Borst, and A. J. Welch, "Temperature dependence of the absorption coefficient of water for midinfrared laser radiation," *Lasers Surg. Med.* 14(3), 258-268 (1994).
- [40] G. M. Hale and M. R. Querry, "Optical constants of water in the 200-nm to 200-mm wavelength region," *Appl. Opt.* 12(3), 555-563 (1973).

- [41] B. I. Lange, T. Brendel, and G. Huttman, "Temperature dependence of light absorption in water at holmium and thulium laser wavelengths," *Appl. Opt.* 41(27), 5797-5803 (2002).
- [42] R. L. Blackmon, T. C. Hutchens, L. A. Hardy, C. R. Wilson, P. B. Irby, N. M. Fried, "Thulium fiber laser ablation of kidney stones using a 50- μ m-core silica optical fiber," *Opt Eng.* 54:011004 (2015).
- [43] C. R. Wilson, T. C. Hutchens, L. A. Hardy, P. B. Irby, N. M. Fried, "A miniaturized, 1.9 french integrated optical fiber and stone basket for use in thulium fiber laser lithotripsy," *J. Endourol.* 29(10), 1110-4 (2015).
- [44] L. A. Hardy, C. R. Wilson, P. B. Irby, and N. M. Fried, "Rapid Thulium fiber laser lithotripsy at pulse rates up to 500 Hz using a stone basket," *IEEE J. Sel. Top. Quantum Electron.* 20(5), 0902604 (2014).
- [45] C. R. Wilson, L. A. Hardy, P. B. Irby, N. M. Fried, "Collateral damage to the ureter and nitinol stone baskets during Thulium fiber laser lithotripsy," *Laser Surg. Med.* 47(5), 403-410 (2015).
- [46] M. D. White, M. E. Moran, C. J. Calvano, A. Borhan-Manesh, and B. A. Mehlhaff, "Evaluation of retropulsion caused by Holmium:YAG laser with various power settings and fibers," *J. Endourol.* 12(2), 183-186 (1998).
- [47] H. Lee, T. R. Ryan, J. M. H. Teichman, J. Kim, B. Choi, N. V. Arakeri, and A. J. Welch, "Stone retropulsion during Holmium:YAG Lithotripsy," *J. Urol.* 169(3), 881-885 (2003).
- [48] C. G. Marguet, J. C. Sung, W. P. Springhart, J. O. L'Esperance, S. Zhou, P. Zhong, D. M. Albala, and G. M. Preminger, "In vitro comparison of stone retropulsion and fragmentation of the frequency doubled, double pulse Nd:YAG laser and the Holmium:YAG laser," *J. Urol.* 173(5), 1797-1800 (2005).
- [49] H. W. Kang, H. Lee, J. M. Teichman, J. Oh, J. Kim, and A. J. Welch, "Dependence of calculus retropulsion on pulse duration during Ho:YAG laser lithotripsy," *Lasers Surg. Med.* 38(8), 762-772 (2006).
- [50] P. Kalra, N. B. Le, and D. Bagley, "Effect of pulse width on object movement in vitro using holmium:YAG laser," *J. Endourol.* 21(2), 228-231 (2007).
- [51] J. Sea, L. M. Jonat, B. H. Chew, J. Qiu, B. Wang, J. Hoopman, T. Milner, and J. M. H. Teichman, "Optimal power settings for Holmium:YAG lithotripsy," *J. Urol.* 187, 914-919 (2012).
- [52] O. M. Elashry and A. M. Tawfik, "Preventing stone retropulsion during intracorporeal lithotripsy," *Nat. Rev. Urol.* 9(12), 691-698 (2012).
- [53] R. L. Blackmon, P. B. Irby, and N. M. Fried, "Holmium:YAG laser lithotripsy at high pulse energies versus Thulium fiber laser lithotripsy at high pulse rates," *J. Endourol.* 24(12), #72, 2136-2137, (2010).
- [54] S. Thomsen and J. A. Pierce, "Thermal damage and rate processes in biologic tissues," (Chapter 13) in *Optical-Thermal Response of Laser Irradiated Tissue*, 2nd Ed., Springer: Heidelberg, Germany (2011).

- [55] X. He, S. McGee, J. E. Coad, F. Schmidlin, P. A. Iaizzo, D. J. Swanlund, S. Kluge, E. Rudie E, and J. C. Bischof, "Investigation of the thermal and tissue injury behavior in microwave thermal therapy using a porcine kidney model," *Int. J. Hyperthermia*, 20(6), 567–593 (2004).
- [56] R. Agah, J. A. Pearce, A. J. Welch, and M. Motamedi, "Rate process model for arterial tissue thermal damage: implications on vessel coagulation," *Lasers Surg. Med.*, 15(2), 176-184 (1994).
- [57] W. R. Molina, I. N. Silva, R. D. da Silva, D. Gustafson, D. Sehr, and F. J. Kim, "Influence of saline on temperature profile of laser lithotripsy activation," *J. Endourol.* [Epub] (2014).
- [58] D. A. Wollin, E. C. Carlos, W. R. Tom, W. N. Simmons, G. M. Preminger, M. E. Lipkin, "Effect of Laser Settings and Irrigation Rates on Ureteral Temperature During Holmium Laser Lithotripsy, an In Vitro Model," *J. Endourol.* 32(1), 59-63 (2018).
- [59] K. Hendlin, D. Weiland, and M. Monga, "Impact of irrigation systems on stone migration," *J. Endourol.* 22(3) (2008).
- [60] T. Bach, B. Geavlete, T. R. W. Herrmann, and A. J. Gross, "Working tools in flexible ureterorenoscopy – influence on flow and deflection: What does matter?" *J. Endourol.* 22(8), 1639-1643 (2008).
- [61] R. W. Santa-Cruz, R. J. Leveillee, and A. Krongrad, "Ex vivo comparison of four lithotripters commonly used in the ureter: what does it take to perforate?" *J. Endourol.* 12(5), 417-422 (1998).
- [62] A. Vogel and V. Venugopalan, "Mechanisms of pulsed laser ablation of biological tissues," *Chem. Rev.* 103(2), 577-644 (2003).
- [63] H. Loertscher, W. Shi, and W. Grundfest, "Tissue ablation through water with Erbium:YAG lasers," *IEEE Trans. Biomed. Eng.* 39(1), 86-88 (1992).
- [64] M. Frenz, H. Pratisto, F. Konz, E. D. Jansen, A. J. Welch, and H. P. Weber, "Comparison of the effects of absorption coefficient and pulse duration of 2.12- μm and 2.79- μm radiation on laser ablation of tissue," *IEEE J. Sel. Top. Quantum Electron.* 32(12), 2025-2035 (1996).
- [65] H. Pratisto, M. Frenz, M. Ith, H. J. Altermatt, E. D. Jansen, and H. P. Weber, "Combination of fiber-guided pulsed erbium and holmium laser radiation for tissue ablation under water," *Appl. Opt.* 35(19), 3328-3337 (1996).
- [66] M. Frenz, F. Konz, H. Pratisto, H. P. Weber, A. S. Silenok, and V. I. Konov, "Starting mechanisms and dynamics of bubble formation induced by a Ho:Yttrium aluminum garnet laser in water," *J. Appl. Phys.* 84(11), 5905-5912 (1998).
- [67] O. Fohn, H. S. Pratisto, F. Konz, M. Ith, J. Altermatt, M. Frenz, and H. P. Weber, "Side-firing fiber device for underwater tissue ablation with Ho:YAG and Er:YAG laser radiation," *J. Biomed. Opt.* 3(1), 112-122 (1998).

- [68] P. Zhong, H. L. Tong, F. H. Cocks, M. S. Pearle, and G. M. Preminger, "Transient cavitation and acoustic emission produced by different laser lithotripters," *J. Endourol.* 12(4), 371-374 (1998).
- [69] S. Griffin, "Fiber optics for destroying kidney stones," *Biophoton. Int.* 11(4), 44-47 (2004).
- [70] N. J. Scott, C. M. Cilip, and N. M. Fried, "Thulium fiber laser ablation of urinary stones through small-core optical fibers," *IEEE J. Sel. Top. Quantum Electron.* 15, 435-440 (2009).
- [71] R. L. Blackmon, P. B. Irby, and N. M. Fried, "Thulium fiber laser lithotripsy using tapered fibers," *Lasers Surg. Med.* 42(1), 45-50 (2010).
- [72] T. Lu, Q. Xiao, D. Xia, K. Ruan, and Z. Li, "Cavitation effect of holmium laser pulse applied to ablation of hard tissue underwater," *J. Biomed. Opt.* 15(4), 048002 (2010).
- [73] T. Asshauer, K. Rink, and G. Delacretaz, "Acoustic transient generation by holmium-laser-induced cavitation bubbles," *J. Appl. Phys.* 76(9), 5007-5013 (1994).
- [74] J. W. Dushinski and J. E. Lingeman, "High-speed photographic evaluation of holmium laser," *J. Endourol.* 12(2), 177-181 (1998).
- [75] T. Lu and Z. Li, "Underwater holmium-laser-pulse-induced complete cavitation bubble movements and acoustic transients," *Chinese Science Bulletin* 56(12), 1226-1229 (2011).
- [76] L. A. Hardy, C. R. Wilson, P. B. Irby, and N. M. Fried, "Thulium fiber laser lithotripsy in an in vitro ureter model," *J. Biomed. Opt.* 19(12), 128001 (2014).
- [77] R. L. Blackmon, "Thulium Fiber Laser Lithotripsy," Ph.D. Thesis, Optical Science and Engineering, United States of America, University of North Carolina at Charlotte (2013).
- [78] R. L. Blackmon, "Holmium:YAG ($\lambda = 2,120$ nm) Versus Thulium Fiber ($\lambda = 1,908$ nm) Laser Lithotripsy," *LSM.* 42(3), 232-236 (2010).
- [79] M. E. Mayo, "Interaction of laser radiation with urinary calculi," Ph.D. Thesis, Department of Applied Science, Security and Resilience, United Kingdom, Cranfield University (2009).
- [80] G. Motley, N. Dalrymple, C. Keesling, J. Fischer, W. Harmon, "Hounsfield unit density in the determination of urinary stone composition," *Urology* 58(2), 170-173 (2001).
- [81] B. Majaron, P. Plestenjak, M. Lukac, "Thermo-mechanical laser ablation of soft biological tissue: modeling the micro-explosions," *Appl. Phys. B* 69, 71-80 (1999).
- [82] P.F. Schofield, K.S. Knight, J.A.M. van der Houwen, E. Valsami-Jones, "The role of hydrogen bonding in the thermal expansion and dehydration of brushite, di-calcium phosphate dihydrate," *Phys. Chem Minerals* 31, 606-624 (2004).

- [83] D. Fried, M. Zuerlein, J. D. B. Featherstone, W. Seka, C. Duhn, S. M. McCormack, "IR laser ablation of dental enamel: mechanistic dependence on the primary absorber," *Appl. Surf. Sci* 127-129, 852-856 (1998).
- [84] E. Esch, W. N. Simmons, G. Sankin, H. F. Cocks, G. M. Preminger, P. Zhong, "A simple method for fabricating artificial kidney stones of different physical properties," *Urol Res.* 38(4), 315-319 (2010).
- [85] A. Wierzbicki, C.S. Sikes, J. D. Sallis, J. D. Madura, E. D. Stevens, K.L. Martin, "Scanning electron microscopy and molecular modeling of inhibition of calcium oxalate monohydrate crystal growth by citrate and phosphocitrate," *Calcif Tissue Int* 45, 297-304 (1995).
- [86] L. A. Hardy, J. D. Kennedy, C. R. Wilson, P. B. Irby, N. M. Fried, "Analysis of thulium fiber laser induced bubble dynamics for ablation of kidney stones," *J. Bio* 20160010, (2016).
- [87] P. Carmona, J. Bellanato, E. Escolar, " Infrared and Raman Spectroscopy of Urinary Calculi: A Review," 3(5), 331-346 (1997).
- [88] S. Spore, J. Teichman, N. Corbin, P. Champion, E. Williamson, R. Glickman, "Holmium:YAG Lithotripsy: optimal power settings," *J. Endourol.* 13(8), 559-566 (2009).
- [89] G. M. Hale, M. R. Querry, A. N. Rusk, and D. Williams, "Influence of temperature on the spectrum of water," *JOSA* 62(9), 1103-1108 (1972).
- [90] J. T. Walsh, J.P. Cummings, "Effect of the dynamic optical properties of water on midinfrared laser ablation," *Lasers Surg. Med.* 15(3), 295-305 (1994).
- [91] L. A. Hardy, P. B. Irby, N.M. Fried, "Scanning electron microscopy of real and artificial kidney stones before and after Thulium fiber laser ablation in air and water," *Proc. SPIE* 104680G (2018).
- [92] K. T. Schomacker, Y. Domankevitz, T. J. Flotte, and T. F. Deutsch, "Co:MgF₂ laser ablation of tissue: effect of wavelength on ablation threshold and thermal damage," *Lasers Surg. Med.* 11, 141-151 (1991).
- [93] J. T. Walsh, T. J. Flotte, and T. F. Deutsch, "Er:YAG laser ablation of tissue: effect of pulse duration and tissue type on thermal damage," *Lasers Surg. Med.* 9(4), 314-326 (1989).
- [94] J. P. Cummings and J. T. Walsh, "Erbium laser ablation: The effect of dynamic optical properties," *Appl. Phys. Lett.* 62(16), 1988-1990 (1993).
- [95] N. S. Nishioka, Y. Domankevitz, "Comparison of tissue ablation with pulsed holmium and thulium lasers," *IEEE J. Quantum Electron.* 26(12), 2271-2275 (1990).
- [96] I. Stein, R. O. Stein, M. L. Beller, "Living Bone in Health and Disease," Philadelphia: J. B Lippincott, 52 (1955).

- [97] S. N. Chawla, M. F. Chang, A. Chang, J. Lenoir, and D. H. Bagley, "Effectiveness of high-frequency holmium:YAG laser stone fragmentation: the popcorn effect," *J. Endourol.* 22, 645-649 (2008).
- [98] A. J. Marks and J. M. H. Teichman, "Lasers in clinical urology: state of the art and new horizons," *World J. Urol.* 25, 227-233 (2007).
- [99] O. Schatloff, U. Lindner, J. Ramon, et al. "Randomized trial of stone fragment active retrieval versus spontaneous passage during holmium laser lithotripsy for ureteral stones," *J. Urol.* 183, 1031-1035 (2010).
- [100] D. Pal, A. Ghosh, R. Sen, and A. Pal, Continuous-wave and quasi-continuous wave thulium-doped all-fiber laser: implementation on kidney stone fragmentations, *Appl. Opt.* 55, 6151-6155 (2016).
- [101] F. Wezel, A Hacker, A. J. Gross, M. S. Michel, and T. Bach, "Effect of pulse energy, frequency and length on Holmium:Yttrium-Aluminum-Garnet laser fragmentation efficiency in non-floating artificial urinary calculi," *J. Endourol.* 24, 1135-1140 (2010).

APPENDIX A: LIST OF PEER-REVIEWED PUBLICATIONS

- [1] **Luke A. Hardy**, Christopher R. Wilson, Pierce B. Irby, Nathaniel M. Fried, "Rapid Thulium Fiber Laser Lithotripsy at Pulse Rates Up to 500 Hz using a Stone Basket," *IEEE Journal of Selected Topics in Quantum Electronics*, 20(5):0902604 (2014).
- [2] Richard L. Blackmon, Thomas C. Hutchens, **Luke A. Hardy**, Christopher R. Wilson, Pierce B. Irby, Nathaniel M. Fried, "Thulium Fiber Laser Ablation of Kidney Stones using a 50- μ m-Core Silica Optical Fiber," *Optical Engineering*, 54(1):011004 (2014).
- [3] **Luke A. Hardy**, Christopher R. Wilson, Pierce B. Irby, Nathaniel M. Fried, "Thulium Fiber Laser Lithotripsy in an in Vitro Ureter Model" *Journal of Biomedical Optics*, 19(12):128001 (2014).
- [4] Christopher R. Wilson, **Luke A. Hardy**, Pierce B. Irby, Nathaniel M. Fried, "Collateral Damage to the Ureter and Nitinol Stone Baskets during Thulium Fiber Laser Lithotripsy," *Lasers in Surgery & Medicine*, 47(5) 403-410 (2015).
- [5] Christopher R. Wilson, Thomas C. Hutchens, **Luke A. Hardy**, Pierce B. Irby, Nathaniel M. Fried, "A miniaturized, 1.9 french integrated optical fiber and stone basket for use in thulium fiber laser lithotripsy," *Journal of Endourology*, 29(10):1110-4 (2015).
- [6] Christopher R. Wilson, **Luke A. Hardy**, Pierce B. Irby, Nathaniel M. Fried, "Miniature Ball Tip Optical Fibers for use in Thulium Fiber Laser Ablation of Kidney Stones," *Journal of Biomedical Optics*, Opt. 21(1): 018003 (2016).
- [7] Christopher R. Wilson, **Luke A. Hardy**, Pierce B. Irby, Nathaniel M. Fried, "Microscopic analysis of laser- induced proximal fiber tip damage during Holmium:YAG and thulium fiber laser lithotripsy," *Optical Engineering*, 55(4):046102 (2016).
- [8] **Luke A. Hardy**, Joshua D. Kennedy, Christopher R. Wilson, Pierce B. Irby, Nathaniel M. Fried, "Analysis of thulium fiber laser induced bubble dynamics for ablation of kidney stones," *Journal of Biophotonics*, 10(10):1240-1249 (2016).
- [9] **Luke A. Hardy**, Chun-Hung Chang, Erin Myers EM, Michael J. Kennelly, Nathaniel M. Fried, "Computer Simulations of Thermal Tissue Remodeling during Transvaginal and Transurethral Laser Treatment of Female Stress Urinary Incontinence," *Laser in Surgery & Medicine*, 49:198-205 (2017).
- [10] Thomas C. Hutchens, David D. Gonzalez, **Luke A. Hardy**, Scott C. McLanahan, Nathaniel M. Fried, "Thulium Fiber Laser Recanalization of Occluded Ventricular Catheters in an Ex Vivo Tissue," *Journal of Biomedical Optics*, 22(4):048001 (2017).
- [11] **Luke A. Hardy**, Thomas C. Hutchens, Eric R. Larson, David A. Gonzalez, Chun-Hung Chang, William H. Nau, Nathaniel M. Fried, "Rapid Sealing of Porcine Renal

Blood Vessels, Ex Vivo using a High Power, 1470-nm Laser and Laparoscopic Prototype,” *Journal of Biomedical Optics*, 22(5):058002 (2017).

- [12] David A. Gonzalez, **Luke A. Hardy**, Thomas C. Hutchens, Pierce B. Irby, Nathaniel M. Fried, “Thulium Fiber Laser Induced Vapor Bubble Dynamics using Bare, Tapered, Ball, Hollow Steel, and Muzzle Brake fiber Optic tips,” *Optical Engineering*, 57(3):036106 (2018).

APPENDIX B: LIST OF PEER-REVIEWED CONFERENCE PROCEEDINGS

- [1] Richard L. Blackmon, Thomas C. Hutchens, **Luke A. Hardy**, Pierce B. Irby, Nathaniel M. Fried, "Characterization of a 50- μ m-core optical fiber for use in Thulium fiber laser lithotripsy," Proc. SPIE 8926, Photonic Therapeutics and Diagnostics X, 89261F (2014).
- [2] **Luke A. Hardy**, Christopher R. Wilson, Pierce B. Irby, Nathaniel M. Fried, "Rapid vaporization of kidney stones, ex vivo, using a Thulium fiber laser operated at pulse rates up to 500Hz," Proc. SPIE 8926, Photonic Therapeutics and Diagnostics X, 89261H (2014).
- [3] Christopher R. Wilson, Thomas C. Hutchens, **Luke A. Hardy**, Pierce B. Irby, Nathaniel M. Fried, "A permanently integrated fiber and stone basket for Thulium fiber laser lithotripsy," Proc. SPIE 8926, Photonic Therapeutics and Diagnostics X, 89261J (2014).
- [4] **Luke A. Hardy**, Christopher R. Wilson, Pierce B. Irby, Nathaniel M. Fried, "Kidney stone ablation times and peak saline temperatures during Holmium:YAG and Thulium fiber laser lithotripsy, ex vivo, in a ureteral model," Proc. SPIE 9303, Photonic Therapeutics and Diagnostics XI, 930310 (2015).
- [5] Christopher R. Wilson, **Luke A. Hardy**, Pierce B. Irby, Nathaniel M. Fried, "Thulium fiber laser damage to Nitinol stone baskets," Proc. SPIE 9303, Photonic Therapeutics and Diagnostics XI, 93031A (2015).
- [6] Christopher R. Wilson, **Luke A. Hardy**, Pierce B. Irby, Nathaniel M. Fried, "Thulium fiber laser damage to the ureter," Proc. SPIE 9542, Medical Laser Applications and Laser-Tissue Interactions VII, 95420C (2015).
- [7] Christopher R. Wilson, **Luke A. Hardy**, Pierce B. Irby, Nathaniel M. Fried, "Thulium Fiber Laser Lithotripsy using small spherical distal fiber tips," Proc. SPIE 9689, Photonic Therapeutics and Diagnostics XII, 96891G (2016).
- [8] **Luke A. Hardy**, Christopher R. Wilson, Joshua D. Kennedy, Pierce B. Irby, Nathaniel M. Fried, "Cavitation bubble dynamics during Thulium fiber laser lithotripsy," Proc. SPIE 9689, Photonic Therapeutics and Diagnostics XII, 96891B (2016).
- [9] Christopher R. Wilson, **Luke A. Hardy**, Pierce B. Irby, Nathaniel M. Fried, "Proximal fiber tip damage during Holmium:YAG and Thulium Fiber laser ablation of kidney stones," Proc. SPIE 9689, Photonic Therapeutics and Diagnostics XII, 96891Q, (2016).
- [10] **Luke A. Hardy**, Chun-Hung Chang, Erinn M. Myers, Michael J. Kennelly, Nathaniel M. Fried, "Laser treatment of female stress urinary incontinence: optical, thermal, and tissue damage simulations," Proc. SPIE 9689, Photonic Therapeutics and Diagnostics XII, 96891R, (2016).
- [11] **Luke A. Hardy**, Eric R. Larson, Thomas C. Hutches, David A. Gonzalez, Chun-Hung Chang, William H. Nau, Nathaniel M. Fried, "Laparoscopic prototype for

- optical sealing of renal blood vessels,” Proc. SPIE 10038, Therapeutics and Diagnostics in Urology: Lasers, Robotics, Minimally Invasive, and Advanced Biomedical Devices, 100380V (2017).
- [12] **Luke A. Hardy**, Pierce B. Irby, Nathaniel M. Fried, “Scanning Electron Microscopy of Real and Artificial Kidney Stones Before and After Thulium fiber laser Ablation in Air and Water,” Proc. SPIE 10468, Therapeutics and Diagnostics in Urology 2018, 104680G (2018).
- [13] **Luke A. Hardy**, David A. Gonzalez, Pierce B. Irby, Nathaniel M. Fried, “Fragmentation and Dusting of Large Kidney Stones with Compact, Air-cooled, High Peak Power, 1940-nm, Thulium Fiber Laser,” Proc. SPIE 10468, Therapeutics and Diagnostics in Urology 2018, 104680O (2018).
- [14] Chun-Hung Chang, **Luke A. Hardy**, Michael G. Peters, Dina A. Bastawros, Erin M. Myers, Michael J. Kennelly, Nathaniel M. Fried, “Optical clearing of vaginal tissues in cadavers,” Proc. SPIE 10468, Therapeutics and Diagnostics in Urology 2018, 104680K (2018).
- [15] David A. Gonzalez, **Luke A. Hardy**, Thomas C. Hutchens, Pierce B. Irby, Nathaniel M. Fried, “Thulium fiber laser induced vapor bubbles using bare, tapered, ball, hollow steel, and muzzle brake fiber optic tips,” Proc. SPIE 10468, Therapeutics and Diagnostics in Urology 2018, 1046806 (2018).

APPENDIX C: DYNAMIC PULSING DURING THULIUM FIBER LASER FOR LITHOTRIPSY

C.1 Introduction

The TFL can be electronically modulated, giving a large matrix of laser parameters that can be explored for ablation of kidney stones. This enables customized laser pulse parameters termed, “dynamic pulsing”, for use in laser lithotripsy.

Previous preliminary studies have shown that dynamic pulsing during TFL lithotripsy increases stone ablation rates [1]. The use of dynamic pulsing and higher pulse rates are studied to increase calcium oxalate monohydrate (COM) and uric acid (UA) stone ablation rates.

Dynamic pulsing is defined as operation of the laser with customized micro-pulse trains of laser pulses as opposed to conventional pulse trains, in an effort to produce more rapid and efficient tissue ablation (Figure C.1).

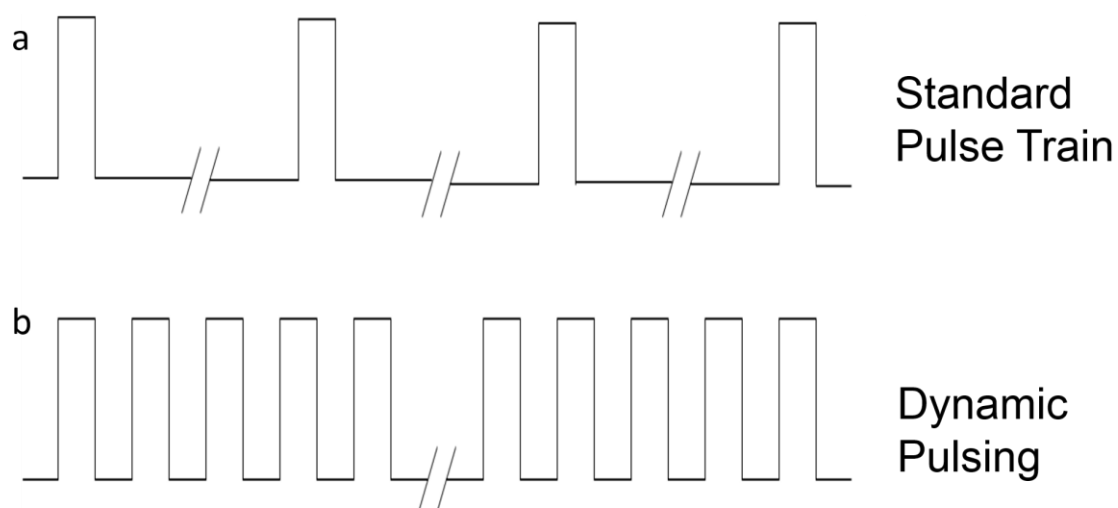


Figure C.1. Temporal beam profile of (a) standard pulse train, and (b) micro-pulse train of a laser.

Long-pulse laser lithotripsy is primarily a photothermal process. Therefore, it is important to optimize the laser pulse duration to produce rapid stone removal rates. A laser pulse that is too short will produce plasma that shields incoming laser energy and results in a reduced ablation rate. A laser pulse that is too long will result in thermalized energy diffusing out from the local treatment site during the laser pulse instead of being consumed in the phase transition process during vaporization, also reducing ablation rates. The solution to the Bio-Heat Transfer Equation below provides criteria for the thermal relaxation time, based on the optical and thermal properties of materials. The laser pulse duration should be less than the thermal relaxation time (Equation 1) for optimal tissue removal.

$$\text{(Equation C.1)} \quad \tau_r = \frac{\delta^2}{4\alpha}$$

Where δ (m) is the penetration depth of the wavelength of light, and α is the thermal diffusivity (m^2/s). The thermal diffusivity of the tissue can be found using k thermal conductivity, ρ density and c the specific heat of the tissue using the equation:

$$\text{(Equation C.2)} \quad \alpha = \frac{k}{\rho c}$$

Unfortunately, the optical and thermal properties of kidney stones are not well characterized. Instead, values for arterial plaque, a similar calcified biological material to kidney stones, were used to provide an approximate calculated thermal relaxation time of 2-10 ms [2,3]. The 5-pulse and 10-pulse micro-pulse trains used in this study were chosen for testing based on this range of thermal relaxation times.

C.2 Methods

A 100-Watt TFL (TLR 100-1908, IPG Photonics, Inc., Oxford, MA) was operated at a wavelength of 1908 nm, pulse energy of 35 mJ, and pulse durations of 500 μ s. TFL energy was delivered through two types of 100- μ m-core, low-OH, silica optical fibers (AFS105/125Y, Thorlabs, Newton, NJ) (FIP100120140, Polymicro Technologies, Phoenix, AZ). The TFL was externally modulated by a function generator (Model DS345, Stanford Research Systems, Sunnyvale, California) to produce the customized pulse packets or pulse trains.

Pulse packets were defined as a group of pulses assembled into a single packet (Figure C.1). Three pulse packet configurations were tested: standard pulse trains, 5-pulse packets, and 10-pulse packets with pulse rates of 50 – 500 Hz (Figure C.2).

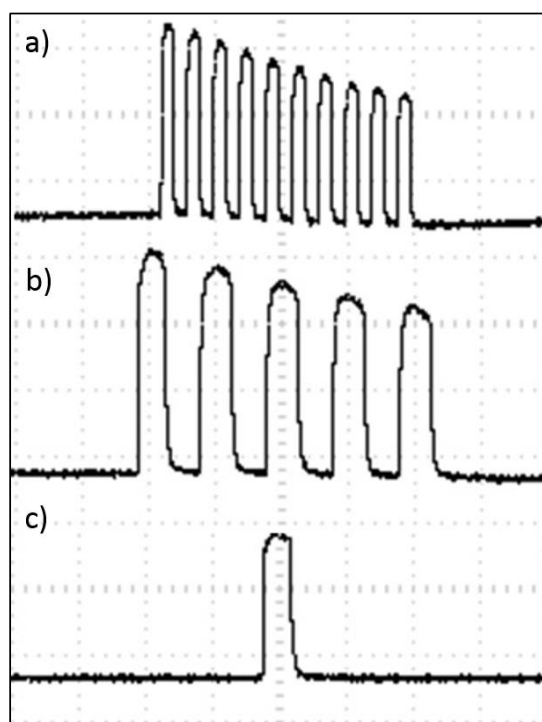


Figure C.2. (a) 10-pulse packet , (b) 5- pulse packet, and (c) standard pulse.

The duration of the macro pulse packets were determined by an estimated thermal relaxation time (Equation C.1). The thermal relaxation time is defined as the amount of time needed for an object's incident thermal energy to decrease 63%, which is theorized to be the optimum pulse duration for thermal confinement [4]. Not all thermal and optical properties of COM stones are available, so calcified plaque was used as a suitable substitute for stone properties of COM stones [2,3]. The estimates yielded a thermal relaxation time between 2 to 10 ms for COM stones. Estimates fit the pulse durations for standard pulse trains, 5-pulse packets, and 10-pulse packets which are 500 μ s, 4.5 ms and 9.5 ms, respectively.

COM and UA stone samples were kept fixed and submerged in a saline bath during laser irradiation. Each stone was irradiated for one minute. Samples were dried by heating to 60°C for 30 minutes and then weighed with an analytical balance (AB54-S, Mettler-Toledo, Switzerland) before and after each experiment. Stone ablation rates (μ g/s) were calculated by dividing the difference in mass by the total irradiation time. Ablation rates (μ g/s) were measured with a minimum of five stone samples in each data set. Ablation rates were plotted on a graph as a function of pulse rate, comparing standard, 5-pulse, and 10-pulse packets for COM and UA stones (Figure C.3).

C.3 Results

At pulse rates less than 100 Hz, dynamic pulsing provided a 2-fold increase in stone ablation rates. However, as laser pulse rates were increased above 100 Hz, the standard and customized pulse trains provided equivalent results. Stone vaporization rates reached 4.5 mg/s and 1.3 mg/s for UA and COM stones, respectively, when operating the laser at 500 Hz (Figure C.5).

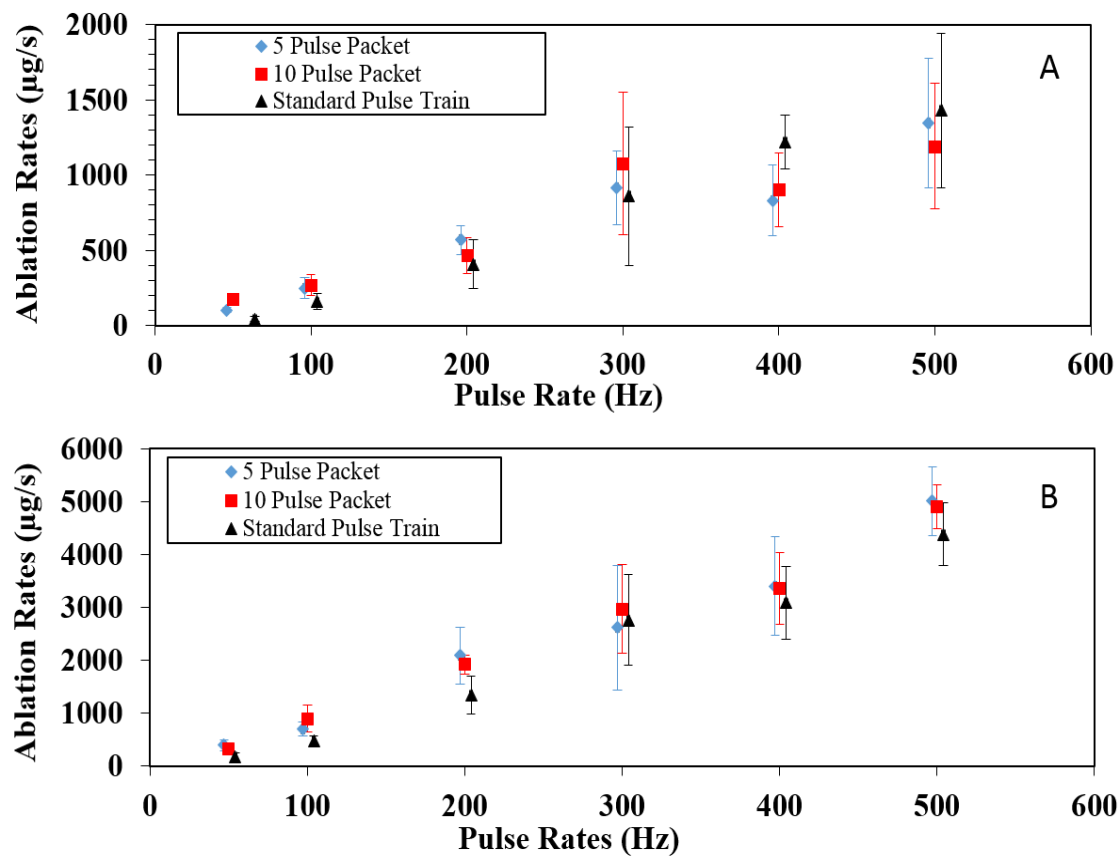


Figure C. 5. Displays ablation rates for (a) COM and (b) uric acid stones for both 5, and 10 pulse packets.

C.4 Conclusion

Dynamic pulsing during Thulium fiber laser lithotripsy results in increased stone vaporization rates that may be practical for use in the clinic. However at higher pulse rates (> 100 Hz), the difference between standard pulses and the dynamic pulses were not statistically significant ($P > 0.05$). It was calculated that typical UA and COM stones (8-10 mm diameter) could be completely vaporized in about 5 and 15 min, respectively, with possibly shorter times if only fragmentation is desired.

C.5 References

- [1] Blackmon RL, Irby PB, Fried NM, “Enhanced thulium fiber laser lithotripsy using micro-pulse train modulation,” *J Biomed Opt*, 17(2), (2012).
- [2] Welch AJ, Gemert MJC, “Optical-thermal response of laser-irradiated tissue,” Plenum Press: New York, (1995).
- [3] Sundaramoorthi P, Kalainathan S, Kanchana G, Santhi R, “Electrical, Thermal Parameter Calculations of Artificially Removed Human Renal Stones by Two-Probes Method,” *Asian J. Chem.* 20(3), 1711-1722 (2008).
- [4] Bernard C, Welch AJ, “Analysis of thermal relaxation during laser irradiation of tissue,” *Lasers Surg. Med.* (29), 351-359 (2001).

APPENDIX D: FRAGMENTATION AND DUSTING OF LARGE KIDNEY STONES USING COMPACT AIR-COOLED, HIGH PEAK POWER, 1940-nm, THULIUM FIBER LASER

D.1 Introduction

Numerous previous studies have reported that use of low laser pulse energy, high pulse rates, long pulse duration, and/or small optical fibers reduce stone retropulsion [1-7]. Unfortunately, the Holmium laser, based on the fundamental technical limitations described above (e.g. low pulse rates and large fibers), in general, is not well suited for stone dusting. On the contrary, TFL technology, due to its ability to operate at high pulse rates and couple laser energy into smaller optical fibers, is ideally suited for stone dusting.

Depending on stone size and location in the urinary tract, either fragmentation or dusting may be desirable. Our laboratory has previously only reported on TFL lithotripsy in dusting mode using small fibers and high pulse rates. All of our previous studies were limited to the use of a large, water cooled, 100-Watt, continuous-wave, TFL, electronically modulated to operate with a peak power of only about 70 W (35 mJ at 500 μ s) [8,9]. This technical limitation required laser lithotripsy operation only in a dusting mode with a low pulse energy of 35 mJ, compensated by high pulse rates of up to 500 Hz [8,9]. While dusting may be sufficient for smaller stones (< 10 mm diameter), it may be too slow for treatment of larger urinary stones (> 10 mm diameter).

Recently, a higher peak power TFL was tested with direct comparison to Holmium laser. The TFL provided 2-4 times faster stone ablation than Holmium laser using equivalent laser parameters, and reduced stone retropulsion [10-12]. In this study, a novel TFL capable of operation at up to 500 W peak power (7x higher than 1st generation TFL), up to

50 W average power, and pulse rates up to 2000 Hz, was tested. This TFL was also more compact and air-cooled for potential future clinical use (Table D.1). We studied TFL laser ablation of large uric acid and calcium oxalate monohydrate stones using three modes: (a) dusting, (b) fragmentation, and (c) a dual mode approach involving first fragmenting stone into smaller pieces, followed by dusting to reduce all stone fragments to less than 2 mm. We hypothesize that a dual mode approach provides enhanced stone ablation rates because large stones initially experience less retropulsion so high laser pulse energy is used, while smaller stone fragments created later in the procedure experience higher stone retropulsion so lower pulse energy setting is used.

Table D.1. Comparison of 1st and 2nd generation Thulium fiber laser technology.

Parameters	1st Generation	2 nd Generation
Manufacture Date:	2004	2016
Physical Dimensions (cm):	50 x 60 x 80	27 x 45 x 55
Weight (kg):	120	40
Wavelength (nm):	1908	1940
Peak Power (W):	70	500
Average Power (W):	100	50
Pulse Rate (Hz):	1-1000	1-2000
Cooling System:	External Water	Air

* Weight and dimensions for 1st generation TFL do not include separate recirculating water chiller.

D.2 Methods

A compact, air-cooled, high-power Thulium fiber laser (IPG Medical, Marlborough, MA) operating at 1940 nm wavelength was used (Figure 1). Laser pulse duration (500 μ s), average power (10 W), and fiber size (270- μ m-core) were kept fixed, while pulse energy (33 or 200 mJ) and pulse rate (50 or 300 Hz) were changed, based on three different operation modes, including fragmentation, dusting, and dual mode (fragmentation then dusting) (Table D.2).

Table D.2. Laser lithotripsy operation modes.

Mode	Dust	Fragment	Dual mode
Pulse Energy (mJ):	33	200	200/33
Pulse Rate (Hz):	300	50	50/300
Peak Power (W):	66	400	400/66
Average Power (W):	10	10	10
Pulse Duration (μ s)	500	500	500

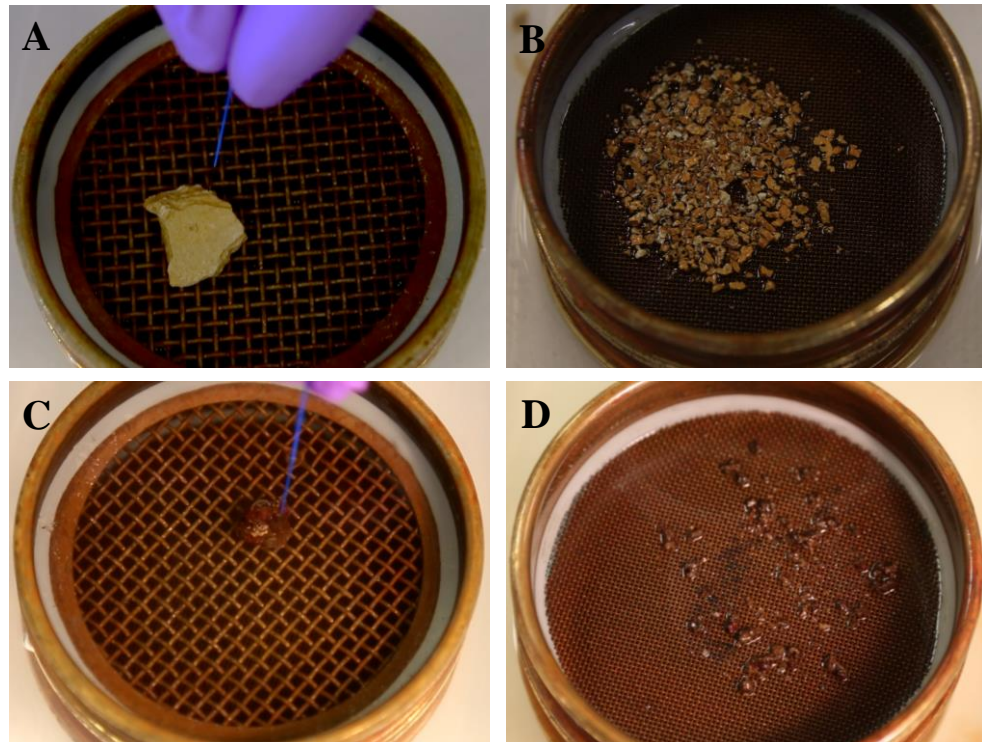


Figure D.1. Stones (A,C) before ablation, resting on 2-mm mesh sieve and (B,D) stone fragments after ablation, resting on 1-mm mesh sieve. (A,B) UA stone (initial mass = 1359 mg). (C,D) COM stone (initial mass = 510 mg).

Uric acid (UA) and calcium oxalate monohydrate (COM) stones were used in this study because they make up the vast majority of stones encountered clinically [13]. Samples obtained from a stone analysis laboratory (Labcorp, Oklahoma City, OK) were desiccated in an oven prior to weighing and experiments. 23 large UA stones were separated into 3 groups with similar average mass (1.9 ± 0.5 g, 1.9 ± 0.5 g, 1.9 ± 0.4 g). 16 large COM stones were also separated into 3 groups with similar average mass (0.5 ± 0.1 g, 0.8 ± 0.2 g, 0.7 ± 0.2 g). The difference in number and size of stones between UA and COM groups was due to limited availability of large COM stones.

In Group 1 (Dust), the TFL delivered 33mJ/300Hz (n=9), similar to previously published studies with 1st generation TFL. In Group 2 (Fragment), the TFL delivered 200mJ/50Hz (n=7). In Group 3 (Dual mode), the stone was fragmented at 200mJ/50Hz,

and then smaller stone fragments dusted at 33mJ/300Hz (n=7). The fiber tip was held manually in contact with the stone on a 2-mm-mesh sieve submerged in a saline bath with irrigation flow (Figure D.1). Stone ablation rates were calculated by dividing the initial stone mass by the total treatment time.

D.3 Results

Procedure times for UA stones were 918 ± 312 s, 855 ± 245 s, and 436 ± 312 s, and ablation rates were calculated to be 2.3 ± 0.8 mg/s, 2.3 ± 0.2 mg/s, and 4.4 ± 0.8 mg/s for dusting, fragmentation, and dual mode, respectively. Procedure times for COM stones were 1427 ± 468 s, 777 ± 170 s, and 974 ± 575 s, and ablation rates were 0.4 ± 0.1 mg/s, 1.0 ± 0.1 mg/s, and 0.9 ± 0.4 mg/s for dusting, fragmentation, and dual mode (Table D.3 and Figure D.2).

Table D.3. Stone specifications and ablation rates.

Stone Type	Dust	Fragment	Dual mode
UA stones			
Sample # (n):	9	7	7
Mass (g):	1.9 ± 0.5	1.9 ± 0.5	1.9 ± 0.4
Proc. time (s):	918 ± 312	855 ± 245	436 ± 118
Ablation Rate (mg/s):	2.3 ± 0.8	2.3 ± 0.2	4.4 ± 0.8
COM stone			
Sample # (n):	5	5	6
Mass (g):	0.5 ± 0.1	0.8 ± 0.2	0.7 ± 0.2
Proc. time (s):	1427 ± 468	777 ± 170	974 ± 575
Ablation Rate (mg/s):	0.4 ± 0.1	1.0 ± 0.1	0.9 ± 0.4

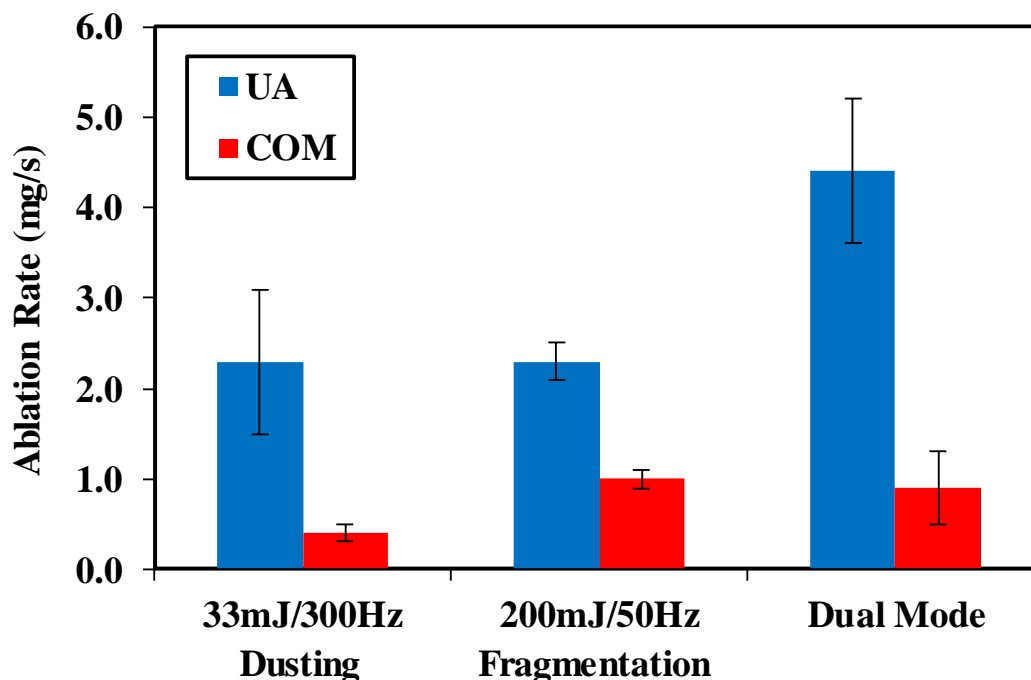


Figure D.2. Stone ablation rates as a function of operation mode.

D.4 Discussion

The Thulium fiber laser is currently being studied as a potential alternative to the conventional Holmium:YAG laser for lithotripsy. Multiple studies have reported that the TFL provides higher kidney stone ablation rates and lower stone retropulsion than the Holmium laser, for equivalent laser parameters [10-12]. The purpose of this study was to compare fragmentation, dusting, and dual mode approaches specifically for TFL treatment of large urinary stones. In general, TFL technology, with its ability to operate at high pulse rates, is ideal for stone dusting, and the next generation TFL presented here, with its higher peak power, is also capable of efficient stone fragmentation. We hypothesized that a dual mode approach (fragmentation of large stones followed by dusting of smaller stone fragments) may improve ablation rates, based on the assumption that larger and heavier stones experience less stone retropulsion, while smaller and lighter stone fragments experience greater stone retropulsion during laser lithotripsy.

For UA stones, the dual mode setting, defined as fragmentation (200mJ/50Hz) followed by dusting (33mJ/300Hz), provided a factor of two times improvement in stone ablation rates compared with either fragmentation or dusting modes alone (4.4 mg/s vs. 2.3 mg/s), consistent with our hypothesis.

However, a similar trend was not observed for COM stone ablation results. The TFL ablation threshold has previously been reported to be three times higher for COM stones than for UA stones (21 vs. 7 J/cm²) [14]. In this current study, a laser pulse energy of 33 mJ for dusting mode translated into a radiant exposure of 58 J/cm², based on fiber core diameter and application of fiber in contact mode with stone. This value is relatively close to the COM stone ablation threshold, so dusting yielded low COM stone ablation rates of less than 1 mg/s. For fragmentation, however, a high pulse energy of 200 mJ provided a higher radiant exposure of 350 J/cm², well above the reported COM stone ablation threshold, and a sufficient stone ablation rate of about 1 mg/s for potential clinical use.

The higher peak power TFL system also allowed use of larger (270- μ m-core) fibers than in previous studies (50-150 μ m core). General advantages of a larger fiber include easier coupling of laser energy into the fiber and a more robust fiber less likely to experience distal fiber tip degradation or burnback during laser lithotripsy [15, 16].

All of these experiments used an average laser power of 10 W, for direct comparison between different operation modes and previous studies (limited to use with 1st generation TFL operating at low pulse energy and high pulse rates). Future studies will explore average powers up to 50 W, using higher pulse energies and/or pulse rates to determine if TFL is a viable alternative to the conventional Holmium laser for ablation of large urinary stones.

D.7 Conclusion

A new, compact, air-cooled Thulium fiber laser capable of operation at a peak power up to 500 W, an average power up to 50 W, and pulse rates up to 2000 Hz, was tested for ablation of large uric acid and calcium oxalate monohydrate stones. For UA stones, dual mode operation consisting of fragmentation (200 mJ / 50 Hz) followed by dusting (33 mJ / 300 Hz) produced the highest stone ablation rates of over 4 mg/s, while for COM stones, the fragmentation mode (200 mJ / 50 Hz) produced the highest stone ablation rates of about 1 mg/s. Future studies will focus on the use of higher average power (> 10 W) for even faster treatment of large urinary stones.

D.7 References

- [1] M. D. White, M. E. Moran, C. J. Calvano, A. Borhan-Manesh, and B. A. Mehlhaff, "Evaluation of retropulsion caused by Holmium:YAG laser with various power settings and fibers," *J. Endourol.* 12(2), 183-186 (1998).
- [2] H. Lee, T. R. Ryan, J. M. H. Teichman, J. Kim, B. Choi, N. V. Arakeri, and A. J. Welch, "Stone retropulsion during Holmium:YAG Lithotripsy," *J. Urol.* 169(3), 881-885 (2003).
- [3] H. Lee, R. T. Ryan, J. Kim, B. Choi, N. V. Arakeri, J. M. Teichman, and A. J. Welch, "Dependence of calculus retropulsion dynamics on fiber size and radiant exposure during Ho:YAG lithotripsy," *J. Biomechan. Eng.* 126(4), 506-515 (2004).
- [4] D. S. Finley, J. Petersen, C. Abdelshehid, M. Ahlering, D. Chou, J. Borin, L. Eichel, E. McDougall, and R. V. Clayman, "Effect of Holmium:YAG laser pulse width on lithotripsy retropulsion in vitro," *J. Endourol.* 19(8), 1041-1044 (2005).
- [5] C. G. Marguet, J. C. Sung, W. P. Springhart, J. O. L'Esperance, S. Zhou, P. Zhong, D. M. Albala, and G. M. Preminger, "In vitro comparison of stone retropulsion and fragmentation of the frequency doubled, double pulse nd:yag laser and the holmium:yag laser," *J. Urol.* 173(5), 1797-1800 (2005).
- [6] H. W. Kang, H. Lee, J. M. Teichman, J. Oh, J. Kim, and A. J. Welch, "Dependence of calculus retropulsion on pulse duration during Ho:YAG laser Lithotripsy," *Lasers Surg. Med.* 38(8), 762-772 (2006).
- [7] W. Kamal, P. Kallidonis, G. Koukiou, L. Amanatides, V. Panagopoulos, P. Ntasiotis, E. Liatsikos, "Stone retropulsion with Ho:YAG and Tm:YAG lasers: a clinical practice-oriented experimental study," *J. Endourol.* 30(11), 1145-1149 (2016).
- [8] L. A. Hardy, C. R. Wilson, P. B. Irby, and N. M. Fried, "Rapid Thulium fiber laser lithotripsy at pulse rates up to 500 Hz using a stone basket," *IEEE J. Sel. Top. Quantum Electron.* 20(5), 0902604 (2014).
- [9] L. A. Hardy, C. R. Wilson, P. B. Irby, and N. M. Fried, "Thulium fiber laser lithotripsy in an in vitro ureter model," *J. Biomed. Opt.* 19(12), 128001 (2014).
- [10] V. Zamyatina, V. Minaev, I. Yaroslavsky, A. Kovalenko, A. Vinarov, and G. Altshuler, "Super pulse thulium fiber laser for lithotripsy," *Lasers Surg. Med.* 48(10), 10 (2016) (Abstract #28).
- [11] P. Glybochko, G. Altshuler, A. Vinarov, L. Rapoport, M. Enikeev, N. Grigoriev, D. Enikeev, N. Sorokin, A. Dymov, R. Sukhanov, M. Taratkin, and V. Zamyatina, "Comparison between the possibilities of holmium and thulium laser in lithotripsy in vitro," *Eur. Urol. Suppl.* 16, e391 (2017). (Abstract #226).
- [12] A. Dymov, P. Glybochko, Y. Alyaev, A. Vinarov, G. Altshuler, V. Zamyatina, N. Sorokin, D. Enikeev, V. Lekarev, A. Proskura, and A. Koshkarev, "Thulium lithotripsy: from experiment to clinical practice," *J. Urol.* 197, e1285 (2017) (Abstract V11-11).

- [13] D. M. Wilson, "Clinical and laboratory approaches for evaluation of nephrolithiasis," *J. Urol.* 141(3 Pt 2), 770-774 (1989).
- [14] R. L. Blackmon, "Thulium fiber laser lithotripsy," Ph.D. Thesis, University of North Carolina at Charlotte (2013).
- [15] A. C. Mues, J. M. Teichman, and B. E. Knudsen, "Quantification of holmium:yttrium aluminum garnet optical tip degradation," *J. Endourol.* 23(9), 1425-1428 (2009).
- [16] R. L. Blackmon, P. B. Irby, and N. M. Fried, "Thulium fiber laser lithotripsy using tapered fibers," *Lasers Surg. Med.* 42(1), 45-50 (2010).